The Bio-Optical Detection of Harmful Algal Blooms

Stewart Bernard

Thesis Presented for the Degree of

DOCTOR OF PHILOSOPHY

in the Department of Oceanography

UNIVERSITY OF CAPE TOWN

August 2005

Acknowledgements

For much support and advice, my supervisors: Trevor Probyn and Frank Shillington.

For advice, support, and data: Grant Pitcher, Collin Roesler, Annick Bricaud, André Morel, Ray Barlow, Arturo Quirantes, Andre du Randt, Desiree Calder, Mike Lucas, Stacey McLeroy-Etheridge, Joséphine Ras, Stanford Hooker, Jim Aiken, Alex Fawcett, Victor Vicente, Malik Chami, Mary-Jane Perry, Curt Mobley, Emmanual Boss, Jill Schwarz, Heather Sessions, Christelle Balt, Pedro Monteiro, Christo Whittle, Koos Williams, Larry Hutchings, Rick Harding, Howard Waldron, Penny Price, August Miller, Terry Hedderson, the captains and crews of the *Africana* and *Algoa*.

For direct funding: Marine & Coastal Management, the National Research Foundation, the Benguela Current Large Marine Ecosystem programme, the Office of Naval Research, Southampton Oceanography Centre.

For great patience: my parents, and Megan Hall.

The first two distributions were chosen due to their proven ability as moment-matched equivalent distributions in atmospheric physics. In addition, these distributions can be conveniently expressed analytically as a function of their effective radii and variance. The second two distributions were chosen due to their common use in the marine bio-optical field [Bricaud & Morel 1986, Campbell 1995, Morel 1973, Boss *et al.* 2001]. Note that the Junge distribution is the only formula that is not explicitly expressed in terms of effective radius and variance, and equivalent distributions were calculated by iteratively adjusting the Junge slope ξ until d_{eff} of the Junge distribution matched that of the measured distribution. It should also be noted that the effective variance of a Junge distribution cannot be independently manipulated, unlike the first three formulae, when using a given size range [Boss *et al.* 2001]. The single size approximation was analysed as a simple and computationally economic alternative. Two analyses were carried out with regard to the effective variance v_{eff}: the first using the variable experimental v_{eff} values determined for each sample, and the second using a constant v_{eff} value of 0.63, the mean value for all samples.

2.2.7 Optical Modelling

Analogous expressions to Equation 2.2 can be used to express the relationships between the attenuation coefficient $c(\lambda)$, the scattering coefficient $b(\lambda)$, the backscattering coefficient $b_b(\lambda)$ and their relative efficiency factors, given appropriate particle size distributions and complex refractive index spectra. Additional detail on such models can be found in Morel & Bricaud [1986]. In addition, the dimensionless package effect parameter (Q_a^*) can be calculated from the following expression [Morel & Bricaud 1981]:

$$Q_a^* = \frac{3}{2}\frac{Q_a}{a_{cm}\,d} \qquad (2.9)$$

where a_{cm} is the absorption of cellular material (m^{-1}) and is given by $a_{cm}=4\pi n'/\lambda$ [*ibid.*]. For each sample two calculations of the suite of IOPs were made. The first was made

distribution The following four size distributions functions were assessed, expressed in radial terms for algebraic simplicity:

1. The special –7/2 generalised inverse Gaussian distribution [Alexandrov & Lacis 2000].

$$F(r) = ASF \frac{r^{-7/2} r_{eff}^{5/2}}{\sqrt{2\pi v_{eff}}\,(1+3v_{eff}+3v_{eff}^2)} \exp\left[\frac{1}{2v_{eff}}\left(2-\frac{r_{eff}}{r}-\frac{r}{r_{eff}}\right)\right] \qquad (2.5)$$

2. The Standard distribution [Hansen & Travis 1974]

$$F(r) = ASF\, r^{[(1-3v_{eff})/v_{eff}]} \exp[r/(r_{eff}\, v_{eff})] \qquad (2.6)$$

3. The 0^{th} order log normal distribution [Hansen & Travis 1974, Jonasz & Fournier 1996]

$$F(r) = ASF \exp\left[\frac{-(\ln(r)-\ln(r_g))^2}{2\sigma_g^2}\right] \qquad (2.7)$$

where $r_g = r_{eff}/(1+v_{eff})^{5/2}$ and $\sigma_g^2 = \ln(1+v_{eff})$.

4. The Junge distribution [Junge 1963, Bader 1970]

$$F(r) = ASF\, r^{-\xi} \qquad (2.8)$$

In addition to the above distributions, a further approximation was assessed:

5. A single size approximation of $d=d_{eff}$

and inherent optical properties that are derived from them, should be considered as representative theoretical values generated for the sole purpose of comparing the optical properties of equivalent size distributions. Accurate determinations of $I+\varepsilon$, in the context of the anomalous diffraction approximation, would require additional use of attenuation or scattering data, not available to this study [Bricaud & Morel 1986, Stramksi *et al.* 1988].

All refractive index determinations, and subsequent optical modelling runs, were made with Chl *a*-specific data to negate the impact of varying biomass concentration upon model performance assessment. Both algal absorption and size distribution data, as discussed above, were normalised by measured Chl *a* values i.e. $a_\phi(\lambda)$ and $F(d)$ were simply divided by the appropriate Chl *a* concentration. Whilst Chl *a*-specific phytoplankton absorption is a common bio-optical parameter [e.g. Bricaud *et al.* 1995], Chl *a* -specific size distributions are rarely used. However, test results employing absorption and size data normalised to Chl *a* concentrations both before and after optical modelling confirmed that such scaling made no impact upon the refractive index and efficiency factor analyses.

2.2.6 Equivalent Size Distributions

All size distributions were expressed in equivalent terms to the processed algal spectral density measurements: a diameter range of 1 to 100 μm, at a 1 μm bin spacing. Equivalent distributions were calculated using the same effective diameter as the corresponding measured size distribution and scaled to the total projected surface area $<SA>$ of the measured algal size distribution, as given by:

$$< SA > = \int_1^{100} \frac{\pi}{4} d^2 F(d) d(d) \qquad (2.4)$$

The *ASF* (Area Scaling Factor) term is introduced here as the total projected surface area scaling parameter. i.e. it is used to manipulate the magnitude of the equivalent distributions by matching the total projected surface area to that of the measured

where $a_\phi(\lambda)$ is the algal absorption coefficient ($m^2 mg^{-1}$), $\overline{Q}_a(\lambda)$ is the absorption efficiency factor (where the overbar signifies the mean efficiency factor of a particle population), d is the particle diameter (m), $F(d)d(d)$ is the number of particles per unit volume in the size range $d \pm \frac{1}{2} d(d)$, and λ denotes wavelength (nm). Using the experimental algal absorption coefficients and size distribution data as described above, $\overline{Q}_a(\lambda)$ can therefore be calculated for natural algal assemblages. Employing the anomalous diffraction approximation [Van de Hulst 1957],

$$Q_a(\lambda) = 1 + \frac{2e^{-\rho'}}{\rho'} + 2\frac{e^{-\rho'} - 1}{\rho'^2} \qquad (2.3)$$

dimensionless absorption efficiency factors can be expressed in terms of the optical thickness $\rho' = 4\alpha n'$, where α is the Mie size parameter $d\pi/\lambda$, and $n'(\lambda)$ is the imaginary part of the refractive index. Equations (2.2) and (2.3) can thus be employed iteratively to derive n' for an algal population. To allow calculations of additional inherent optical properties, namely attenuation and scattering coefficients, representative values of the real part of the refractive index were also derived. The Kramers-Kronig relations [Bohren & Huffman 1983, Bernard *et al.* 2001] were employed to derive spectral variations in the real part of the index, typically denoted as $\Delta n(\lambda)$, from the imaginary part of the index. The Kramers-Kronig (KK) relations are used as a replacement for the Ketteler-Helmholtz theory of Bricaud & Morel [1986], which employs Lorentzian oscillators. The KK relations describe the mutual dependence of the real and imaginary parts of the refractive index through dispersion, as does Ketteler-Helmholtz theory, but it is essentially more simply applied than the tedious and sometimes inaccurate use of summed oscillators.[Stramski *et al.* 1988]. Computational difficulties in the KK relations, specifically the evaluation of the Cauchy principal integral, were overcome using a Hilbert transform in Matlab (R14, The MathWorks) on the imaginary part of the refractive index to calculate $\Delta n(\lambda)$.The central value of $n(\lambda)$ around which $\Delta n(\lambda)$ varies, denoted as $1+\varepsilon$, was fixed at 1.05 for all samples, chosen as a representative value for phytoplankton [Bricaud & Morel 1986, Bricaud *et al.* 1988]. Note that both the $n(\lambda)$ data,

fit was then subtracted from the total measured size distribution to obtain the algal particle size distribution. These distributions were extrapolated to a minimum size of 0.7 μm (nominal GF/F pore size) by fitting a log-normal function (Equation 2.7, $\nu_{eff} = 0.5$) to the minimum measured diameter. Algal size distributions were also extended to an upper limit of 100 μm by extrapolation with a fitted Jungian distribution of exponential slope ξ=4. Finally, data for optical analyses were resampled to linear size bins of 1 μm, with a range of 1 μm to 100 μm, through calculation of the spectral density.

2.2.4 Pigments

Pigments were analysed using High Performance Liquid Chromatography (HPLC). Seawater was filtered through 25 mm GF/F filters and filters stored frozen in liquid nitrogen until analysis. Filtration volumes were adjusted to maintain approximately constant amounts of material on the filter and ranged from 0.1 l to 2 l. Pigments were extracted in acetone, containing *trans*-β-apo-8′-carotenal internal standard, with the aid of ultrasonication and clarified by centrifugation. Analysis of pigments followed the reverse-phase HPLC procedure outlined by Barlow *et al.* [1997] using a 3 μm Hypersil MOS2 C8 column (100 x 4.6 mm), a Varian ProStar pump, a Thermo Separations AS3000 autosampler, a Thermo Separations UV6000 diode array absorbance detector, and ChromQuest chromatography software. Pigments were detected at 440 and 665 nm, identified by retention time and on-line diode array spectra, and quantified relative to the internal standard. Chlorophyll *a* standard and *trans*-β-apo-8′-carotenal were obtained from Sigma-Aldrich Ltd. Other pigment standards were purchased from the DHI Institute for Water and Environment, Denmark.

2.2.5 Refractive Index Determinations

The absorption coefficient of a phytoplakton population can be described by the following expression [Morel & Bricaud 1986]:

$$a_\phi(\lambda) = \frac{\pi}{4}\bar{Q}_a(\lambda)\int_0^\infty F(d)d^2d(d) \qquad (2.2)$$

manner as the samples. Filtration volumes were adjusted to maintain a large amount of material on the filter while avoiding excessive clogging, and varied between 2 l and 0.1 l. Raw optical density values at 438 nm, corrected for blank absorption, ranged from 0.9 (Chl a = 195 mg m^{-3} with 100 ml filtered) to 0.4 (Chl a = 0.5 mg m^{-3} with 2000 ml filtered). Absorption coefficients were calculated using the pathlength amplification factor of Roesler [1998], assuming a null-point correction at 750 nm. Detrital measurements were made using methanol extraction on the filter, followed by re-reading in the spectrophotometer [Kishino *et al.* 1985]. Phytoplankton absorption $a_\phi(\lambda)$ data were then obtained by subtraction of detrital absorption $a_d(\lambda)$ from total particulate absorption $a_p(\lambda)$.

2.2.3 Particle Size Distributions (PSD)

Particle size measurements were made using a 128 channel Coulter Multisizer II with either a 50 µm or 140 µm aperture in manometer mode, using freshly prepared 0.2 µm filtered seawater as both blank and electrolyte. Choice of aperture size was dictated by size of the dominant algal species, with 140 µm used for all samples other than those dominated by the small pelagophyte *Aureococcus anophagefferens*. Samples were diluted to keep coincidence levels below 10%, and 40 ml of sample was typically counted. Particle size distributions measured in this manner pertain to the total particle population. A numerical technique was employed to fractionate measured size distributions into algal and non-algal components, designed to produce data analogous to the phytoplankton absorption data fractionated using the methods of Kishino *et al.* [1985]. The detrital component of the particle population was assumed to obey a Junge distribution (Equation 2.8), with diameters ranging from 0.7 µm to 100 µm, in log-spaced bins. An inverse anomalous diffraction model, employing a Nelder-Mead (simplex) non-linear optimisation routine to solve for magnitude N_0, was then used to fit measured detrital absorption $a_d(\lambda)$. An imaginary refractive index of n'=0.001066 exp(-0.007168λ) was employed [Stramski *et al.* 2001], with the implicit assumption that all non-chlorophyllous matter retained on the GF/F filters have similar refractive index characteristics, e.g. detritus and bacteria [Morel & Ahn 1990]. The detrital size distribution resulting from the

2.2 Methods

2.2.1 Approach

Bio-optical measurements were made on near-surface samples from diverse water types, ranging from the near oligotrophic to high biomass algal blooms dominated by a variety of algal species. Sampling was conducted from 1999 to 2003 in the southern Benguela from a variety of platforms (see Table 2.1), and thirty-four samples in total were analysed for this study. Principal measurements consisted of particulate absorption, particle size distributions and intra-cellular pigments. Identification of dominant algal species and groups were made using a combination of microscope analysis of fresh and preserved samples, and chemotaxonomic information from HPLC pigment analyses. Particulate data were separated into algal and detrital components, and inverse anomalous diffraction models [Bricaud & Morel 1986], in combination with refractive index dispersion models [Bernard *et al.* 2001], were used to derive algal refractive index data. These data were employed to assess the ability of several, common size distribution formulations to simulate the optical properties of algal populations calculated with measured size distributions. Equivalent size distributions were scaled to have the same total projected area and effective diameters as the measured size distributions. The performance of the equivalent distributions was assessed with regard to their ability to simulate the absorption, attenuation, scattering, backscattering and package effect parameter as both one- and two- parameter formulations.

2.2.2 Particulate Absorption

Particulate absorption data were measured with the quantitative filter pad technique [Yentsch 1962, Roesler 1998] using a Shimadzu UV-2501 spectrophotometer equipped with an ISR-2200 internal integrating sphere. Discrete seawater samples were filtered under less than 10 mm mercury pressure using Whatman GF/F filter pads, which were placed at the entrance port of the sphere, and scanned from 350 nm to 750 nm using an air reference and baseline. In cases where filters could not be read immediately, they were stored frozen in liquid nitrogen. Blank filter pads were prepared by filtering several hundred ml of Milli-Q water through fresh GF/F filters, which were then read in the same

identical moments display the same optical characteristics [Hansen &Travis 1974, Hu & Stamnes 1993, McGraw *et al.* 1998], where the *k*th diametric moment of a size distribution is given by:

$$< d^k > = \int_0^\infty d^k \, F(d) \, d(d) \qquad (2.1)$$

where d is the particle diameter (m), and $F(d)\ d(d)$ is the number of particles per unit volume in the size range $d \pm ½\ d(d)$. The best single parameter describing the optical properties of a size distribution is the effective radius r_{eff} or diameter d_{eff} – the ratio of the third to second moment ($<d^3>/<d^2>$), or the mean volume to surface area ratio of the distribution [Hansen & Travis 1974, Lacis *et al.* 1992]. An additional parameter of importance is the effective variance v_{eff} ($<d^4><d^2>/<d^3>$-1), which describes the width of the distribution [Hansen & Travis 1974, Alexandrov & Lacis 2000]. Using size distributions of dissimilar shapes but identical effective diameters, optical properties have been accurately matched in a variety of cases: attenuation coefficients, single scattering albedos and asymmetry parameters for water clouds [Hu & Stamnes 1993], aerosols [Alexandrov & Lacis 2000], and non-spherical ice crystals [Grenfell & Warren 1999]; and phase functions for aerosols [McGraw *et al.* 1998]. The dependence of particle optical properties upon effective radius, given an appropriate distribution function, has been shown to hold even when considering distributions of different shape, skewness, width and modality [Hu & Stamnes 1993].

This study seeks to establish whether a moment-based approach can be employed to define single parameter equivalent size distributions for the simulation of algal optical properties through a wide range of algal assemblage types. A functional size distribution form that is based upon optical equivalence rather than the replication of sometimes complex observed phytoplankton size distributions would have application in bio-optical and ocean colour modelling and inversion techniques. Such techniques are of particular relevance to the bio-optical monitoring and detection of harmful algal blooms.

populations are rarely monospecific, and the use of log-normal or gamma distributions has been restricted to application with total marine particle distributions, either decomposition techniques to describe measured distributions [Campbell 1995, Jonasz & Fournier 1996], or distribution functions suitable for oligotrophic waters [Risovic 1993]. The most commonly used distribution type for marine particulate, with specific regard to modelling optical properties, is the power law or Junge distribution [Junge 1963, Bader 1970]. The Junge distribution has been used to describe marine particle distributions for angular scattering function inversions [Morel 1973, Twardowski 2001], determine relationships between beam attenuation spectral shape and Junge distribution slope [Kitchen *et al.* 1982, Boss *et al.* 2001], establish backscattering budgets for marine particulate types [Morel & Ahn 1991], and provide basis vectors in reflectance inversion schemes [Roesler & Boss 2003]. However, such applications have typically considered the total marine particle population, as opposed to the chlorophyllous fraction which is under consideration in this study. Particle size distributions in phytoplankton-dominated waters typically display complex shapes, with variable intermediate maxima associated with the presence of dominant phytoplankton groups or species [Sheldon 1972, Jonasz & Fournier 1996]. Such complex size distributions deviate markedly from the smooth exponential representation of a Junge distribution [Bernard *et al.* 2001]. Thus, whilst a Junge distribution offers a simple scheme conforming to general trophic and dynamic paradigms [Sheldon & Parsons 1967, Sheldon 1972], and allows robust application to optical inversion, there is some doubt as to whether it is the most suitable function to describe algal optical properties, particularly in productive waters [Kitchen 1982, Jonasz & Fournier 1996, Boss *et al.* 2001].

An alternative approach, from an optical perspective, to finding best-fit functions to measured size distribution data is to consider simply parameterised equivalent size distributions: formulations that, whilst dissimilar in distribution shape, can reproduce the optical properties of polydispersed particle populations. The approach has been successfully employed by atmospheric physicists to describe the optical properties of aerosol and cloud size distributions for the purposes of radiative transfer inversions. Central to the concept of equivalent distributions is that dissimilar size distributions with

2.1 Introduction

Phytoplankton size is of considerable importance to phycologists, exerting a strong influence upon metabolic rates and physiological behaviour [Banse 1976, Finkel & Irwin 2000, Raven & Kubler 2002], algal optical properties [Morel 1973, Morel & Bricaud 1981, Stramski & Kiefer 1991], algal cell density, biomass, and carbon concentrations [Agusti *et al.* 1987, Montagnes *et al.* 1994] and physical behaviour [Raven 1986, Rodriguez *et al.* 2001]. There is thus a need to provide simple descriptors of algal size, and formulations for algal size distributions, that can account for both morphological variations and the polydispersity typically displayed by phytoplankton populations. Such schemes, by reducing algal size descriptors to one or more proxy parameters, can allow a greater understanding of cultured and natural algal populations from optical, physiological and ecological perspectives. In addition, size distribution formulae for marine particle populations allow the rapid and semi-continuous assessment of marine particle size variability through the application of inversion techniques to marine optical measurements [Boss *et al.* 2001, Twardowksi *et al.* 2001, Roesler & Boss 2003].

The effects of morphological variations on size estimates can be overcome to first order through volume equivalence schemes, either explicitly with geometrical calculations from microscopic observations [Montagnes *et al.* 1994] or implicitly through volume-based particle sizing techniques such as the Coulter method [Sheldon *et al.* 1972, Olivieri 1985]. However, whilst the Coulter Counter and analogous instrumentation allow measurements of marine particle size distributions to be made with relative ease, there still appears uncertainty as to whether such distributions can be approximated using analytical formulations, or characterised through simple descriptors.

A variety of distribution formulations have been employed to represent both phytoplankton and total marine particle distributions, typically from fitting such functions to measured size distribution data. Monospecific phytoplankton cultures display expectedly narrow size distributions, and can be represented by log-normal [Bricaud & Morel 1986] and gamma [Risovic 1993] distributions. However, marine phytoplankton

Chapter 2

Optically Equivalent Size Distributions of Natural Phytoplankton Assemblages

The study necessarily addresses several issues relevant to characterising the optical properties of natural algal assemblages; issues distinct in their nature but closely inter-linked through their relevance to ocean colour. The structure of the study is deliberately chosen to reflect these considerations, and is specifically written as four self-contained chapters – the last of which integrates the various aspects of algal optical characteristics addressed in the first three. It is hoped that such a format promotes clarity, and ultimately aids in the greater understanding of phytoplankton optics and ocean colour that is the major aim of this study. A table of notation for the entire thesis is given in Appendix III.

simplest geometry capable of simulating the observed angular scattering of algal cells [Quinby-Hunt *et al.* 1989]. Chapter 4 thus investigates the suitability of the two-layered spherical model [Aden & Kerker 1951] for the simulation of the major IOPs of algal populations, with a particular focus on algal backscattering characteristics. Intra-cellular structure and micromorphometrics, appropriate refractive index ranges and methods of determination, detailed comparisons of homogeneous vs. heterogeneous IOPs for both single cells and populations, and a preliminary validation of the two-layered model are all undertaken. The parameterisations and insights offered by the previous two chapters, in addition to a wide range of data from the literature, are all used to construct algal IOP models based on a two-layered spherical geometry. Such models move towards allowing the holistic description of the suite of algal IOPs necessary to quantitatively describe ocean colour, based on known values of core causal variables.

The final chapter of the study seeks to integrate the results of the previous chapters, in the form of a reflectance inversion algorithm for use with hyperspectral remote-sensing reflectance data. Employing the frequently used reflectance approximation [Morel & Prieur 1977, Roesler & Perry 1995, Zaneveld 1995], the algorithm seeks to simulate measured reflectance data by iteratively manipulating the absorption and backscattering of the algal assemblage and other major constituents. This allows the quantitative derivation of algal IOPs and biomass. In addition, by using the algal IOP model previously discussed, the algorithm allows an estimate of the major algal optical causal variables from reflectance data: descriptors of assemblage effective size and relative accessory pigment concentrations. Algorithm performance is tested with an independent set of bio-optical data gathered in the southern Benguela, encompassing a wide range of water types and natural algal assemblages. In addition to providing the basis for operational detection and monitoring of HABs through autonomous bio-optical sensors, the algorithm returns allow further comment on the nature of particulate and algal backscattering in the highly productive waters of the Benguela upwelling system.

the southern Benguela [Pitcher *et al.* 1998]. However, establishing simple descriptors for algal cell diameter, and a sufficiently accurate means of simulating the effects of size on algal IOPs, is complicated by the typically complex particle size distributions of natural algal populations. Chapter 2 thus investigates the use of equivalent particle size distributions, and the means of effectively and simply parameterising the IOPs of algal assemblages with regard to effective cell diameter.

Understanding the processes underlying algal absorption is key to the effective use of ocean colour. Chapter 3 seeks to quantify the effects of causal variables on algal assemblages in the Benguela, and establish to what extent these can be measured through inverse absorption models. In addition to the well-known effects of cell size, variations in the intracellular concentration of Chl *a* and accessory pigments are responsible for a large proportion of observed variability in algal absorption coefficients [Bidigare *et al.* 1990, Morel & Bricaud 1981]. A central construct of the analyses conducted in Chapter 3 is the use of the package-effect to decouple the effects of the three major casual variables – such data are used statistically to assess causal influence and to construct a diagnostic absorption inversion model. Accessory pigment effects have been utilised successfully in the past to identify algae using chemotaxonomic groupings from direct measurements of absorption [Hoepffner & Sathyendranath 1993, Johnsen *et al.* 1994, Millie *et al.* 1995]. These effects are analysed here as an assessment of the ability to obtain diagnostic chemotaxonomic information from inverse absorption models - a necessary intermediate step in the construction of inverse reflectance models.

A better understanding of algal backscattering is key to the effective use of reflectance algorithms for HAB applications. Given the critical role Mie modelling has played in the past in advancing the understanding of algal optical variability, it can be argued that a necessary first step is the adoption of a modelling theorem that is capable of adequately simulating algal backscattering. Ideally, such a theorem would pertain to all relevant algal optical properties, e.g. allow a realistic description of cellular absorption and backscattering using a single simulation. Given the previously discussed importance of cellular internal structure on algal scattering, the two-layered sphere appears to offer the

with the additional influence of the material responsible for inducing changes to the real part of the cellular refractive index [Morel & Bricaud 1986, Stramski *et al.* 2001]. However, whilst the absorption and total scattering of algal cultures have been successfully simulated using Mie theory [Bricaud & Morel 1986, Ahn *et al.* 1992], the few direct measurements made of algal angular scattering suggest that Mie theory is less well suited to describe backward scattering [Quinby-Hunt *et al.* 1989, Volten *et al.* 1998, Vaillancourt *et al.* 2004]. These studies, and others investigating the effect of internal cellular structure on angular scattering [Witkowsi *et al.* 1993, 1998] indicate the importance of internal structure on algal scattering at large angles [Bricaud *et al.* 1992, Kitchen & Zaneveld 1992].

Whilst causality is well understood with regard to algal absorption, and at least partially understood with regard to algal backscattering, the interpretation of ocean colour data based on a metric rooted in explicit algal optical causality has yet to be fully realised. This study seeks to construct an inverse reflectance model, suitable for HAB application, by establishing quantitative relationships between the variables causal to the optical properties of natural algal populations, the inherent optical properties that influence ocean colour, and the apparent optical properties that constitute ocean colour. The study will thus address several themes: the means of simply parameterising the IOPs of natural algal populations in terms of causal variables, testing the ability to detect causal variability in optical data from natural algal populations, and establishing optical models able to simulate algal backscattering and other IOPs. Finally, all of these structures will be integrated into a reflectance model allowing the estimation of IOPs and related causal variables through numerical inversion - a model tested with independent bio-optical data sets gathered in the southern Benguela.

Size of the algal cell, or the effective size of the algal assemblage, is known to be one of the dominant causes of variability in algal optics [Ciotti *et al.* 2002, Morel & Bricaud 1981, Raven 1984]. Size is also of considerable value in HAB applications, where bloom onset is often characterised by changes in the effective size of the algal assemblage, particularly with regard to the relatively large dinoflagellate cells commonly observed in

harmful algal groups or species, and that such a metric can be applied to data from available sensor systems within sufficiently small error margins. Understanding the variables causal to the absorption and backscattering of phytoplankton, and establishing a quantitative paradigm in which to apply such an understanding, must therefore be one of the central tenets of bio-optical oceanography as regards HABs.

Mie modelling, and the related anomalous diffraction approximation [Van De Hulst 1957], have played a central role in advancing the understanding of the processes underlying algal optical properties [Morel & Bricaud 1986, Ahn *et al.* 1992]. Algal absorption is well understood from this theoretical perspective, and is governed by three causal variables: the effective size of the algal cell or assemblage; the intracellular concentration of the pigments that are the predominant cellular absorbing material; and the spectral character of these pigments [Kirk 1975, Morel & Bricaud 1981, Morel & Bricaud 1986]. Experimental confirmation can be found from observations of cultured algae [Bricaud *et al.* 1988, Geider & Osborne 1987, Johnsen *et al.* 1997] and field studies of algal assemblages, showing absorption dependencies on both algal size and accessory pigmentation using either an empirical metric [Ciotti *et al.* 2002], a mechanistic approach [Bricaud *et al.* 1995, Lohrenz 2003], or a chemotaxonomic approach [Bricaud *et al.* 2004]. Additionally, absorption is a dominant source of light attenuation in the sea [Kirk 1980, Morel 1988], and there would thus seem considerable opportunity to utilise the signal offered by algal absorption for HAB detection through analytical ocean colour algorithms [Roesler *et al.* 2003].

Backscattering, the integrated angular scattering that is responsible for returning light to the surface of the sea, is considerably less well understood than absorption due to several factors. These include the historical difficulties of measuring the backscattering coefficient directly; an incomplete knowledge of the major sources of backscattering in the sea; and the difficulties of modelling the angular scattering properties of complex algal cells with sufficient verisimilitude [Stramksi *et al.* 2004]. Backscattering is nevertheless understood to be theoretically controlled, albeit in a less predictable manner, by the same causal variables as absorption: size and intracellular pigment configuration,

the sea. Radiometric sensor systems provide spectral reflectance or ocean colour data by measuring the light field both leaving the sea and incident to it, and offer several advantages for HAB applications. First amongst these is that ocean colour reflectance inversion algorithms offer considerable potential for HAB application through the identification of dominant algal groups and size classes [Roesler & Boss 2003, Roesler *et al.* 2003]. *In situ* radiometric data can be considered analogous to space-based ocean colour measurements, and the use of reflectance inversion algorithms allows the potential derivation of equivalent algal products from both point measurements and at the synoptic scale offered by satellite data. Passive hyperspectral radiometric sensors have several other positive attributes for autonomous HAB application: robust sensors with low power consumption; high resolution semi-continuous spectral data offering a rich signal; data that can be calibrated in absolute units; and the ability to provide validation of the satellite signal in high biomass bloom water types [Cullen *et al.* 1997, Chang *et al.* 2004].

An important construct in contemporary bio-optics is the division between inherent optical properties (IOPs) and apparent optical properties (AOPs) [Preisendorfer 1976]: this allows a quantitative evaluation of the aquatic light field in terms of the optical properties specific to the various marine constituents [Morel & Prieur 1977, Zaneveld 1995]. Of these, it is the absorbing and backscattering properties of the marine hydrosol that can be considered most important from the perspective of ocean colour applications [*ibid.*]. The ability to understand and characterise the absorbing and backscattering properties of the algal assemblage is thus central to the effective use of reflectance algorithms for HAB-related applications. It must be possible to make a distinction, through bio-optical means, between non-harmful algae, present in the majority and making an essential contribution to system productivity, and those species or algal groups deemed harmful. However, it could be argued that ocean colour data are blind to the majority of morphological and genetic distinctions underlying conventional algal taxonomy; its effective use demands instead a metric based on the variables causal to the optical characteristics of the algal cell. Successful bio-optical HAB detection thus requires that causal optical variables are identified, a metric based on causality is constructed and linked to the conventional taxonomy required for the identification of

Harmful algal blooms (HABs) are a frequent occurrence in the Benguela system (Pitcher & Calder 2000), often resulting in severe negative impacts to local marine ecosystems and communities, in addition to commercial marine concerns such as aquaculture operations. Harmful impacts of HABs, most often composed of a variety of dinoflagellate species, are associated with either the toxicity of some species present in the algal assemblage, or the high biomass such blooms can achieve. Collapse of high biomass blooms through natural causes such as nutrient exhaustion can lead to hypoxic events and in extreme cases, the production of hydrogen sulphide, frequently causing extensive mortalities of marine organisms. Effective ecosystem management requires a greater understanding of the variability of HABs as ecologically prominent phenomena, and the means of detecting and monitoring blooms in real time, through both *in situ* observation platforms and satellites.

Bio-optical methods are well suited to algal monitoring applications, offering a variety of robust, cost-effective *in situ* and satellite-borne sensor systems capable of measuring the variation of light in the sea: a signal strongly influenced by phytoplankton [Morel & Prieur 1977, Cullen *et al.* 1997]. Simple bio-optical *in situ* instrumentation, such as fluorometers, and conventional satellite-derived chlorophyll *a* products (Chl *a*) have become routine tools for the estimation of algal biomass in the sea. However, it has been demonstrated that bio-optical techniques can offer considerably more than simple algal biomass estimates, allowing the detection of changes in biomass-normalised algal optical properties and thus assemblage size and broad taxonomic identification [Bricaud *et al.* 2004, Ciotti *et al.* 2002, Roesler *et al.* 2003]. The provision of some form of assemblage description from bio-optical measurements offers significant advantages over simple biomass estimates. These include the detection of precursive and formative bloom conditions; an enhanced capacity to determine whether a bloom is of a potentially harmful nature; a better facility to monitor bloom growth, movement and decay; and a greater understanding of the bio-physical dynamics underlying bloom formation.

A wide variety of both passive and active *in situ* bio-optical sensors is currently commercially available for the purposes of autonomous, real-time algal monitoring, most commonly measuring the absorbing, scattering, fluorescent and radiometric properties of

Chapter 1

Introduction

Abstract

An analytical framework for the simulation and quantitative interpretation of ocean colour data is presented, providing an inverse reflectance algorithm designed for the detection of harmful algal blooms. The adopted framework focuses on establishing quantitative relationships between optically important algal intracellular properties and inherent optical properties (IOPs), such as the absorption and backscattering coefficients, and the resultant effects on remote-sensing reflectance.

A principal aim of the study is to establish the determinant variables of the IOPs associated with natural algal assemblages, and provide a means of simulating these IOPs. Algal size is an important determinant of optical properties, and the study demonstrates algal IOP simulation, using equivalent particle size distributions that can be simply parameterised with regard to effective cell diameter. Statistical analyses of causal variability are also conducted on absorption data from a variety of natural algal assemblages, revealing the relative importance of cell size, intracellular Chl *a* concentration, and accessory pigment complement. An improved understanding of algal angular scattering is regarded as key to the analytical modelling of ocean colour, and the use of two-layered spherical models for the simulation of algal scattering properties is investigated. Preliminary validation of the combined use of the equivalent size and two-layered models indicates that they are capable of adequately simulating the remote-sensing reflectance properties of high biomass bloom waters.

The equivalent size distribution model, in conjunction with an algal optical model employing a two-layered geometry, and a spectral mixing model based on common algal groupings for upwelling systems, is used to construct a reflectance inversion algorithm. Designed for use with hyperspectral remote-sensing reflectance data, the algorithm is tested with an independent data set representing a wide variety of water types in the southern Benguela. The algorithm allows the derivation of Chl *a* concentrations, an algal size descriptor, and coarse accessory pigment identification, with sufficient accuracy to indicate that it could be of considerable use as a bio-optical means of monitoring algal dynamics and detecting harmful algal blooms.

Table of Contents

using the measured algal size distribution (calculated as described in section 2.2.3) with corresponding refractive index data (as described in section 2.2.5) - these are referred to as the "measured" properties. The second was made using the equivalent algal size distribution (calculated as described in section 2.2.6) using exactly the same refractive index data as for the "measured" calculations – these are referred to as the "equivalent" properties. Again, it should be noted that the purpose of the exercise is to assess the ability of a simple equivalent size distribution to match the IOPs calculated using a relatively complex measured size distribution.

The ability of the equivalent size distribution to match the IOPs calculated from the measured size distribution were assessed using the mean and standard deviations (SD) of the RMS errors (in percent) of the entire data set for each wavelength, as given by

$$RMS\,error(\lambda)=\left[\sqrt{mean\left(\frac{a_{equiv}(\lambda)-a_{meas}(\lambda)}{a_{meas}(\lambda)}\right)}\right]^2 \qquad 2.10$$

$$SD\,of\,RMS\,error(\lambda)=\left[\sqrt{SD\left(\frac{a_{equiv}(\lambda)-a_{meas}(\lambda)}{a_{meas}(\lambda)}\right)}\right]^2 \qquad 2.11$$

where a_{equiv} is the modeled absorption of the equivalent size distribution, and a_{meas} is the modeled absorption of the measured size distribution. The above expression are for absorption – analogous expressions are employed for other IOPs.

The Aden-Kerker [1951] formulations, as provided by the Fortran code of Toon & Ackerman [1981] were employed for all forward optical modelling, in a combined Matlab/Fortran environment. The Aden-Kerker formulations allow the absorbing and scattering properties of a two-layered particle to be calculated using size and refractive index data as input, in a way analogous to Mie theory use for a homogeneous particle. The suitability of the Aden-Kerker formulations for homogenous particle geometry was confirmed by testing sample results against the Fortran code of Bohren & Huffman [1983].

Table 2.1 General description of sampled assemblages, with Chl *a* ranges in mg m^{-3}, and phytoplankton absorption $a_\phi(674)$ ranges in m^{-1} (see Appendix II).

Date	Location/Cruise	Chl *a* ($mg\ m^{-3}$)	$a_\phi(674)$ (m^{-1})	Dominant Assemblage Types
1999	Lamberts Bay/shore based	50-120	0.8-1.8	Dinoflagellates
1999	Saldanha Bay/shore based	9-12	0.3-0.4	*Aureococcus anophagefferens*
1999	Southern Benguela/Benefit	0.5-14	0.02-0.2	Mixed
2000	Lamberts Bay/SBHABE	19-46	0.4-0.8	Diatoms/Dinoflagellates
2001	False Bay/shore based	19	0.36	*Karenia mikimotoi*
2001	Lamberts Bay/shore based	2-195	0.04-3.9	Dinoflagellates/Ciliates
2003	Saldanha Bay/shore based	12-14	0.25-0.35	*Aureococcus anophagefferens*

Table 2.2 Maximal mean RMS errors (%), with standard deviations in brackets, between measured and equivalent distributions. The single size distribution is assessed with regard to efficiency factors rather than volume coefficients due to the unknown volume integral associated with a single size– mean efficiency factor errors for the inverse Gaussian are shown for comparison. The two most effective distributions for potential application are in bold. Errors for phytoplankton attenuation c_ϕ, scattering b_ϕ, absorption a_ϕ, backscattering $b_{b\phi}$, and package effect parameter Q_a^* are shown. Realistic values of the maximum expected errors can be obtained by summing the mean RMS error and standard deviation.

Distribution	ν_{eff} (d/less)	Error c_ϕ (%)	Error b_ϕ (%)	Error a_ϕ (%)	Error $b_{b\phi}$ (%)	Error Q_a^* (%)
Inverse Gauss	Measured	3.1 (4.6)	4.6 (5.8)	0.9 (3.1)	9.6 (9.1)	1.4 (4.9)
Inverse Gauss	**0.63**	**2.8 (4.9)**	**3.9 (5.5)**	**1.0 (3.8)**	**7.7 (12.7)**	**1.1 (4.6)**
Standard	Measured	5.5 (4.2)	7.8 (5.2)	1.9 (2.7)	8.1 (17.4)	0.8 (5.7)
Standard	**0.63**	**4.9 (4.1)**	**6.4 (4.8)**	**0.9 (3.5)**	**8.4 (17.1)**	**1.9 (5.2)**
Log-normal	Measured	3.4 (8.4)	3.1 (10.8)	18.3 (11.8)	19.6 (17.9)	8.4 (7.9)
Log-normal	0.63	2.7 (6.2)	2.6 (7.8)	18.3 (1.4)	19.5 (12.0)	8.8 (6.1)
Junge	Variable	36.6 (12.9)	36.7 (12.8)	27.4 (8.0)	14.4 (22.0)	33.3 (28.5)
		Error Q_c	Error Q_b	Error Q_a	Error Q_{bb}	Error Q_a^*
Inverse Gauss	Measured	3.0 (4.7)	4.3 (5.4)	0.6 (2.7)	8.6 (9.7)	1.4 (4.9)
Single size	-	6.7 (25.3)	8.1 (24.6)	14.5 (8.2)	33.3 (17.6)	4.1 (3.0)

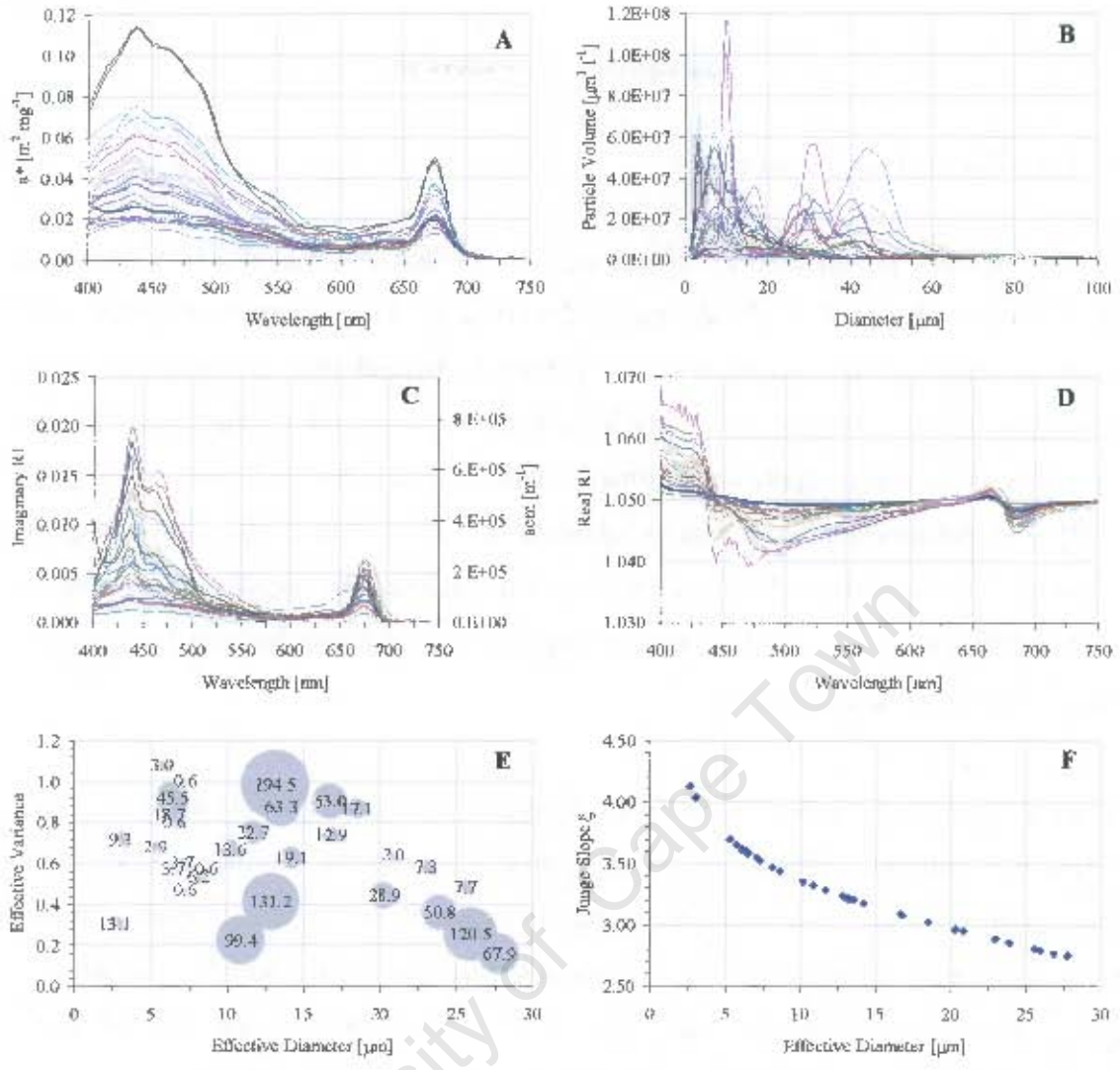

Figure 2.1 Optical and size related data for all samples analysed. A) Chl *a*-specific phytoplankton absorption, B) Algal size distributions by volume, C) Imaginary part of the phytoplankton refractive index, D) Real part of the phytoplankton refractive index, E) Effective diameter vs. effective variance of the phytoplankton size distributions, where bubble size represents measured Chl *a* concentrations [mg m^{-3}], F) Slope ξ of the equivalent effective diameter matched Junge phytoplankton distributions. The complex and sometimes highly peaked algal size distributions can be observed in B). Distributions dominated by the pelagophyte *A. anophagefferens* are scaled by 0.2 to facilitate comparison.

2.3 Results and Discussion

All Chl *a*-specific phytoplankton absorption, size distributions and refractive index data are displayed in Figure 2.1. The absorption data (Fig. 2.1A) demonstrate the effects of varying assemblage size and pigmentation [Morel & Bricaud 1981, Bricaud *et al.* 1988]; the effects of which can also seen in the imaginary refractive index data (Fig. 2.1C), the magnitudes of which compare well with algal culture data [Ahn *et al.* 1992, Volten *et al.* 1998]. The multimodal phytoplankton volume distributions (Fig. 2.1B) are typical of the productive, phytoplankton-dominated waters of the southern Benguela, and demonstrate the difficulties of simulating the complex shapes of natural phytoplankton distributions using simple distribution functions.

Figure 2.1E shows the range of effective diameter and variance data in relation to algal Chl *a* concentrations. There would appear to be little systematic variation with regard to shape of the algal size distribution and algal biomass, and the range of effective variance with regard to Chl *a* concentrations demonstrates that many of the high biomass algal blooms observed in the Benguela are composed of multiple species of a wide range of sizes [Pitcher *et al.* 1998]. The range of effective variance data compares well with algal culture data [Volten *et al.* 1998], although the variance data from this study typically display higher values, as might be expected from more widely polydispersed natural algal assemblages. Figure 2.1F shows the relationship between Junge slope ξ and effective diameter for the matched Junge distributions: the range of slope values falls between $2.74 < \xi < 4.2$, a similar range of values to those previously published for total marine particulate [Boss *et al.* 2001, 2001a, Twardowski *et al.* 2001]. The relationship between ξ and d_{eff} can be closely approximated with a power law function ($\xi = 4.94\, d_{eff}^{-0.17}$, $r^2 = 0.99$, n=34), but such an approximation is only appropriate to the diameter range (1 to 100 μm) and linear size interval (1 μm) used for this study [Boss *et al.* 2001].

2.3.1 Optical Properties of Equivalent Size Distributions

The two equivalent size distributions previously used for analogous atmospheric work, the inverse Gaussian [Alexandrov & Lacis 2000] and Standard [Hansen & Travis 1974], perform well in simulating the optical properties of algal assemblages. Maximal RMS errors and their standard deviations are reported in Table 2.2 & Figure 2.2 for all distributions, calculated in percentage terms for all optical properties relative to the derived optical properties of the full, i.e. measured, distributions. Realistic values of the maximum expected errors can be obtained by summing the mean RMS error and standard deviation – the single values in Table 2.2 represent the largest spectral errors seen in Figure 2.2. The best performing inverse Gaussian distribution therefore appears capable of simulating beam attenuation c and total scattering b to within 10%, absorption a and package effect parameter Q_a^* to within 6%, and backscattering b_b to within 20%. The Standard distribution, offering a simpler algebraic expression, gives similar performance with the exception of slightly higher maximum backscattering errors of ~25 %.

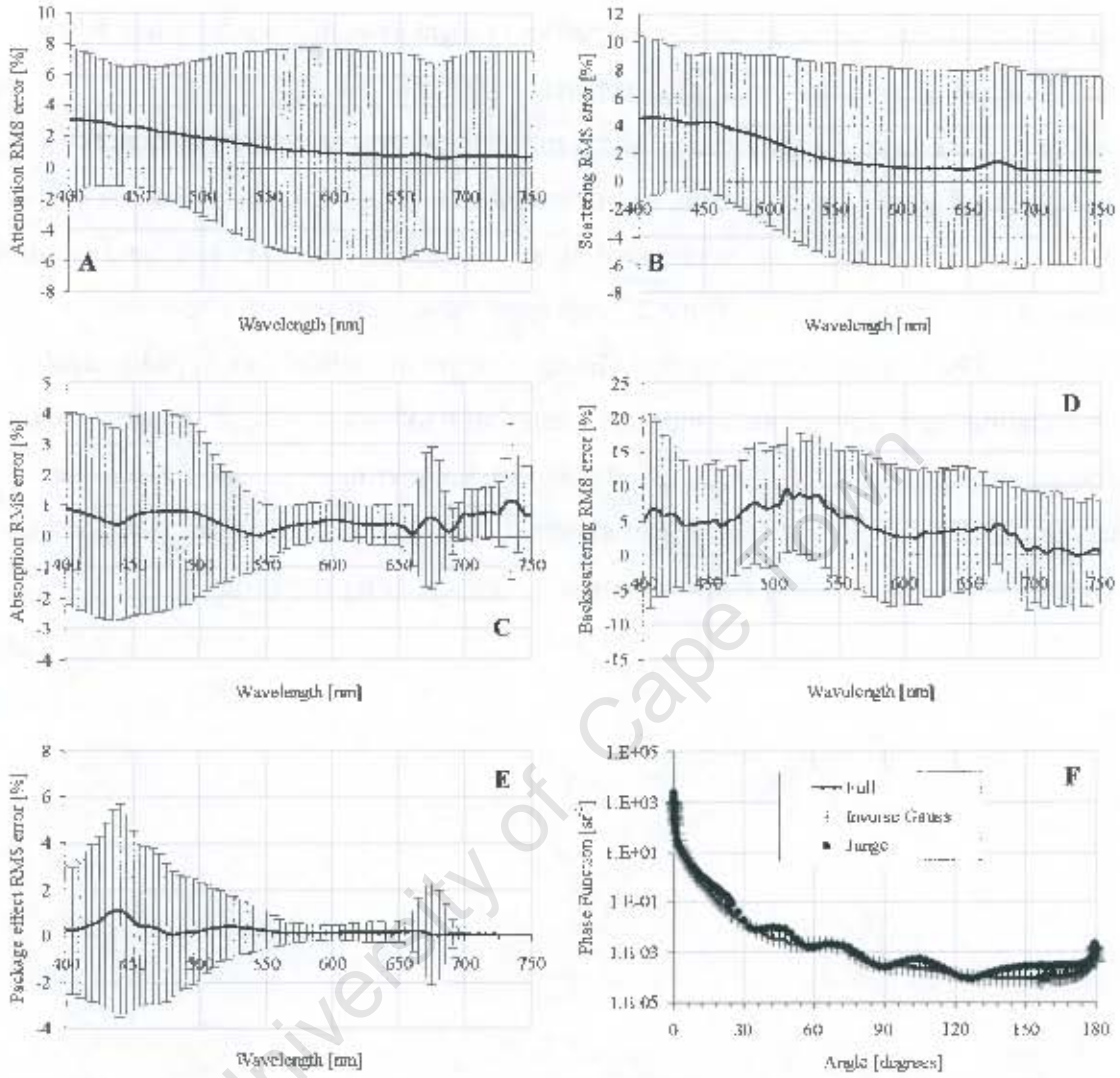

Figure 2.2 Mean spectral RMS errors and standard deviations of the best performing inverse Gaussian equivalent distribution. A) Attenuation coefficient, B) Scattering coefficient, C) Absorption coefficient, D) Backscattering coefficient and E) Package effect parameter. High magnitude morphology-dependent resonance effects [Mishchenko & Lacis 2000] can cause extremely high mean errors in phase function simulations, and such errors are therefore not calculated for the phase function. Figure 2.2F shows a comparison between computed phase functions from the full, inverse Gaussian and Junge distributions at 530 nm for the same example assemblage as Figure 2.3.

Both these distributions appear capable of reproducing salient bio-optical variables with sufficient accuracy for inversion application through a wide range of algal assemblage types. Of particular importance is the ability of the inverse Gaussian and Standard distributions to reproduce spectral absorption coefficients and package effect parameters accurately (< 6 %), as phytoplankton absorption is an often dominant determinant of light attenuation in the sea [Morel 1988], and offers an optical signal with the ability to provide algal assemblage descriptors [Ciotti *et al.* 2002, Lohrenz *et al.* 2003, Bricaud *et al.* 2004].

The relatively high errors associated with the backscattering coefficient (~20%) relative to the other coefficients (~5 % to ~10 %) are presumed to be a result of the greater sensitivity to small size changes of the scattering phase function relative to integrated variables such as the attenuation or absorption coefficient [Hansen & Travis 1974, Mishchenko & Lacis 2000]. Both interference phenomena and morphology dependent resonances, at their most pronounced in the phase function [Mishchenko & Lacis 2000], are likely to result in much larger size-dependent variations (and errors) in phase function dependent variables such as the backscattering coefficient. Previous studies considering hypothetical particle polydispersions [Morel & Bricaud 1986, Stramski & Kiefer 1991] have demonstrated that the relationship between optical efficiency and particle size is considerably more complex for backscattering (which can show decadal variations in the 1 to 100 μm size range) than those for attenuation, scattering or absorption (which tend to limiting values in the same size range). It must also be appreciated that Mie formulations employing a homogenous spherical particle geometry have been shown to be sub-optimal for algal angular scattering calculations, due primarily to cellular internal structure [Quinby-Hunt *et al.* 1989, Witkowski *et al.* 1993, Zaneveld & Kitchen 1995, Volten *et al.* 1998, Witkowski *et al.* 1998]. Nevertheless, the aim of this study is to demonstrate the utility of equivalent size distributions, which appear able to reproduce the simulated backscattering properties of measured algal size distributions within an acceptable level of uncertainty.

Forcing both the inverse Gaussian and Standard distributions to a constant v_{eff} appears to have had little adverse effect on the returned errors, allowing both distributions to be expressed through two parameters for potential inversion applications: the effective diameter and a scaling parameter. The relative lack of sensitivity to v_{eff} would appear to be due at least in part to the relatively dispersed nature of the majority of the algal assemblages analysed, even in high biomass bloom scenarios. Thus, whilst the assumption of a relatively high constant v_{eff} of 0.63 appears appropriate for natural algal assemblages in productive coastal systems, application either in truly oligotrophic waters or to very highly size-constrained mono-specific blooms or cultures may require further validation.

The single size approximation would appear to offer poor returns for all optical variables (~25% to ~50% errors), with the important exception of the package effect parameter (~7% error) which offers comparable performance to the inverse Gaussian and Standard distributions (~6% to ~7% errors). The acceptable performance of the single-size package effect derivation, in comparison to the poorer performance with regard to the other optical coefficients, is likely to result both from the monotonic nature of the Q_a^* vs d_{eff} (or ρ') relationship [Morel & Bricaud 1981], and the high relative impact of the optical thickness ρ' upon direct Q_a^* calculations (Equation 2.9). Whilst Q_a and Q_a^* are obviously both directly dependent upon ρ', the average deviation of $\rho'(675)$ is four times higher than $Q_a(675)$ when considering the entire data set – thus the assemblage-averaged effective diameter and imaginary refractive index data play a greater role in the package effect calculations relative to those of the other inherent optical properties. The good performance of the single-size package-effect derivation offers a potentially extremely useful formulation: the ability to robustly express the Chl *a*-specific phytoplankton absorption of natural assemblages through a single effective diameter parameter via the package effect [e.g. Morel & Bricaud 1981].

The Junge size distribution, perhaps the most commonly used in marine optics, performed markedly less well, with errors ranging from 35% to 62% (Table 2.2). Given

the peaked nature of the measured phytoplankton size distributions, and the noted limitations of the Junge distribution for phytoplankton-dominated waters [Sheldon *et al.* 1972, Risovic 1993, Jonasz & Fournier 1996, Boss *et al.* 2001], the poor performance of the Junge distribution is not unexpected. The log-normal distribution, while offering more accurate returns than the Junge distribution, offers a mixed performance in comparison to the inverse Gaussian and Standard distributions. The log-normal returns for the attenuation and scattering coefficients (10% to 14% errors) are comparable to those of the inverse Gaussian and Standard distributions. The log-normal returns for the absorption and backscattering coefficients, and the package effect parameter, are however noticeably poorer (Table 2.2). Whilst this may be partially due to the particular 0^{th} order formulation of the log-normal distribution employed here [Hansen & Travis 1974], it is also likely to be due to the less desirable asymptotic characteristics of the log-normal distribution at higher sizes [Jonasz & Fournier 1996, Alexandrov & Lacis 2000].

Figure 2.3 details the measured and equivalent algal size distributions, and associated optical properties of a mixed dinoflagellate and diatom bloom in the southern Benguela. The example station is specifically chosen to illustrate the close simulation of optical properties using equivalent size distributions very different in shape to the highly multimodal measured size distribution. The equivalent size distributions in Fig. 2.3A are calculated using the mean effective variance of 0.63, and can therefore be parameterised using a maximum of two variables: the effective diameter d_{eff}, and the scaling parameter *ASF*. Such data demonstrate both the utility of equivalent size distributions with regard to optical simulation, and the disadvantages of replicating size distributions by matching measured shape. Simulation of the measured volume size distribution shape in Fig 2.3A would require a minimum of three discrete distributions, each described by two parameters [e.g. Campbell 1995, Jonasz & Fournier 1996]. With regard to the optical properties of the example assemblage, the close replication of all optical properties by the inverse Gaussian and Standard distributions can be observed. The approximate 7% difference between the measured phytoplankton absorption and that reproduced from the Mie modelling (Fig 2.3C) can be attributed to the errors associated with the anomalous diffraction approximation, used to derive the spectral refractive index data.

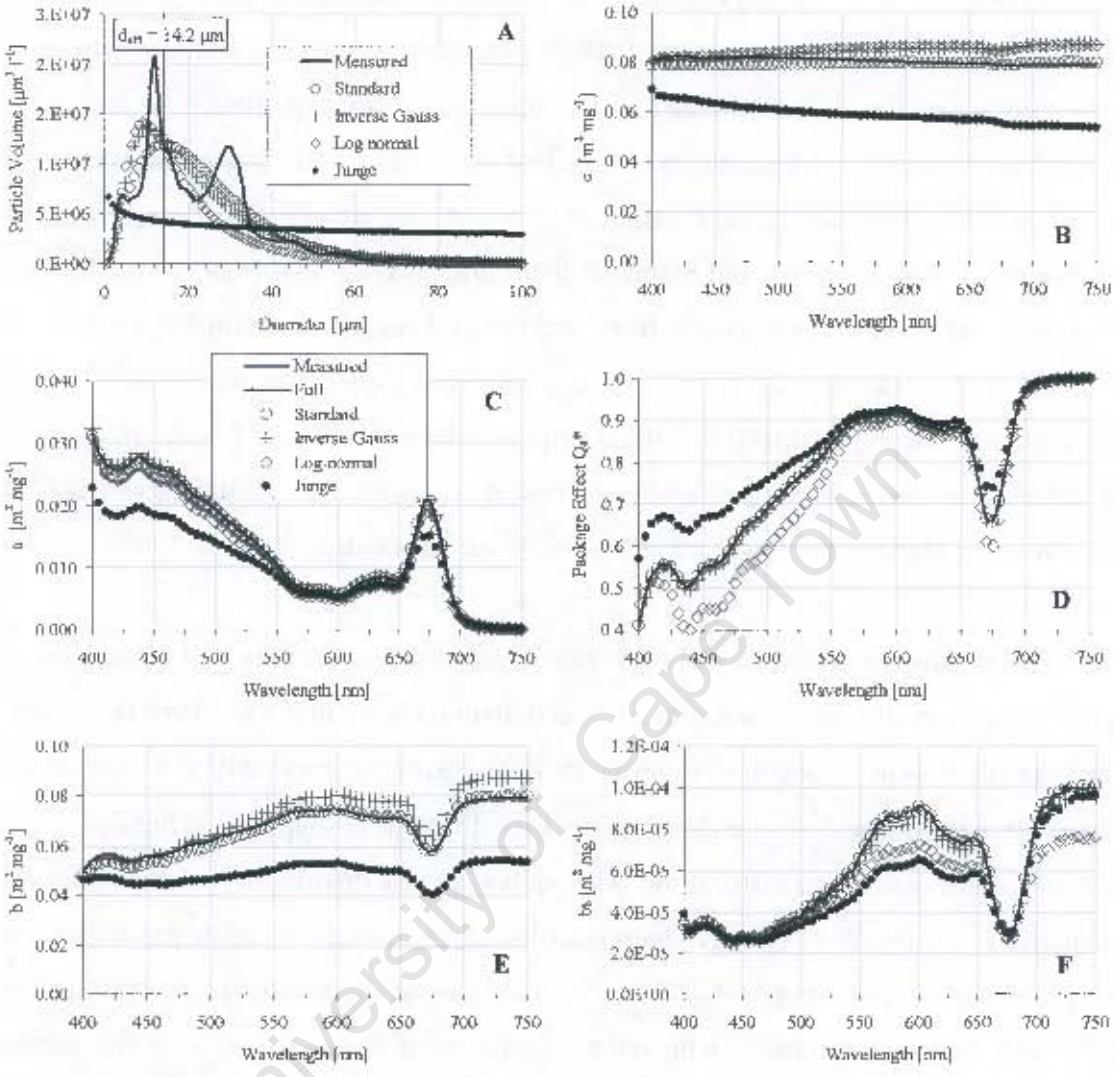

Figure 2.3 Equivalent size distributions and their inherent optical properties for an example assemblage, composed of mixed dinoflagellate and diatom species. All data are shown for Chl a=1 mg m^{-3}. Data shown are A) Measured and equivalent phytoplankton size distributions,B) Phytoplankton beam attenuation coefficient c, C) Phytoplankton absorption coefficient a, D) Package effect parameter Q_a^*, E) Phytoplankton scattering coefficient b, and F) Phytoplankton backscattering coefficient b_b. Close matches for the calculated optical properties of the equivalent inverse-Gaussian and Standard distributions can be observed, as can the difference in the shapes of the equivalent size distributions relative to the highly multimodal measured distribution.

2.4 Application and Conclusions

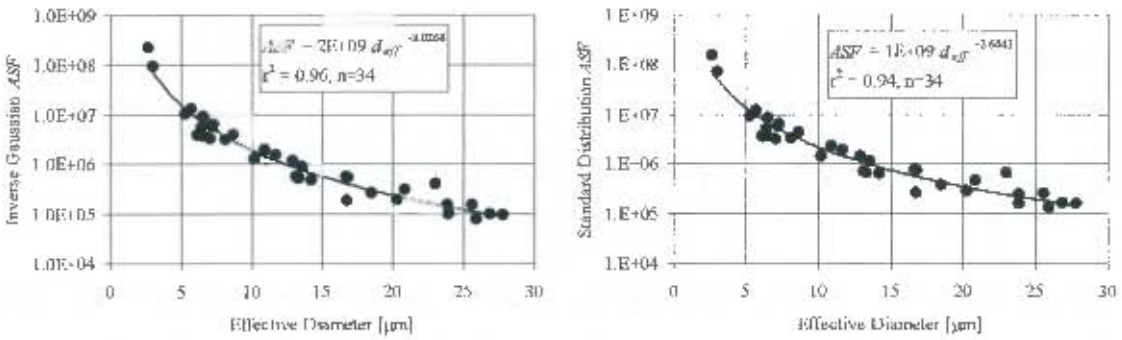

Figure 2.4 Scaling parameters *ASF* for the A) inverse Gaussian and B) Standard distributions, calculated as surface area equivalent to the thirty-four measured algal Chl *a* specific size distributions. The results suggest that *ASF* can be confidently expressed as a function of d_{eff} for a wide variety of algal assemblages for the above distributions.

Further consideration of the scaling parameter *ASF* for the inverse Gaussian and standard distributions reveals a close relationship with effective diameter d_{eff} for the samples analysed using a mean effective variance of 0.63 (Fig. 2.4). The *ASF* parameter is used to manipulate the magnitude of the equivalent distributions by matching the total projected surface area to that of the measured distribution. The ability to express the *ASF* to d_{eff} relationship using a power law allows both distributions to be parameterised using a single variable, the effective diameter (Fig 2.4). This further simplifies potential inversion of the inverse Gaussian and Standard equivalent distributions by allowing Chl *a*-specific algal size distributions to be expressed as single variable functions, assuming a mean effective variance of 0.63:

1. Inverse Gaussian Chl *a*-specific algal size distribution

$$F(r) = 2\times10^{9}\,(2r_{eff})^{3.0264}\left[\frac{r^{-7/2}\,r_{eff}^{5/2}}{7.9232}\right]\exp\left[0.7937\left(2-\frac{r_{eff}}{r}-\frac{r}{r_{eff}}\right)\right] \qquad (2.12)$$

2. Standard Chl *a*-specific algal size distribution

$$N(r)=1\times10^{9}\,(2r_{eff})^{-2.6443}\,r^{(-1.412/)}\exp[r/0.63r_{eff}] \qquad (2.13)$$

It should also be noted that it is possible to use the above expressions as simple weighting formulae without the scaling parameters shown in Figure 2.4, for example to calculate optical efficiency factors given refractive index data.

The equivalent distribution approach demonstrates that by shifting paradigm from attempting to simulate or reconstruct the shape of a marine particle distribution to simulating the optical properties of a size distribution, simple parameterisations of common size distribution formulae can be employed for optical purposes. In particular such an approach circumvents the necessity to consider the detailed structure of complex particle size distributions in biologically dominated waters, even in the case of intense algal blooms. The current study has several limitations: those of a methodological nature with regard to the derivation of algal size distributions, subsequent refractive index determinations, and the simplifications arising from the use of homogenous particle geometries in optical calculations. Nevertheless, the study demonstrates the utility of the equivalent size distribution approach, providing the ability to simulate the primary inherent optical properties of a wide range of algal assemblage types. In addition, the distributions described here allow simple size descriptions of the chlorophyllous particle population, as opposed to the more general size distribution formulations used in the past for the total marine particle population.

Chapter 3

Analysing and Modelling the Effects of Assemblage Size and Intracellular Pigmentation on Phytoplankton Absorption

3.1. Introduction

Understanding the absorbing properties of algae is a requirement for the description of light propagation through the ocean, one of the primary goals of optical oceanography. Absorption of light by phytoplankton is of considerable ecological importance: as a constraint upon photosynthetic rate, and as an often dominant source of light attenuation in natural waters [Kirk 1980, Morel 1988]. The processes causal to algal absorption are governed principally by three variables: the size of the algal cell or mean size of the assemblage, the intracellular concentration of the pigments that are the predominant cellular absorbing material, and the spectral character of these pigments [Morel & Bricaud 1981]. The ways in which these variables control algal absorption are well understood both from a theoretical perspective [Duysens 1956, Kirk 1975, Morel & Bricaud 1981], and with regard to observations of cultured algae [Agusti 1991, Bricaud *et al.* 1983, 1988, Geider & Osborne 1987, Johnsen *et al.* 1997]. In addition, field studies on algal assemblages have shown absorption dependencies on both algal size and accessory pigmentation using either an empirical metric [Ciotti *et al.* 2002], a mechanistic approach [Bricaud *et al.* 1995, Lohrenz *et al.* 2003], or a chemotaxonomic approach [Bricaud *et al.* 2004].

Algal absorption spectra thus offer a means of providing information on algal biomass, average assemblage size, and accessory pigment composition. Such information has obvious application in coastal monitoring, specifically in the detection of harmful algal blooms. The most effective realisation of such an application requires the remote measurement or derivation of algal absorption, e.g. the use of moored *in situ* instrumentation providing semi-continuous measurements in real-time, or satellite ocean colour measurements providing synoptic data [e.g. Cullen *et al.* 1997]. However, algal absorption is difficult to measure directly using autonomous *in situ* instrumentation, given currently available technologies, and cannot be measured directly from space. It thus must be derived either from measurements of total absorption [Eisner *et al.* 2003, Pegau *et al.* 1995], or using inversion techniques on spectral reflectance data [Roesler & Perry 1995, Garver & Siegel 1997, Roesler & Boss 2003]. Such methods are necessarily

reliant upon numerical techniques to derive algal absorption spectra: through either spectral deconvolution from total absorption [Roesler *et al.* 1989, Bricaud & Stramski 1990]; reflectance inversion models representing algal absorption with single [Roesler & Perry 1995] or multiple spectral basis vectors [Roesler *et al.* 2003]; empirically derived power law models [Bricaud *et al.* 1995, as cited in Garver & Siegel 1997]; or hyperbolic tangent functions [Carder *et al.* 1991]. However, the majority of such inverse models are designed for the calculation of Chl *a* concentrations - typically through single value parameterisations of the Chl *a*-specific absorption coefficient - rather than size and chemotaxonomic pigment data. Exceptions to this are the spectral mixing model of Roesler *et al.* [2003], and the phycobiliprotein-targeted models of Subramaniam *et al.* [1999], specifically designed to provide additional chemotaxonomic information on the algal assemblage.

There are a variety of techniques available to derive size and marker pigment information from direct measurements (as opposed to those derived indirectly through inverse models) of algal absorption. The spectral mixing model of Ciotti *et al.* [2002] offers a robust means of determining mean assemblage size, and the approach has been demonstrated for inverse application by Roesler *et al.* [2003]. Chemotaxonomic techniques include accessory pigment quantification using Gaussian deconvolution [Hoepffner & Sathyendranath 1993, Stuart *et al.* 1998, Lohrenz *et al.* 2003], spectral discriminant analysis [Johnsen *et al.* 1994], and fourth derivative analysis [Millie *et al.* 1995, Kirkpatrick *et al.* 2000]. These techniques, designed for direct as opposed to inverse application, and reliant upon the direct measurement of algal absorption with a high signal to noise ratio and spectral resolution, are not ideally suited to data from autonomous bio-optical instruments or satellites. The signal from these instrument systems, to which algal absorption typically makes only a partial contribution, cannot currently offer the degree of precision required by the above techniques, constructed around accessory pigment related fine structure in data from highly resolved discrete analytical methods such as the quantitative filter technique [Yentsch 1962, Roesler 1998].

Remote or autonomous bio-optical measurement systems require inverse algal optical models offering the ability to assess the viability of deriving algal size and marker pigment data, in addition to biomass proxies. Simple, robust spectral mixing algorithms, capable of inverse application, that allow determination of algal assemblage size through an empirical metric [Ciotti *et al.* 2002] and the identification of algal functional groups [Roesler 2003] have already been demonstrated. However, such models are essentially empirical in that they directly utilise admixtures of measured Chl *a*-specific absorption spectra, rather than explicitly accounting for absorption causality. This study seeks to establish the effectiveness of formulating such inverse models in terms of the assemblage descriptors causal to algal absorption: size, and intra-cellular pigment concentration and composition. The anomalous diffraction approximation (ADA) and derived package effect [Morel & Bricaud 1981] offer such a formulation: allowing algal absorption to be expressed in terms of both gross and intra-cellular Chl *a* concentration, the absorbing material forming the cell, and cellular size. The package effect expresses the effects of placing cellular material in a discrete particle as opposed to in a solution [Morel & Bricaud 1981]. It is a simple and profound expression that allows the effective decoupling of the principal causal effects on algal absorption: those of accessory pigment related spectral variability, intracellular pigment concentration, and changes in cellular size. It has been used extensively in the analysis of algal optical properties, in applications ranging from allometric photosynthetic and metabolic models [Finkle & Irwin 2000, Finkel 2001], algal fluorescence [Collins *et al.* 1985], and absorption modelling [Bricaud *et al.* 1988, Sosik & Mitchell 1991, Lohrenz *et al.* 2003].

This study will seek to implement and test an inverse algal absorption formulation expressed in terms of the package effect and spectral admixtures of appropriate unpackaged absorption spectra, based upon analyses of data from a wide variety of algal assemblages using the anomalous diffraction approximation. The explicit use of the package effect is intended to provide a model structure that, by decoupling the three primary variables causal to phytoplankton absorption, has the ability to derive algal size and marker pigment based chemotaxonomic descriptors from algal absorption data. The model is designed to form the algal absorption component [e.g. Roesler & Perry 1995] of

an inverse reflectance model for application with moored and satellite-derived bio-optical systems providing data pertaining to coastal algal dynamics. In addition, the ability to describe the absorption of a wide range of natural algal assemblages in terms of causal processes may provide further insight into characterising phytoplankton absorption from an allometric perspective.

Phytoplankton absorption, particle size distribution and HPLC pigment data from a variety of natural assemblages in the southern Benguela are used to analyse the influence of size and intracellular pigmentation on phytoplankton absorption. These data are then employed in conjunction with the anomalous diffraction approximation to construct and test several inverse phytoplankton absorption models, based on spectral basis vectors of unpackaged absorption $a^*_{\phi u}(\lambda)$, explicit values of intracellular Chl *a* concentration c_i, and a package effect parameter $Q^*_a(\lambda)$ based explicitly on the effective diameter d_{eff} of the algal assemblage. Model performance is assessed with regard to both the cost, in terms of the number of unknowns required for a solution, and the benefit, as given by the accuracy and precision of model determinations, the number of returned algal descriptors, and their potential utility in algal monitoring.

3.2 Absorption Theory and the Anomalous Diffraction Approximation

Revisiting optical theory explored in Chapter 2, the absorption coefficient of a phytoplankton population can be described by the following expression [Morel & Bricaud 1986]:

$$a_\phi(\lambda) = \frac{\pi}{4}\overline{Q}_a(\lambda)\int_0^\infty F(d)d^2\,d(d) \qquad (3.1)$$

where $a_\phi(\lambda)$ is the algal absorption coefficient (m^{-1}), $\overline{Q}_a(\lambda)$ is the absorption efficiency factor (where the overbar signifies the mean factor for a population), d is the particle diameter (m), $F(d)d(d)$ is the number of particles per unit volume in the size range $d \pm ½$

$d(d)$, and λ denotes wavelength (nm). Using the experimental algal absorption coefficients and size distribution data as described above, $\overline{Q}_a(\lambda)$ can therefore be calculated for natural algal assemblages. Employing the anomalous diffraction approximation [Van de Hulst 1957],

$$Q_a(\lambda)=1+\frac{2e^{-\rho'}}{\rho'}+2\frac{e^{-\rho'}-1}{\rho'^2} \qquad (3.2)$$

dimensionless absorption efficiency factors can be expressed in terms of the the absorption of the cellular material a_{cm} (m^{-1}) and the diameter of the particle d (m^{-1}) through the dimensionless optical thickness $\rho' = a_{cm}d$ and $a_{cm} = 4\pi n'/\lambda$. Similarly, the dimensionless package effect parameter Q_a^*, as given by [Morel & Bricaud 1981]:

$$Q_a^*=\frac{3}{2}\frac{Q_a}{a_{cm}d} \qquad (3.3)$$

can be calculated. The Chl a-specific absorption of phytoplankton a_ϕ^* (m^2 mg^{-1}) and the unpackaged Chl a-specific absorption $a_{\phi u}^*$ (m^2 mg^{-1}) can therefore be expressed as:

$$a_\phi^*=\frac{a_{cm}}{c_i}Q_a^* \qquad (3.4) \qquad\qquad a_{\phi u}^*=\frac{a_{cm}}{c_i} \qquad (3.5)$$

where c_i is the intracellular Chl a concentration (kg m^{-3}). Equations (3.1) to (3.5) can thus be used in conjunction with measurements of absorption, particle size distributions and HPLC intracellular pigment concentrations to derive absorption efficiency factors and causal variables for algal populations. Detailed methods regarding these derivations are presented in Chapter 2.2.

Table 3.1 Notation and pigment abbreviations and chemotaxonomic use.

a	absorption coefficient [m^{-1}]	
a_{cm}	absorption of cellular material [m^{-1}]	
a_ϕ	phytoplankton absorption coefficient [m^{-1}]	
a_d	detrital absorption coefficient [m^{-1}]	
a^*_ϕ	chlorophyll *a* specific phytoplankton absorption [m^2 mg Chl a^{-1}]	
$a^*_{\phi u}$	unpackaged chlorophyll *a* specific phytoplankton absorption [m^2 mg Chl a^{-1}]	
c_t	intracellular chlorophyll *a* concentration [kg m^{-3}]	
Chl *a*	total algal chlorophyll *a* concentration [mg m^{-3}]	
d	diameter [µm]	
d_{eff}	effective diameter [µm]	
$F(d)$	number of particles per unit volume [m^{-3}]	
λ	in vacuo wavelength [nm]	
Q_a	absorption efficiency factor [dimensionless]	
Q^*_a	package effect parameter [dimensionless]	
ρ'	optical thickness [dimensionless]	
	Pigment Abbreviations	Chemotaxonomic Identifier[1]
Allo	alloxanthin	Cryptophytes
But-fuco	19'-butanoyloxyfucoxanthin	some Haptophytes, Pelagophytes
Chl *a*	chlorophyll *a*	Ubiquitous
Chl *b*	chlorophyll *b*	Chlorophytes, Prasinophytes, Euglenophytes
Chl *c*	chlorophyll *c*	-
Diadino	Diadinoxanthin	-
Fuco	Fucoxanthin	Diatoms
Hex-fuco	19'-hexanoyloxyfucoxanthin	Prymnesiophytes
Perid	Peridinin	Dinoflagellates
Viola	Violaxanthin	Chlorophytes, Eustigmatophytes
Tpigs	ratio of all pigments (excluding chlorophyll *a*) to chlorophyll *a*	

1. Jeffrey et al. 1997.

3.3 Field Methods and Analysis

Bio-optical measurements were made on surface samples from diverse water types, ranging from the near oligotrophic to high biomass algal blooms dominated by a variety of algal species. Sampling was conducted from 1999 to 2003 in the southern Benguela from a variety of platforms (see Table 2.1 and Appendix II). Principal measurements

consisted of particulate absorption, particle size distributions and intra-cellular pigments from 34 samples. Identification of numerically dominant algal species and groups were made using a combination of microscopic analysis of fresh and preserved samples and chemotaxonomic information from HPLC pigment analyses. Particulate data were separated into algal and detrital components and inverse anomalous diffraction models [Bricaud & Morel 1986] were used to derive algal refractive index and cellular material information. Detailed methods for all measurements are presented in Chapter 2.

3.3.1 Particulate Absorption

Particulate and detrital absorption data were measured with the quantitative filter pad technique [Yentsch 1962, Roesler 1998, Kishino *et al.* 1985] using a Shimadzu UV-2501 spectrophotometer equipped with an ISR-2200 internal integrating sphere. Phytoplankton absorption $a_\phi(\lambda)$ data were then obtained by subtraction of detrital absorption $a_d(\lambda)$ from total particulate absorption $a_p(\lambda)$.

3.3.2 Particle Size Distributions (PSD)

Particle size measurements were made using a 128 channel Coulter Multisizer II with either a 50 μm or 140 μm aperture in manometer mode, using freshly prepared 0.2 μm filtered seawater as both blank and electrolyte. Numerical techniques [Chapter 2] were employed to fractionate measured size distributions into algal and non-algal components, and extend both lower and upper ranges of measured size distributions to match absorption measurements. A discussion of the potential errors introduced through this approach is presented in Appendix I.

Polydispersed algal particle size distributions are described by the effective diameter d_{eff} [Hansen & Travis 1974, Ahn *et al.* 1992] as given by:

$$d_{eff} = \frac{\int_{1}^{100} \frac{\pi}{4} d^3 F(d) d(d)}{\int_{1}^{100} \frac{\pi}{4} d^2 F(d) d(d)} \qquad (3.6)$$

3.3.3 Pigments

Pigments were analysed using HPLC. Seawater was filtered through 25 mm GF/F filters and filters stored frozen in liquid nitrogen until analysis [Barlow *et al.* 1997, Chapter 2].

Intracellular Chl *a* concentrations c_i (kg m^{-3}) were calculated from HPLC and algal particle size data using the following expression [Bricaud & Morel 1986]:

$$c_i = \text{Chl } a \left[\frac{\pi}{6} \int_1^{100} F(d) d^3 d(d) \right]^{-1} \tag{3.7}$$

3.3.4 Statistics

Statistical analyses were carried out to assess the covariance between all pigment and size related data (Table 3.2), and the spectral coefficients of determination between spectral algal absorption data and pigment and size related data (Figure 3.2). All statistical analyses were carried out using a bootstrapping technique, as much of the data were not normally distributed, as determined by the Lilliefors test [Conover 1980]. A bootstrap analysis using 1000 resampled replicates was made using Matlab R12 [The Mathworks], using a Fisher transform [Fisher 1921] on correlation data from bootstrap replicates to ensure a normal distribution. Coefficients of determination were determined using median replicate values, and significance levels were determined at a 95 % confidence level using the 2.5th and 97.5th percentile of the replicated correlation data, i.e. $p<0.05$. Significance levels vary amongst the accessory pigments analysed due to the different number of samples analysed: cases with non-detectable pigment concentrations were excluded from analysis. Correlation analyses on absorption data were carried out on all wavelengths from 400 nm to 700 nm at an interval of 1 nm.

3.4 Results of Field Data

Example measured and unpackaged Chl *a*-specific absorption spectra, fourth derivative spectra [Butler & Hopkins 1970], and package effect parameter spectra are presented in Figure 3.1A to 3.1D. The four assemblages shown are an offshore low biomass (Chl a = 0.5 mg m^{-3}) sample dominated by chrysophytes, chlorophytes and cyanobacteria (*flagellate*), a high biomass (Chl a= 120 mg m^{-3}) bloom dominated by the dinoflagellates *Alexandrium catenella* and *Ceratium furca* (*dinoflagellate*) a high biomass (Chl a = 195 mg m^{-3}) bloom dominated by the ciliate *Mesodinium rubrum* (*cryptophyte*), and a monospecific bloom (Chl a= 13.1 mg m^{-3}) of *Aureococcus anophagefferens* (*pelagophyte*). The examples are chosen to show the maximum range of variability observed in the phytoplankton absorption data, from a range of assemblages likely to encompass the major suites of accessory pigmentation found in upwelling systems [Hutchings *et al.* 1994]. The *pelagophyte* assemblage has similar accessory pigment composition to the majority of diatom species [Jeffrey 1997], regarded as a numerically dominant class in upwelling systems, and serves to demonstrate the expected pigment related characteristics of the diatom group. The effects of both varying size and accessory pigmentation can be observed in Fig 3.1A; specifically the higher Soret and red peaks of the smaller size pelagophyte- and flagellate-dominated samples, and the effects of phycoerythrin absorption at ~550 nm [Sciandra *et al.* 2000] for the cryptophyte-dominated sample. Note that the sample in question was dominated by the ciliate *Mesodinium rubrum*, and the cryptophyte pigments observed are thus most likely to be associated with endosymbiotic chloroplasts [Gustafson 2000, Kyewelyanga 2002].

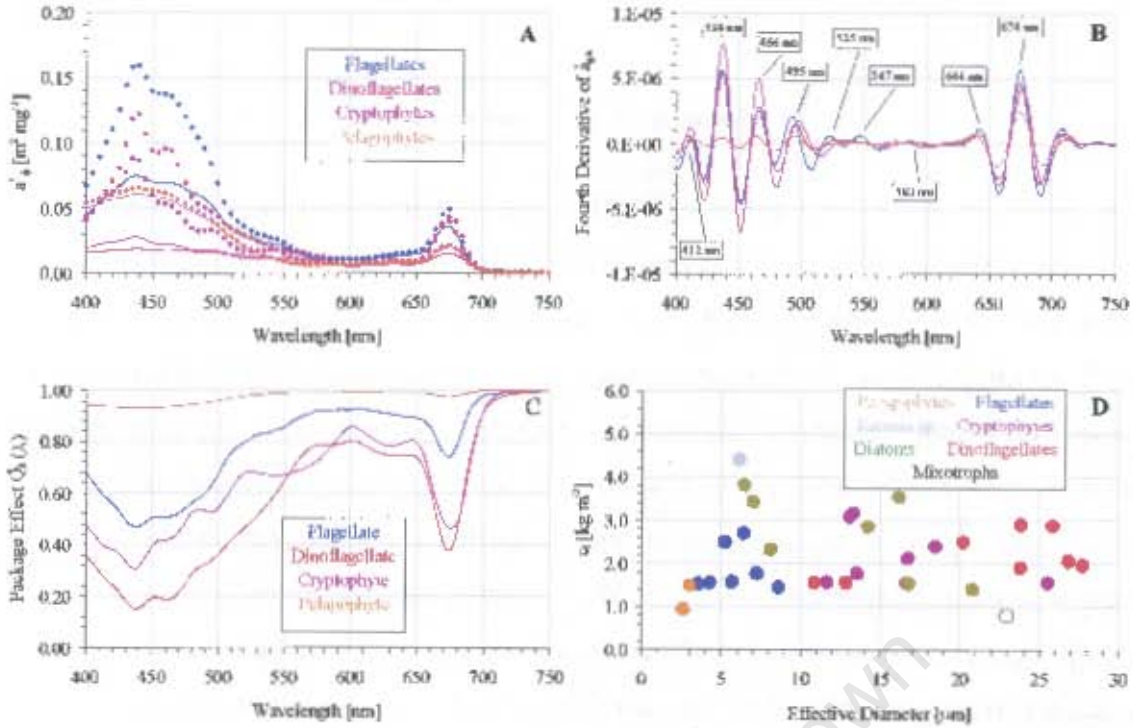

Figure 3.1 A) Packaged (a^*_ϕ – lines) and unpackaged ($a^*_{\phi u}$ – dots) Chl *a*-specific phytoplankton absorption for four example assemblages. B) Example fourth derivative $a^*_{\phi u}(\lambda)$ spectra for the same samples. C) Example package effect parameter $Q^*_a(\lambda)$. D) Effective diameter d_{eff} vs. intracellular Chl *a* concentration c_i identified by dominant algal group.

Table 3.2 Coefficients of determination (r^2) values for all size and pigment related data. Only relationships significant at the 95 % confidence level are shown.

	d_{eff}	c_i	Tpigs	Chl *c*	Perid	But-fuc	Fuco	Hex-fuco	Viola	Diadino	Allo	Chl *b*
d_{eff}					0.39	0.49		0.23				0.15
c_i												
Tpigs				0.26	0.25	0.17		0.41		0.56	0.51	
Chl *c*			0.26			0.21		0.31			0.11	
Perid	0.39		0.25			0.34	0.08		0.09	0.32	0.11	0.14
But-fuc	0.49		0.17	0.21	0.34			0.33		0.11	0.15	
Fuco					0.08						0.11	
Hex-fuco	0.23		0.41	0.31		0.33					0.09	0.12
Viola					0.09							0.88
Diadino			0.56		0.32	0.11		0.09			0.50	
Allo			0.51	0.11	0.11	0.15	0.11	0.09		0.50		0.05
Chl *b*	0.15				0.14			0.12	0.88		0.05	

The fourth derivative spectra (Fig 3.1B) [Butler & Hopkins 1970] show that pigment-related absorption variability is greatest in approximately nine absorption bands corresponding to the spectra of Chl *a* and the major accessory pigments [Millie *et al.* 1995, Kirkpatrick *et al.* 2000, Kyewelyanga 2002]. The association of fourth derivative peaks with specific accessory pigments is somewhat imprecise, due to the spectral shifts between *in vivo* and *in vitro* pigment absorption peaks resulting from denaturisation in the extraction process, and the spectral similarities between most of the major carotenoids, e.g. fucoxanthin, peridinin, alloxanthin, diadinoxanthin [Bidigare *et al.* 1990]. Nevertheless, the peaks at 438 nm and 674 nm are likely to be associated with Chl *a*, those between 466 nm and 525 nm with chlorophyll c and the major carotenoids such as fucoxanthin (and derivatives), peridinin, diadinoxanthin and alloxanthin, the 547 nm peak with phycoerythrin, and the 644 nm peak with chlorophyll b [Bidigare *et al.* 1990, Johnsen *et al.* 1994, 1994a, Millie *et al.* 1995].

Calculated package effect parameter for the same examples (Fig 3.1C) are in the most part larger, ($Q_a^*(\lambda)$ closer to zero) than those reported for algal cultures using cell disruption techniques [Osborne & Geider 1989, Sosik & Mitchell 1991, Johnsen *et al.* 1997] but are comparable in magnitude to those calculated for natural assemblages [Bricaud *et al.* 1995, Bricaud *et al.* 2004, Lohrenz *et al.* 2003]. The very high packaging of the large celled dinoflagellate dominated assemblage (effective diameter = 28 μm), compared to that of the small pelagophyte (effective diameter = 2.5 μm) *A. anophagefferens*, is clearly evident at 438 nm.

The relationship between the effective diameter d_{eff} and the intracellular Chl *a* concentration c_i, two of the variables causal to both packaging and phytoplankton absorption, are shown in Figure 3.1D for all assemblages analysed. Previous studies have shown quantifiable inverse relationships between c_i and cell volume [Hitchcock 1982, Moal *et al.* 1987, Montagnes *et al.* 1994], in addition to rough inverse relationships between c_i and d_{eff} [Taguchi 1976, Malone 1980, Bricaud *et al.* 1988]. However, the c_i vs. d_{eff} relationships from these studies have typically shown a great deal of scatter, and there is ample evidence indicating that environmentally induced variability in c_i can be comparable in magnitude to interspecific variability. Photoadaptive state, nutrient limitation, growth phase and temperature [Messer & Ben-Shaul 1972, Thinh 1983, Rosen & Lowe 1984, Osborne & Raven 1986, Sosik & Mitchell 1991, Stramski *et al.* 2002] have all been shown to cause large variations in intracellular pigment concentrations. It is not unreasonable to assume that the assemblages considered in this study are high light adapted, given that they are all surface samples taken in daylight. The c_i values shown in Figure 3.1D (0.7 to 4.2 kg m^{-3}) compare well with published data for high light grown cultures of the diatom *Thalassiosira* spp.(1 to 3 kg m^{-3}, Stramski *et al.* 2002) and a range of species presented in Bricaud *et al.* 1988 (0.3 to 6 kg m^{-3}). Given the lack of any statistically significant relationship between effective diameter and intracellular Chl *a* concentration (Table 3.2), it would appear that environmental influences are greater determinants of c_i than taxonomic groupings for the natural surface assemblages considered here.

Figure 3.2 and Table 3.2 shows the results of the statistical analyses between all size, pigment and absorption data. Figure 3.2A indicates that mean assemblage size is the major influence on packaged algal absorption, explaining up to 45 % of absorption variability, and most strongly correlated in the Soret and red peak absorption regions. Intracellular Chl *a* concentration c_i is only significantly correlated in the blue and red spectral regions, and can explain up to ~ 16 % of absorption variability at blue wavelengths.

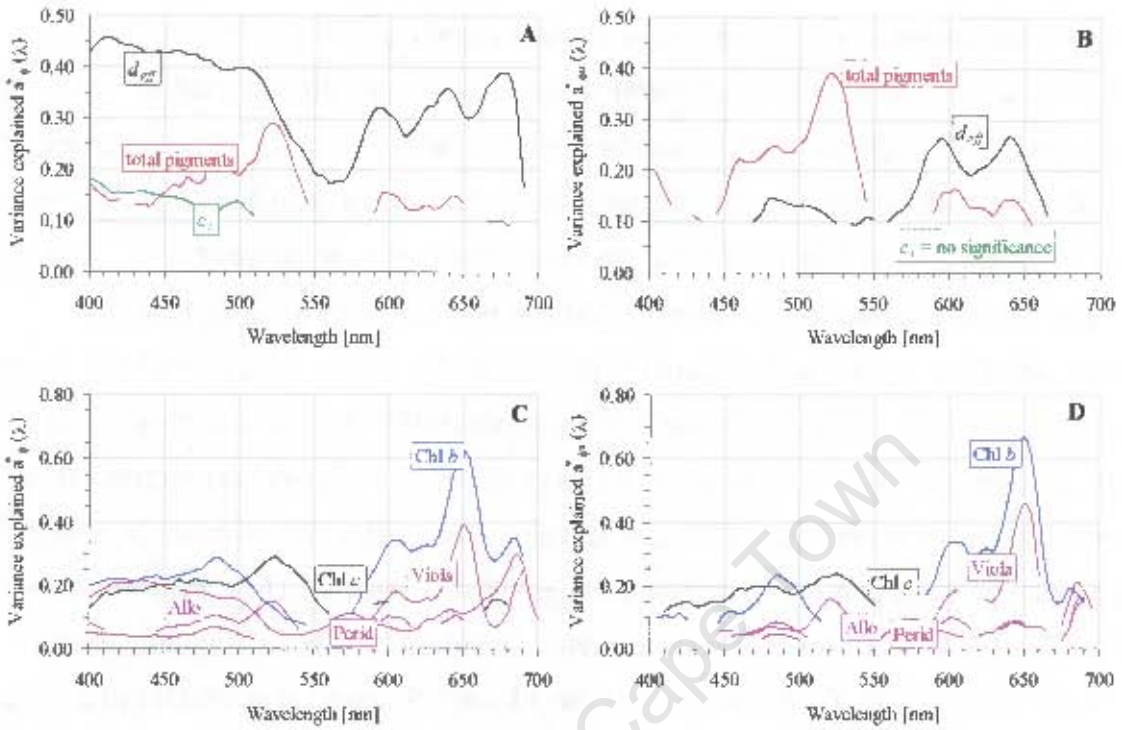

Figure 3.2. Results of the spectral bootstrap analyses for measured Chl *a*-specific absorption, and unpackaged Chl *a*-specific absorption. Spectra of significant ($p<0.05$) coefficients of determination (r^2) are presented for: A) d_{eff}, c_i and total accessory pigments (relative to Chl *a*) vs. a^*_ϕ , B) d_{eff}, c_i and total accessory pigments vs. $a^*_{\phi u}$ (unpackaged absorption), C) Accessory pigments vs. a^*_ϕ , D) Accessory pigments vs. $a^*_{\phi u}$ (unpackaged absorption). Note the effective decoupling of size and pigment effects associated with the unpackaging of absorption. Discontinuous areas in the spectra are indicative of wavelengths where no significant correlation occurred.

The relatively minor apparent effects of c_i on absorption are consistent with the lack of interspecific c_i variability previously discussed. The effects of total cellular pigmentation, i.e. all accessory chlorophylls and carotenoids normalised to Chl *a*, can be seen as most pronounced between 500 nm and 540 nm, explaining ~30% of absorption variability. This result is consistent with published absorption discriminant [Johnsen *et al.* 1994] and decomposition [Hoepffner & Sathyendranath 1993, Stuart *et al.* 1998] techniques, which successfully used a 530-535 nm wavelength to account for the spectral influence of the major light harvesting carotenoids.

Analyses of the unpackaged Chl *a*-specific absorption show that the process of unpackaging partially decouples the effects of assemblage size, intracellular Chl *a* concentration and accessory pigmentation (Fig. 3.2B and D). There is no significant correlation between unpackaged absorption and d_{eff} in the blue region, and no significant correlation with c_i at any wavelength. The correlations between unpackaged absorption and size remaining in the red region (~25%) are less than for packaged absorption (~40%), but still significant at 95 % confidence limits, and indicative of incomplete decoupling. Problems with direct and theoretical package effect determinations at red wavelengths have been observed previously [Geider & Osborne 1987, Osborne & Geider 1989], and are subject to a number of potential error sources, both random and systematic. These include instrumental errors affecting measurement precision, scattering errors in absorption measurements, residual absorption inappropriately removed by the 750 nm null point correction, and inappropriate calculation of detrital particle size distributions. In addition, the anomalous diffraction approximation's (ADA) assumption of homogenous sphericity is very much a simplification with regard to algal morphology. There are many possible departures from uniformity, which the ADA cannot account for, known to affect absorption packaging. These include variability in: number, shape and position of chloroplasts per cell, thylakoid stacking, intracellular biochemistry, and areal chlorophyll thylakoid density: [Rosen & Lowe 1984, Geider & Osborne 1987, Berner *et al.* 1989, Osborne & Geider 1989]. Nevertheless, the removal of size effects at blue wavelengths by unpackaging absorption suggests that an absorption formulation making explicit use of the package effect can account for mean assemblage size. The enhanced

correlation between total pigments and absorption resulting from unpackaging absorption (comparison of Fig. 3.1A and 3.1B) also suggests that techniques aimed at discriminating accessory pigment related changes in absorption should have greater success when size and intracellular pigment concentration effects have been removed by unpackaging absorption.

The apparent explained variability in absorption by accessory pigments is depicted in Figures 3.2C and 3.2D. It appears that Chl *b* can explain 60 % to 70 % of absorption variability at ~ 650 nm: the location of a unique Chl *b* absorption band successfully used by previous researchers for chemotaxonomic discrimination of Chl *b* containing algal groups [Hoepffner & Sathyendranath 1993, Johnsen *et al.* 1994]. Whilst the explained variability associated with Chl *b* at 650 nm would thus appear to be of causal significance, the apparent correlation of the carotenoid Viola at similar wavelengths (at which it does not absorb) is unlikely to be causal: it is more likely to result from the high Viola: Chl *b* covariance (r^2=0.88, n=34, $p<0.05$, Table 3.2). This high correlation also indicates that the majority of Chl *b* containing algae in this study are Chlorophytes and Prasinophytes as opposed to Euglenophytes, which do not contain Viola [Jeffrey *et al.* 1997]

Similar considerations indicate that the other accessory pigments showing moderately significant correlations in Figure 3.2C and 3.2D cannot explain absorption variability in a causal manner. Peaks in r^2 values for Perid and Chl *c* are not consistent with the location of absorption bands in these pigments [Bidigare *et al.* 1990, Johnsen *et al.* 1994, 1997]. The r^2 values of Allo, explaining ~ 15 % of absorption variability at 520 nm, are similarly not located either in the vicinity of the ~ 495 nm Allo absorption band or the ~545 nm phycoerythrin absorption band absorption band [Prezelin & Boczar 1986, Hewes *et al.* 1998], but are located at wavelengths previously used for carotenoid determinations [Johnsen *et al.* 1994, Hoepffner & Sathyendranath 1993]. The Allo related r^2 values can therefore only be interpreted equivocally. The effects of unpackaging absorption results in an ~10% increase in the r^2 values for causally significant pigment absorption relationships.

In conclusion, it appears expressing absorption through a package effect formulation allows significant decoupling of the three causal absorption variables: d_{eff}, c_i and accessory pigment composition. It also appears that without recourse to the sophisticated discriminant techniques [Johnsen *et al.* 1994, Kirkpatrick *et al.* 2000] unavailable for application to inverse absorption models, it will only be possible to discern the absorption effects of algal groups containing uniquely absorbing pigments, such as chlorophyll *b*. Given the unique location of phycoerythrin absorption bands between ~ 540 nm and 600 nm [Prezelin & Boczar 1986], there would be some hope of discriminating phycobiliproteins from absorption. However, phycobiliproteins cannot be determined using the HPLC pigment techniques used in this study; alternative means of phycoerythrin determination from unpackaged absorption [Sciandra *et al.* 2000] cannot result in measurements independent to absorption. Without such independent data, phycobiliprotein concentrations are not considered in a quantitative manner in this study.

3.5 Inverse Model Development

Having established that assemblage size and accessory pigmentation have significant effects upon the absorption coefficients of natural algal assemblages, the study seeks to establish whether it is possible to quantitatively calculate these causal variables through inverse absorption models. These models seeks to calculate Chl *a* concentration, effective algal diameter, and appropriate accessory pigment concentrations by simulating measured algal absorption with a reconstruction based on a package effect based formulation. Algal absorption spectra are approximated using basis vectors of unpackaged Chl *a*-specific algal absorption spectra $a^*_{\phi u}(\lambda)$, an assumed intracellular pigment concentration c_i, and a package effect parameter $Q^*_a(\lambda)$ calculated explicitly from an algal diameter value. The four algal groups depicted in Figure 3.1A are used to compose the $a^*_{\phi u}(\lambda)$ admixture, making the assumption that the majority of algal absorption spectrum can be approximated by an appropriate mixture of these four diverse algal groups. Two models are assessed: a single spectral vector model returning Chl *a* concentrations and effective diameter (1V model) and a four spectral vector model (4V model) that additionally returns accessory pigment concentrations. Revisiting Equation 3.4, phytoplankton absorption can thus be expressed as a function of the Chl *a* concentration and packaged absorption such that:

$$a_\phi(\lambda) = Chl\, \bar{a}^*_{\phi u}(\lambda) Q^*_a(\lambda) \tag{3.8}$$

where $\bar{a}^*_{\phi u}$ represents either a single predetermined mean $a^*_{\phi u}$ vector (1V model) or the mean admixture of four unpackaged Chl *a*-specific algal absorption spectra (4V model) as given by:

$$\bar{a}^*_{\phi u}(\lambda) = P_1 a^*_{\phi u1}(\lambda) + P_2 a^*_{\phi u2}(\lambda) + P_3 a^*_{\phi u3}(\lambda) + P_4 a^*_{\phi u4}(\lambda) \tag{3.9}$$

where the unknowns P_n represent the normalised scaling parameter ($0 \leq P_n \leq 1$) for a single vector in the admixture such that:

$$\sum_{n=1 \text{ to } 4} P_n = 1 \tag{3.10}$$

and $Q_a^*(\lambda)$ represents the package effect determined from an explicit effective diameter value d_{eff} (µm), the average $a_{\phi a}^*(\lambda)$ vector (m^2 mg^{-1}) and a predetermined value of c_i (kg m^{-3}):

$$Q_a^*(\lambda) - \frac{3}{2} \frac{Q_a(\lambda)}{a_{\phi a}^*(\lambda)\, c_i\, d_{eff}} \tag{3.11}$$

where the absorption efficiency factor $Q_a(\lambda)$ is a function of the dimensionless optical thickness ρ' ($= \overline{a}_{\phi a}^*\, c_i\, d_{eff}$) as given by Equation 3.2.

The inverse model thus accepts an input of a measured absorption spectrum, and seeks to simulate this absorption by iteration of the independent unknowns described below, which are the final model output. Equations 3.8, 3.9 and 3.10 are thus solved for iteratively using a non-linear regression technique (Nelder-Mead Simplex, Matlab R12 The Mathworks) [Nelder & Mead 1965], where the number of unknowns (model outputs) is either two for the 1V model (Chl *a* and d_{eff}) or six for the 4V model (Chl *a*, d_{eff} and $P_{1\ to\ 4}$, representing the relative concentrations of the algal spectral basis vectors). Relative accessory pigment concentrations, to be used as chemotaxonomic markers, are calculated through a mean pigment suite admixture $\overline{ps}$, where:

$$\overline{ps} = P_1 ps_1 + P_2 ps_2 + P_3 ps_3 + P_4 ps_4 \tag{3.12}$$

and ps_n represents a vector of accessory pigment concentrations associated with each algal group; the values of which can be seen in Table 3.2.

The validity of using a single effective diameter value in representing complex polydispersed algal size distributions has already been demonstrated in Chapter 2. Unpackaged Chl *a*-specific absorption spectra $a^*_{pu}(\lambda)$ were all normalised to a value of 0.027 m^2 mg^{-1} at 674 nm [Johnsen *et al.* 1994a], selected as the theoretical maximum unpackaged absorption at this wavelength – the spectra can be seen in Figure 3.3A. This normalisation ensures that the inverse model selects algal group ratios only on spectral pigment related differences in unpackaged absorption rather than c_i related variations in absorption magnitude. Accessory pigment concentrations calculated using Equation 3.12 were scaled using these $a^*_{pu}(675)$ normalisation factors to ensure consistent relative accessory pigment concentrations between algal groups.

The basis vector used for the 1V model was generated using the mean of the *pelagophyte*, *flagellate* and *dinoflagellate* vectors. It should be noted that the four basis vectors are not explicitly used in the models as an attempt to identify these specific algal groups: the basis vectors are chosen rather to represent generic unpackaged absorption by the most common light harvesting chromoprotein suites in upwelling systems [Hutchings *et al.* 1994]. These are chlorophyll *c*-fucoxanthin-diadinoxanthin (*pelagophyte*, representing both diatoms and pelagophytes), chlorophyll *c*-chlorophyll *b*-fucoxanthin derivatives (*flagellate*), chlorophyll *c*–peridinin-diadinoxanthin (*dinoflagellate*), and chlorophyll *c*–alloxanthin (*cryptophyte*, or more probably algal groups containing endosymbiont cryptophyte organelles). The representation of diatoms, so important to upwelling systems, with a spectral basis vector derived from a pelagophyte assemblage can be justified on the basis of their very similar chromoprotein characteristics from a spectral perspective [Bidigare *et al.* 1989, Jeffrey *et al.* 1997]. An intracellular pigment concentration $c_i = 2.75$ kg m^{-3}, representing a median value of the c_i data displayed in Figure 3.1d, was used for all model calculations. All statistics used to assess model performance were calculated using the bootstrapping techniques described in Section 3.3, with the exception of standard error of prediction estimates (SE), which were calculated using parametric methods. The model was tested on an independent data set, in that the samples used to derive the model basis vectors were removed before analysis.

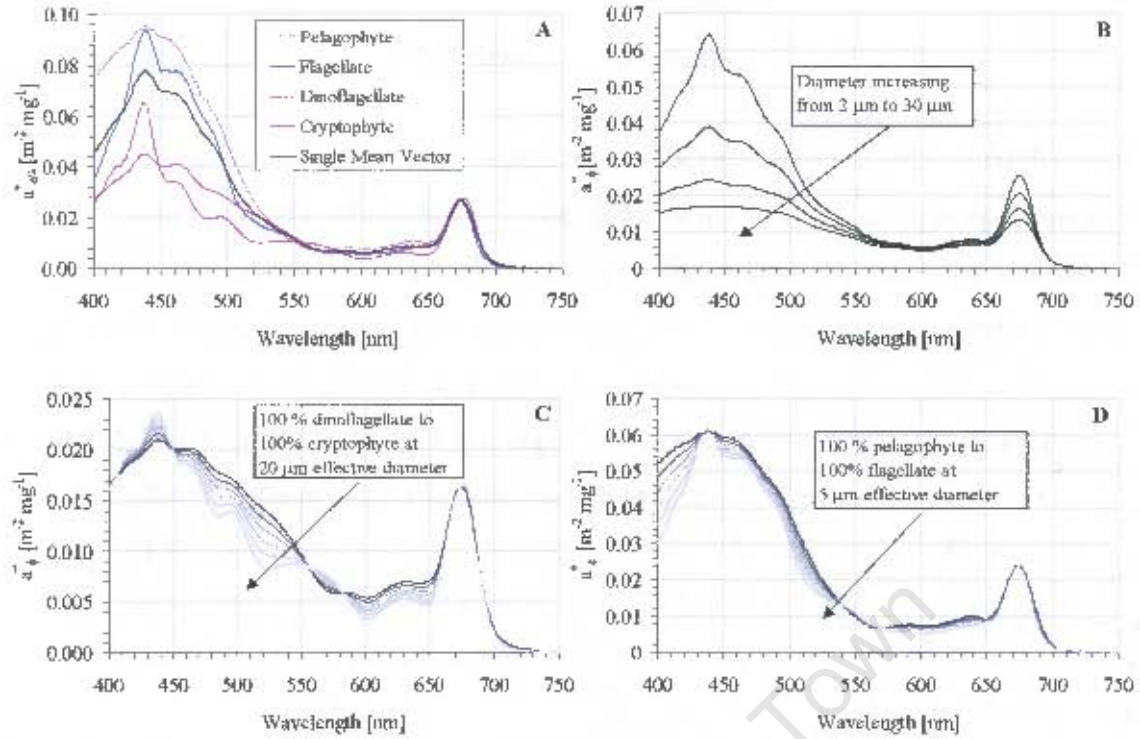

Figure 3.3. A) Unpackaged Chl *a*-specific absorption basis vectors used by the 4V and 1V models, B) Example spectra from the 1V model demonstrating the effects of changing size upon phytoplankton absorption, C) Example spectra from the 4V model demonstrating the effects of changing assemblage type from dinoflagellate- to cryptophyte-dominated at an effective diameter of 20 µm, and D) Example spectra from the 4V model demonstrating the effects of changing assemblage type from pelagophyte- to flagellate-dominated at an effective diameter of 5 µm.

Table 3.2 Accessory pigment concentrations relative to Chl *a* for the four unpackaged absorption basis vectors used in the 4V model, from HPLC analyses of the respective assemblages

	pelagophyte	flagellate	dinoflagellate	cryptophyte
Chl *c*	0.072	0.286	0.225	0.125
Perid	-	0.051	1.036	0.028
But-fuco	0.219	0.120	-	-
Fuco	0.365	0.086	0.107	0.048
Hex-fuco	0.014	0.028	0.246	-
Viola	-	0.019	-	-
Diadino	0.149	0.091	0.110	0.010
Allo	0.015	0.013	0.042	0.180
Chl *b*	0.025	0.184	-	-
Tpigs	0.860	0.879	1.767	0.390

Figures 3.3B to 3.3D demonstrate the forward response of the 1V and 4V models to changes in assemblage size and structure. Figure 3.3B shows the change in shape of the Chl *a*-specific phytoplankton absorption spectra, utilising the 1V model with effective diameter ranging from 2 μm to 30 μm. Spectra associated with larger mean cell sizes display flattened and lowered absorption spectra, as previously shown from theoretical studies [Duysens 1956, Morel & Bricaud 1981] and field data [Bricaud *et al.* 1995, Ciotti *et al.* 2002]. Figures 3.3C and 3.3D show the effect of changing assemblage type by manipulating the basis vector admixture composition. The spectral effects of assemblage change are most noticeable in the 450 nm – 550 nm regions, primarily due to differing relative carotenoid concentrations, and in the 550 nm region due to the effects of phycoerythrin absorption.

3.6 Inverse Model Results

3.6.1 Chl *a* and Effective Diameter

Both the 1V and 4V absorption models were able to predict the Chl *a* concentration and effective diameter of a wide variety of algal assemblages sufficiently well for use in a predictive operational capacity. In the majority of cases both models were able to accurately reconstruct measured algal spectral absorption, with the exception of accessory pigment related features not available to the 1V model.

Figure 3.4 shows reconstructed spectra of both models for two example assemblages: a high biomass bloom dominated by the small dinoflagellate *Gyrodinium zeta* (Fig 3.4A), and an intermediate biomass assemblage dominated by a variety of diatom species (Fig 3.4B). The example assemblages are specifically chosen for their dissimilarity to the assemblages used for derivation of the basis vectors used in the inverse models. Whilst both the 1V and 4V models appear capable of reproducing the gross features of the absorption spectra, the 4V model is better able to reproduce accessory pigment related absorption fine structure due to the choice of spectral basis vectors available to it.

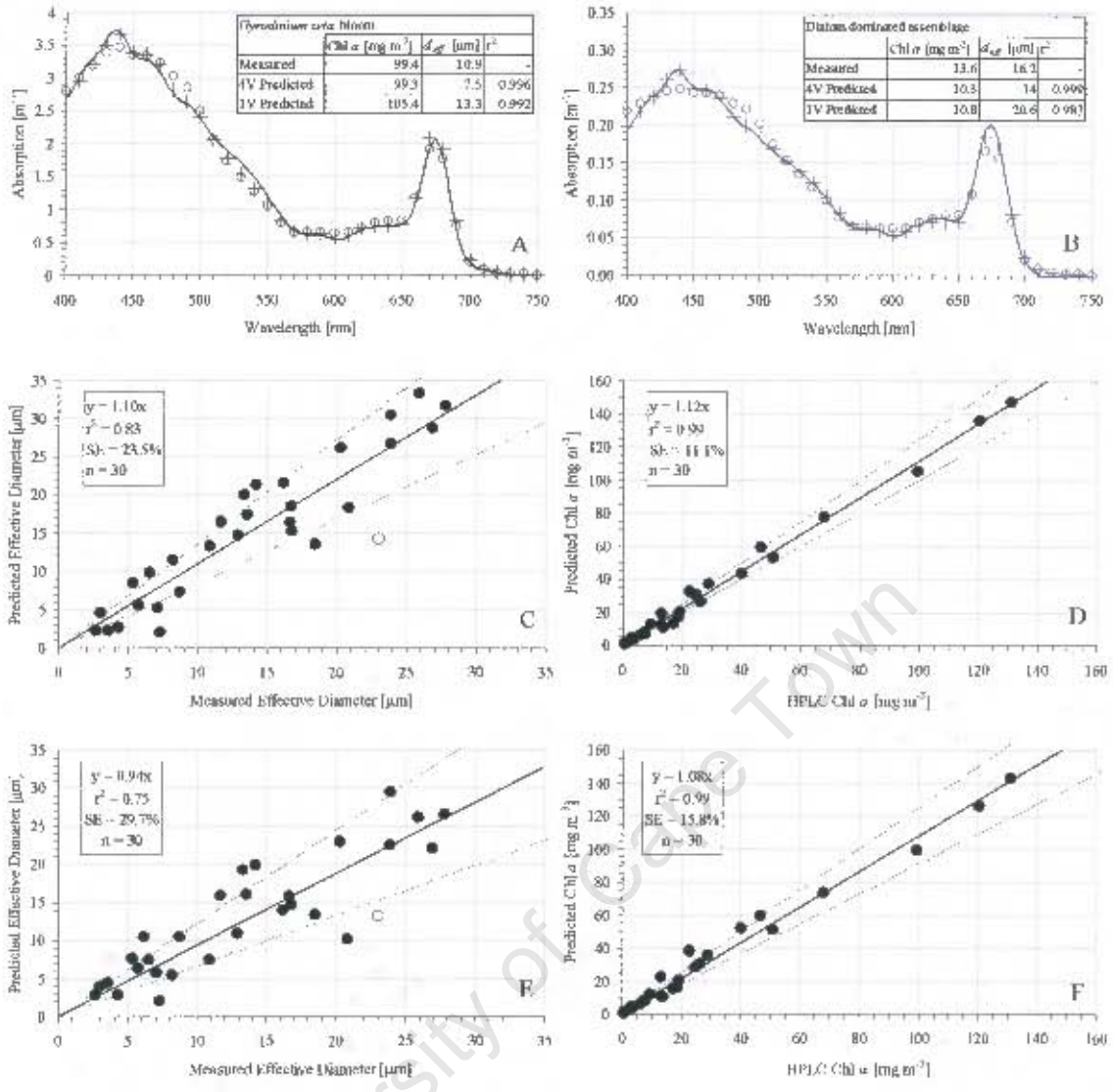

Figure 3.4 Performance of the 1V (o) and 4V (+) inverse absorption models with regard to: A) Example matched absorption of a bloom of the small dinoflagellate *Gyrodinium zeta*, B) Example matched absorption of a mixed diatom population, C) Predicted effective algal diameter d_{eff} using the 1V model, D) Predicted Chl *a* concentrations using the 1V model, E) Predicted effective algal diameter d_{eff} using the 4V model, and F) Predicted Chl *a* concentrations using the 4V model. The solid line in C) to F) represents the linear best fit, while dashed lines represent the percentage standard error (SE) of the prediction, which were not calculated using bootstrapping techniques. The open circles in C) and F) represent a mixotroph dominated assemblage - the effects of lower c_i associated with mixotrophy can be seen in the poor prediction of d_{eff} for this assemblage. Note the higher standard error and data scatter in predicted d_{eff} for the 4V model.

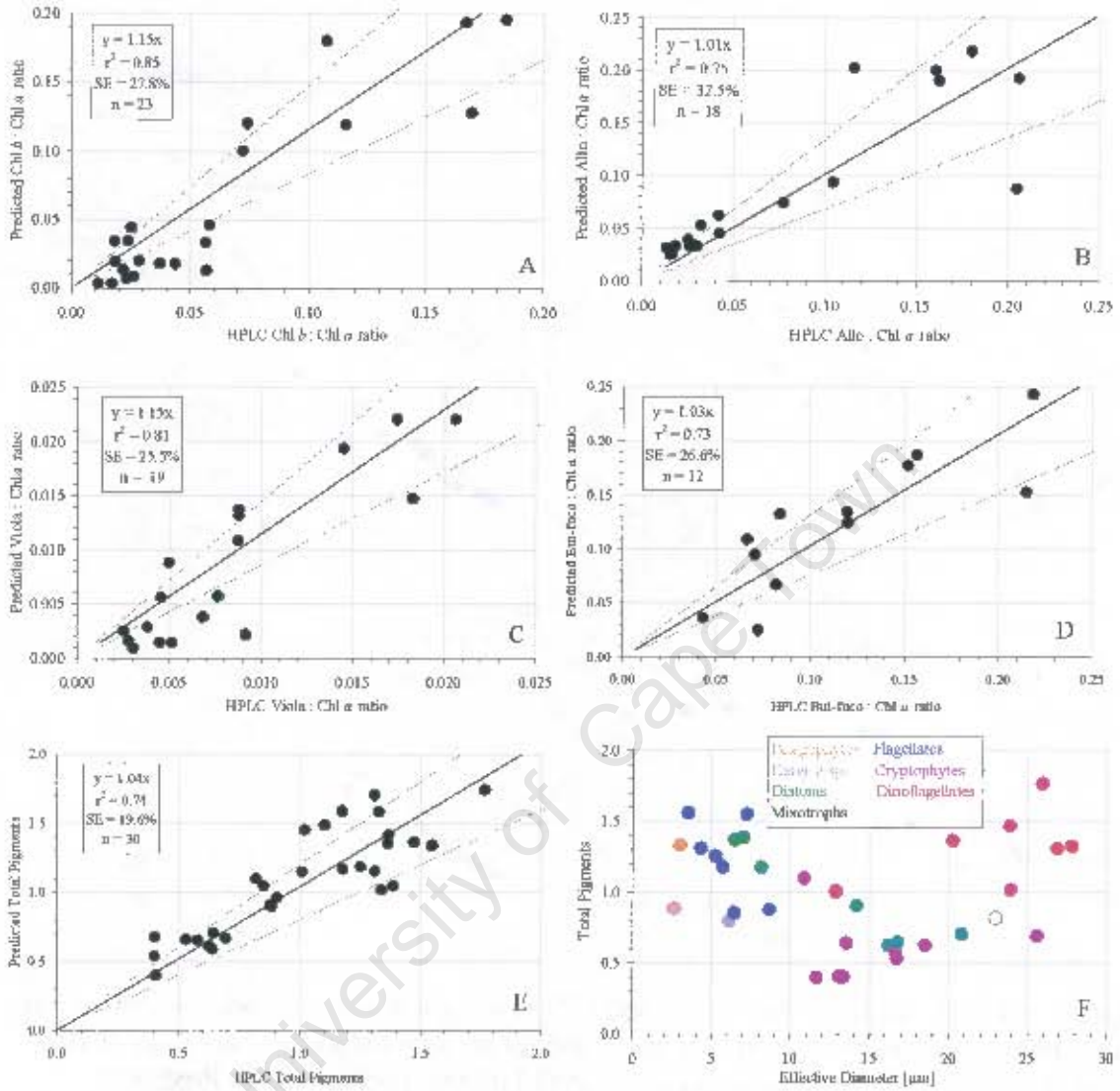

Figure 3.5 Performance of the 4V inverse absorption models with regard to A) Predicted Chl *b*: Chl *a* ratio, B) Predicted Allo : Chl *a* ratio, C) Predicted Viola: Chl *a* ratio, D) Predicted But-fuco : Chl *a* ratio, E) Predicted total pigment concentration (*Tpigs*), and F) effective diameter d_{eff} vs. total pigments *Tpigs*. The solid line represents the linear best fit, while dashed lines represent the percentage standard error (SE) of the prediction. The very similar performance with regard to Chl *b* and Viola prediction is indicative of the high covariance between these pigments as they occur in this dataset, as discussed previously. No other accessory pigments were predicted at significance levels of $P<0.05$. Note also the changing sample size with regard to the different accessory pigments, due to non detectable pigment concentrations in some samples.

This is also the case when considering the whole data set (n=34), with r^2 values ranging from 0.960 to 0.999 for the 4V model, as compared to r^2 values from 0.933 to 0.999 for the 1V model. The lower r^2 values associated with the 1V model result from the limited spectral ability to reconstruct absorption spectra from assemblages associated with different accessory pigments to those used in the derivation of it's basis vector e.g. cryptophyte dominated assemblages. Despite the reduced capability of the 1V model to reproduce the finer features of measured absorption spectra, the model demonstrates the ability to predict Chl *a* concentrations (Fig 3.4D) and effective diameter (Fig 3.4C) with some success. Returned Chl *a* values are highly correlated with measured values (r^2=0.99) and are predicted with a standard error of 11 % through a range of 0.5 to 130 mg m^{-3}. Returned effective diameter values are slightly less well correlated with measured values (r^2=0.83) and are predicted with a standard error of 24 % through a range of 2.5 to 28 μm. In comparison, the 4V model shows a correlation between predicted and measured Chl *a* values of r^2=0.99, with a standard error of 16 % (Fig 3.4F), and a correlation between predicted and measured effective diameter values of r^2=0.75, with a standard error of 30 % (Fig 3.4E).

3.6.2 Accessory Pigments

Figure 3.5 shows the performance of the 4V model as concerns the prediction of relative concentrations of accessory pigments, of use as chemotaxonomic markers. The model was able to predict the relative concentrations of four accessory pigments with some degree of confidence: Chl *b* (Fig. 3.5A), Allo (Fig. 3.5B), Viola (Fig. 3.5C), But-fuco (Fig. 3.5D), in addition to total pigments (Fig. 3.5E). The ability of the model to determine Chl *b* values with a reasonably high degree of accuracy (Fig. 3.5A, r^2=0.85, SE=28 %) is consistent with the statistical analyses discussed in Section 3.4, and is likely to result from the ability of the model to discriminate the unique absorption band at 650 nm associated with Chl *b*. The very similar performance of the model with regard to Viola (Fig. 3.5C, r^2=0.81, SE=26 %) should however be considered an artifact of the particular data set considered here - it is extremely unlikely that Viola as a minor pigment will have any significant effect upon absorption in a causal manner, and Chl *b* and Viola have already been shown to be highly covariant (Table 3.2).

The moderately good predictions of the other two accessory pigments depicted in Figure 3.5 are somewhat more open to conjecture. Allo is a major carotenoid in assemblages dominated by cryptophytes or species containing endosymbiont cryptophyte chloroplasts [Table 3.2, Jeffrey *et al.* 1997], and is therefore likely to have a significant effect upon absorption in such cases (Fig 3.2).

However, the cryptophyte associated assemblages in the test data set are known to consist predominately of endosymbiont containing species, such as *Mesodinium rubrum* and *Dinophysis* spp., and there is a strong probability that there is significant covariance between intracellular concentrations of Allo and unquantified phycoerythrin [Gustafson 2000, Hackett *et al.* 2003], shown to influence absorption strongly at wavelengths where the carotenoids have no significant absorption bands (530 –570 nm). The inverse absorption model may discriminate at least partially on phycoerythrin related absorption features, resulting in a vicarious ability to predict covarying Allo concentrations (Fig 3.5B, r^2=0.75, SE=33 %). Further vicarious discrimination may arise from the fact that Allo concentrations are significantly correlated with total pigment concentrations (Table 3.2), already demonstrated to have significant effects upon absorption (Fig 3.2).

The performance of the 4V model with regard to But-fuco, which may be used as a marker pigment for some haptophyte species and pelagophytes [Jeffrey 1997, Zapata *et al.* 2004], is likely to arise from similar phenomena. Whilst But-fuco can form a significant fraction of the total intracellular pigment complement (e.g. 25 % for the pelagophyte vector accessory pigmentation), it is not spectrally distinct from fucoxanthin and others of its derivatives, and is therefore very unlikely to be directly discriminated by the absorption model. It would thus appear that the apparent ability of the model to determine But-fuco concentrations is based upon discrimination of some covariant variable; Table 3.2 would indicate that the significant correlation between d_{eff} and But-fuco may be responsible. Further evidence for a size covariant influence upon But-fuco predictions arises from the small sized picoplankton algal classes typically associated with the presence of But-fuco, e.g. the genera *Aureococcus*, *Dictateria*, *Imantonia* and

Phaeocystis (as a single cell) [Zapata *et al.* 2004]. The ability of the 4V model to also predict total intracellular accessory pigment concentrations moderately well (Fig 3.5E) is consistent with the earlier findings of the study indicating that total accessory pigmentation exerts a significant influence upon both unpackaged and packaged absorption (Fig 3.2). Whilst there would seem little doubt that the model's ability to predict total pigments is rooted in causality and may therefore be used relatively robustly, there is a need to ascertain whether the total pigment descriptor has any use in HAB detection. Figure 3.5F indicates that there may be some potential in this regard: large dinoflagellates, as the most common problem species in the southern Benguela [Pitcher & Calder 2000], may be distinguished from other large celled organisms, e.g. *Mesodinum rubrum*, on the basis of their increased accessory pigment concentrations. The statistical results presented in Figure 3.2, and the performance of the inverse model, indicate the small likelihood of establishing a predictive capability to distinguish diatoms from dinoflagellates based on their pigment related signatures, i.e. through fucoxanthin vs. peridinin markers. In the southern Benguela, effective HAB detection through bio-optical means requires an ability to distinguish between diatoms and dinoflagellates as the two most common non-harmful and harmful algal groups, respectively. There is a need to establish whether other bio-physical descriptors can be identified that may prove useful in this regard. Further research is needed to establish the operational utility of a total pigment descriptor in HAB detection.

3.6.3 Non-Linear Inversion Considerations

The relative performance of the two models demonstrates the payoff demanded by increasing the number of unknowns to allow the estimation of accessory pigment concentrations. Whilst the 4V model has an enhanced ability to more closely reconstruct measured absorption spectra, with a choice of assemblage type with which to synthesize spectral absorption features, the increased number of unknowns result in slightly less confident Chl *a* and effective diameter predictions. The superior performance of the 1V model with regard to Chl *a* and effective diameter prediction demonstrates the benefits of both a robust parameterisation with regard to algal absorption, and minimising the number of unknowns when seeking the solution to the simplex non linear inversion. A

balance must be found between seeking to obtain maximal chemotaxonomic data (as given by the relative concentrations of the spectral basis vectors), allowing the model the necessary freedom to simulate the absorption of a wide variety of algal assemblages, and the robustness of the non-linear solution method, which ideally should solve for a minimal number of unknowns. In addition, any bio-optical data to which the inverse model is applied will have a limited number of wavelengths which represent the number of independent variables. In the case of hyperspectral data (as used here), whilst there may be several hundred wavelengths hypothetically available to solve with, there will be a finite number of pigment absorption bands which will effectively represent the number of independent variables, e.g. the nine bands shown in Fig 3.1B. It must also be appreciated that the intended application of the inverse absorption model is as a nested component of an inverse reflectance model [e.g. Roesler & Perry 1995, Roesler & Boss 2003]. These models will introduce other unknowns, e.g. those associated with gelbstoff absorption or backscattering components. Thus the choice between the 4V spectral mixing model, with it's greatly increased number of unknown parameters, and the simpler and more robust 1V model, must be dictated by the potential model application and both the cost and effectiveness of making accessory pigment returns available

3.6.4 Theoretical and Methodological Considerations

There is little doubt that the intracellular Chl *a* concentration, as given by c_i, has a profound effect upon both cellular absorption and physiological efficiency [Morel & Bricaud 1981, Raven 1984,]. The assumption of a constant c_i is therefore a somewhat artificial constraint that effectively ascribes all changes in packaging to size variations rather than changes in intracellular pigment density. Given that both size and c_i variations can result in apparently similar packaging effects [Morel & Bricaud 1981], it is unlikely that an inverse absorption model of the type presented here would be capable of distinguishing the effects on absorption of these two causal variables. The models presented here were tested with a variety of formulations allowing both c_i and size to be solved for as independent unknowns – in all cases the models were unable to predict either variable with success. Estimation of size using an inverse package effect formulation therefore appears to require either an assumption of constant c_i, or the

adoption of an empirical c_i to size relationship, such as those explicitly formulated with regard to cell volume [Moal *et al.* 1987, Montagnes *et al.* 1994, Menden-Deuer & Lessard 2000] or the approximate relationships suggested by the data of Bricaud *et al.* [1988] or Malone [1980].

This has obvious implications for the use of inverse absorption models of this type where photadaptation must be accounted for, for example with absorption data from increasing depth through a water column. Whilst the models tested here appear capable of predicting size and Chl *a* concentrations sufficiently accurately for high light adapted assemblages, it rather unlikely such models could be applied across assemblages of varying photoadaptive states. Variation in c_i related absorption with changing light history and other environmental variables [Raven 1984, Sosik & Mitchell 1991, Stramski *et al.* 2002] is known to be significant, and an inverse absorption model seeking to impose an algal size metric by keeping c_i constant is unlikely to perform successfully under highly variable photoadaptive states.

In addition to the simplifications imposed upon the inverse models with regard to intracellular Chl *a* concentration, there are considerations concerning other variables causal to absorption, primarily parameterisations of algal size. Chapter 2 demonstrates the utility of the effective diameter as the single most important descriptor of an algal size distribution, or in fact any size distribution of assumed spherical particles with regard to their optical properties [Mishchenko *et al.* 1997]. Chapter 2 also demonstrates that a single effective diameter value may be used to simulate the packaging of a wide variety of polydispersed algal populations with a maximum 5 % error, given the size distribution and optical properties of that population.

In addition to assessing potential variability associated with formulation of the inverse model, it is necessary to understand potential errors arising from the methods used to fractionate the size distribution data upon which the models are based and tested. The sensitivity study presented in Appendix I indicates that in the context of the large observed variability in the whole data set for absorption and related bio-physical descriptors, the sensitivity to changes in the assumed detrital parameters used in processing the algal size distribution data are generally small. Nevertheless, the study shows that errors from the detrital assumptions are most likely to be manifest in the c_i values of assemblages dominated by very small cells, and the unpackaged absorption values of assemblages dominated by very large cells. Such considerations emphasise the need for an increased knowledge of algal size and intracellular pigment concentration characteristics for natural algal samples. The ubiquitous presence of non-algal particulate matter [Roesler *et al.* 1989, Iturriaga & Siegel 1989] and the typically greatly increased polydispersity of natural samples in comparison to algal monocultures create methodological difficulties, particularly with regard to Coulter measurements of algal size distributions. Such difficulties can only be overcome by using numerical techniques, or employing methods other than those that are Coulter based e.g. flow cytometry [Green *et al.* 2003] or staining techniques [William *et al.* 1995].

3.7 Conclusions

The study demonstrates that assemblage size, as given by the effective diameter, is causal to algal absorption, and is the single factor responsible for the greatest variability (20 % to 45 %) in the Chl *a* specific absorption of natural algal assemblages. Such findings are consistent with anomalous diffraction theory [Morel & Bricaud 1981] and previous field studies [Bricaud *et al.* 1995, Ciotti *et al.* 2002]. The total intracellular accessory pigment concentration is also shown to have a significant effect upon absorption (12 % to 30 %), with the effects of c_i less significant (12 % to 16 %), as has been demonstrated previously [Bricaud *et al.* 1995, Stuart *et al.* 1998, Lohrenz *et al.* 2003]. The discernable effects of specific accessory pigments are limited to narrow spectral ranges corresponding to unique absorption bands, e.g. those of Chl *b* at 646 nm. The use of the anomalous diffraction approximation allows the unpackaging of algal absorption spectra, demonstrating the effective decoupling of the principal variables causal to absorption: effective size of the algal assemblage, the intracellular pigment concentration, and spectral variability associated with the absorption bands of specific accessory pigments.

Decoupling the variables causal to absorption allows the formulation of two inverse absorption models expressed in terms of the Chl *a* concentration, unpackaged absorption vectors associated with a variety of algal groups defined through their different accessory pigment complements, and the size of the algal assemblage expressed through the effective diameter. Both the simple 1V and more complex 4V models shows the ability to return Chl *a* concentrations within a sufficiently small error margin of 11 % to 16 %, perhaps a basic requisite for absorption models of this type. In addition both models demonstrate the capability to calculate the effective diameter of a wide variety of algal assemblages through matched absorption reconstructions, although predicted errors are somewhat larger than for Chl *a* predictions at 25 % to 30%. The 4V model, based on an admixture of assemblage specific unpackaged spectral basis vectors, is capable of returning accessory pigment concentrations. The model demonstrates an ability to return only those accessory pigments associated directly (Chl *b*) or vicariously (Allo) with unique absorption bands. Analysis of model performance indicates that care must be

taken to discern pigment related performance associated with causal absorption effects, and apparent ability of the model to predict minor or spectrally indistinct pigments based on covariant artifacts specific to the test data set. The apparent ability of the 4V model to predict Viola and But-fuco are treated as belonging to this last category, and should be disregarded for potential application. In addition to specific accessory pigments, the model is able to return total pigment concentrations with moderate success, a variable consistent with the criterion of being causal to absorption.

Whilst the 1V and 4V models are necessarily tested with direct measurements of absorption made with the filter pad technique, the models are designed for use with either *in situ* or space-based reflectance data for the detection of harmful algal blooms. This is reflected in the number of unknowns the models are required to solve for: two in the case of the 1V model and six in the case of the 4V model. Testing of model performance on directly measured absorption data is thus considered an initial step, and this will require the incorporation of a detrital term in the model [Bricaud & Stramksi 1990, Roesler *et al.* 1989]. Obviously model performance will also need to be reassessed if they are incorporated into an inverse reflectance model to represent the algal absorption component [e.g. Roesler & Perry 1995, Roesler & Boss 2003]. Nevertheless, the models demonstrate the ability to robustly derive bio-physical descriptors causal to algal absorption, in addition to limited accessory pigment data, and thus offer the ability to make distinctions between algal assemblage type other than purely on biomass. The utility of bio-optical HAB detection and monitoring systems lies in their potential ability to provide real-time data pertaining to the bulk algal population from autonomous instrumentation, rather than specific data relating to the presence of a few target toxic species. The performance of the absorption models is consistent with regard to the aims of such monitoring systems – the robust estimation of bio-physical descriptors allowing an assessment of the changes in algal biomass and assemblage type.

Chapter 4

Simulating the Optical Properties of Algal Cells Using a Two-Layered Spherical Geometry

4.1 Introduction

Understanding the relationship between the dissolved or particulate substances present in the upper ocean, their optical properties, and subsequent effects on the underwater light field is a principal goal of bio-optical oceanographers. The dominant ecological role of phytoplankton in both oligotrophic and coastal marine systems thus requires that the inherent optical properties of algal populations in natural waters be better understood. Establishing quantifiable relationships between these optical properties and causal cellular characteristics, such as algal size, morphology and intracellular constituent concentrations, is of great importance in the development of bio-optical tools for marine biogeochemical and ecological applications.

The equations of radiative transfer describe the propagation of light through the sea, relating radiative field structure to the inherent optical properties or IOPs [Preisendorfer 1976]. The distribution of radiance within the sea, and the radiance emerging from the sea surface, is thus determined by the spectral nature of the volume scattering and absorption coefficients. Radiative transfer models used for the interpretation and inversion of ocean colour data [Morel & Prieur 1977, Roesler & Perry 1995] have parameterised these processes in the form $R \propto b_b/(a+b_b)$, where R is the reflectance, b_b is the backscattering coefficient and a is the absorption coefficient. Understanding the spectral contribution of algal cells to the bulk backscattering coefficient - the integrated angular scattering that is responsible for returning light to the surface of the sea – is thus crucial to ocean colour studies.

Few direct spectral measurements of algal backscattering or angular scattering have been made historically, although the recent commercial availability of single or multiple angle backward scattering sensors may redress this situation. Mie theory has provided a theoretical alternative to direct measurement, and the current understanding of algal scattering properties is largely based on Mie simulation [Bricaud & Morel 1986, Ahn *et al.* 1992, Stramski *et al.* 2001]. However, whilst the absorption, attenuation and total scattering of algal cultures have been successfully simulated using Mie theory [*ibid.*], and

the related anomalous diffraction approximation (ADA) [Van de Hulst 1957], the few direct measurements made of algal angular scattering suggest that Mie theory is less well suited to describe backward scattering [Quinby-Hunt *et al.* 1989, Volten *et al.* 1998, Vaillancourt *et al.* 2004]. These studies, and others investigating the effect of internal cellular structure on angular scattering [Witkowsi *et al.* 1993, 1998], and the application of Mie models for algal radiative transfer [Stramski & Piskozub 2003] indicate the importance of internal structure and non-sphericity on algal scattering at large angles.

The extensive use of Mie and ADA modelling in marine bio-optics lies in the relative simplicity of implementation: a spherical geometry with a homogenous refractive index structure can be assumed. It is known that eukaryotic phytoplankton possess heterogeneous intracellular refractive indices, associated with the presence of various membrane systems and intracellular organelles. These include cellular coatings (composed of silicate, cellulose or calcite), membrane bound highly absorbing chloroplasts (containing the chromoprotein complexes necessary for light harvesting and photosynthesis), other membrane bound organelles (such as the mitochondria and nucleus), and regulatory/storage devices (such as gas vacuoles and starch granules). The fact that such internal structures are visible under light microscopy indicates that they are of varying refractive index, and therefore can influence both the internal and external electromagnetic field associated with a cell.

The need to assess the optical impacts of varying internal refractive indices has been addressed by several researchers, with implementations of layered geometry algal optical models. These models have employed either two-layered spheres with the chloroplast as the core [Aas 1984, Zaneveld & Kitchen 1995] or three layered spheres with the chloroplast as the central layer [Bricaud *et al.* 1992, Kitchen & Zaneveld 1992, Zaneveld & Kitchen 1995], using volume equivalent refractive index schemes to compare IOPs for homogeneous and heterogeneous spheres. Such studies appear to confirm that backscattering is the IOP most affected by cellular heterogeneity, with heterogeneous geometries resulting in both spectral changes and increases in backscattering magnitude of between 2 and 50. It also appears that adopting a heterogeneous geometry has little

effect on absorption and lesser effects on attenuation and total scattering than backscattering – such findings are consistent with the success of homogenous geometry models in simulating algal absorption, attenuation and total scattering [Bricaud & Morel 1986, Bricaud *et al.* 1988].

The models described above were used either for small wavelength ranges [Kitchen & Zaneveld 1992, Zaneveld & Kitchen 1995], or to investigate the backscattering of coccolithophorids [Bricaud *et al.* 1992], which can be regarded as exceptional backscatterers in the algal milieu due to their very high refractive index calcite coating. Such studies demonstrate both the need and the computational ability to produce broadly accessible spectral algal backscattering simulations based on a heterogeneous geometry; a need that is reinforced by the continued emergence of bio-optical techniques and instrumentation for algal and coastal monitoring applications [Cleveland *et al.* 2004]. An improved understanding of the spectral nature of algal backscattering is considered of particular importance, given the well understood effects of anomalous diffraction on angular scattering [Van de Hulst 1957, Zaneveld & Kitchen 1995], and the reliance of phycologically oriented bio-optical inversion techniques on spectral discrimination [Roesler & Perry 1995, Garver & Siegel 1997, Roesler & Boss 2002].

The numerical and computational capability for heterogenous cell modelling has existed for several decades [Aden & Kerker 1951, Meyer 1979]. The relatively sparse implementation of such models regarding algal optics may have resulted at least in part from the paucity of knowledge concerning the optical and morphometrical properties of algal organelles. These difficulties are compounded by the difficulties of translating the highly variable biochemical and structural complexities of eukaryotic cells into an optically or biogeochemically equivalent simple model geometry such as a layered sphere. However, the adoption of a simple layered geometry can allow a simpler perspective *a priori*: the dependencies of heterogeneous algal optical models can be reduced to the morphometrics of algal ultrastructure, and the determination of suitable effective refractive indices for the primary optical cellular structures. These can be considered to be the chloroplasts as the primary absorbing organelles, the watery

cytoplasm typically dominating cell volume, and the external cellular membrane as a high refractive index peripheral layer [Bryant 1969, Aas 1996, Zaneveld & Kitchen 1995].

This study will thus seek to investigate the optical properties of algal cells and populations using a two-layered spherical geometry, chosen as the simplest possible heterogeneous structure that has shown itself capable of reproducing measured algal angular scattering properties [Quinby-Hunt *et al.* 1989]. This geometry reduces the effective algal components to a highly absorbing chloroplast containing the protein bound cellular pigments, and a weakly absorbing cytoplasm [Zaneveld & Kitchen 1995, Stephens 1995]. Representative value ranges for relative algal chloroplast volume and complex refractive index will be established, based upon published values. Simple, single cell models will be used to demonstrate the effects of varying cell geometry on optical physiology as given by the package effect [Morel & Bricaud 1981, Geider & Osborne 1987], and infer a default cellular geometry. Models assuming this simplified heterogeneous geometry will then be used in conjunction with measured optical and algal size data from natural algal assemblages in the southern Benguela to produce simulated inherent optical properties of typical algal assemblages in an upwelling system.

4.2 Model Theory and Structure

4.2.1 Single Particle and Wavelength Mie and Aden-Kerker Models

Whilst the details of both Mie [1908] and Aden-Kerker [1951] theory are outside the scope of this study, the implementation of these theories with regard to algal optics can be briefly described as follows (more detail can be found in Morel & Bricaud [1986] or Van de Hulst [1957]). The optical properties of a homogeneous particle interacting with an electromagnetic wave are dependent upon the Mie size parameter α, and complex refractive index m [Morel & Bricaud 1986]. The Mie size parameter is given by:

$$\alpha = \pi d / \lambda_w \tag{4.1}$$

where d is the particle diameter and λ_w is the wavelength in the surrounding medium – water in this case. The complex refractive index is given by:

$$m = n - n'i \tag{4.2}$$

where the real part n determines the phase velocity of the propagating wave, and the imaginary part n' determines the flux decay. Note that the effective refractive index is a relative value dependent upon the surrounding medium – all future discussion of refractive index values will assume a relative refractive index in water, with m_{water}=1.334-0i [Morel & Bricaud 1986]. The effects of employing a two-layered particle geometry are relatively simple: a new size parameter q is introduced describing the core:particle diameter (or radius) where $q=d_{core}/d$. In addition the refractive indices of both the chloroplast and cytoplasm layers must be explicitly described: the subscripts h for homogeneous, *chlor* for chloroplast, and *cyto* for cytoplasm will be used for this purpose where:

$m_h = n_h - n'_h i$	is the refractive index of a homogeneous particle
$m_{chlor} = n_{chlor} - n'_{chlor} i$	is the refractive index of the chloroplast layer

$m_{cyto} = n_{cyto} - n'_{cyto}\, i$ is the refractive index of the cytoplasm layer (4.3)

The relationship between the imaginary refractive index and the absorption coefficient of the cellular material a_{cm} is useful when considering the effects of intracellular pigment concentration on the refractive index and is given by:

$$n' = a_{cm}\lambda_w / 4\pi \tag{4.4}$$

The principal particle optical properties dependent upon these parameters under both Mie and Aden-Kerker theory can be considered to fall into two categories. The optical efficiency factors for absorption Q_a, attenuation, Q_c and scattering Q_b have no angular dependence and can be calculated at relatively little computational cost from complex "Mie coefficents" expressed through spherical Bessel functions [Van de Hulst 1957, Morel & Bricaud 1986]. The volume absorption a, attenuation c and scattering b coefficients can be calculated from these efficiency factors (absorption is used as an example, analogous expressions are used for other coefficients):

$$a = (N/V)sQ_a \tag{4.5}$$

where N is the number of cells in volume V, and s is the geometrical cross section of the cell.

Optical properties with an angular dependence θ (assuming rotational symmetry) are calculated at greater computational cost and include the volume scattering function (VSF) $\beta(\theta)$, and the phase function $\overline{\beta}(\theta)$ (the scattering normalised VSF), described by:

$$b = 2\pi \int_0^{\pi} \beta(\theta)\sin\theta\, d\theta \tag{4.6}$$ and $$\overline{\beta}(\theta) = \beta(\theta)/b \tag{4.7}$$

Integrated scattering parameters in the backward direction include the volume backscattering coefficient b_b, the backscattering probability factor $\tilde{b}_b$, and the backscattering efficiency factor Q_{bb} described by:

$$b_b = 2\pi \int_{\pi/2}^{\pi} \beta(\theta) \sin\theta d\theta \tag{4.8}$$

$$\tilde{b}_b = b_b / b = 2\pi \int_{\pi/2}^{\pi} \bar{\beta}(\theta) \sin\theta d\theta \tag{4.9}$$

$$Q_{bb} = \tilde{b}_b Q_b \tag{4.10}$$

4.2.2 Size Distributions and Polydispersions

Algal assemblages are typically polydispersed with regard to size, and can be described by a particle size distribution $F(d)$, where d is the particle diameter, and $F(d)d(d)$ is the number of particles per unit volume in the size range $d \pm ½\, d(d)$. Using absorption as an example (analogous expressions may be used for other coefficients) the absorption efficiency factor representing the mean of a size distribution (as signified by the overbar) can be described as [Morel & Bricaud 1986]:

$$\bar{Q}_a = \frac{\int_0^{\infty} Q_a F(d) d^2 d(d)}{\int_0^{\infty} F(d) d^2 d(d)} \tag{4.11}$$

and the resultant volume absorption coefficient is given by either:

$$a = (\pi/4) \int Q_a F(d) d^2 d(d) \tag{4.12}$$

or, if the result of Equation 4.11 is used:

$$a=(\pi/4)\bar{Q}_a\int F(d)d^2\,d(d) \qquad (4.13)$$

Note that such expressions can be used for the determination of experimental optical efficiency factors, and subsequent refractive index determinations, if measured IOPs and size distributions are known [Bricaud & Morel 1986, Stramski *et al.* 1988].

4.2.3 Anomalous Dispersion and Spectral Refractive Indices

The above expressions can be applied through a range of wavelengths, and the wavelength dependency λ can be considered implicit in equations 4.2 to 4.13. An important consideration in spectral application of particle optical theories is the behaviour of the refractive index in the vicinity of absorption bands. In areas of weak absorption, or low values of the imaginary refractive index, the real refractive index typically decreases with wavelength – termed normal dispersion [Van de Hulst 1957]. However, in the presence of absorption bands, or significant spectral change with wavelength in the imaginary refractive index, the real refractive index increases sharply with wavelength – termed anomalous dispersion [*ibid.*]. This phenomenon can lead to significant spectral variability in the real refractive index and thus considerable spectral shape in the attenuation and various scattering coefficients, typically termed anomalous diffraction.

The dependence of the real on the imaginary part of the refractive index is described by Ketteler-Helmholtz theory [Van de Hulst 1957, Bohren & Huffman 1983], and has often been quantified in application to algal refractive indices using a series of oscillators (representing discrete absorption bands) based on the Lorentz-Lorentz equations [Bricaud & Morel 1986, Stramski *et al.* 1988, Zaneveld & Kitchen 1995]. An alternative to the somewhat intricate use of a series of summed Lorentzian oscillators can be found in the Kramers-Kronig relations [Van de Hulst 1957, Bohren & Huffman 1983], which allow the spectral variations in the real refractive index to be calculated as a Hilbert transform of the imaginary refractive index. The application of the Kramers-Kronig relations to describing the anomalous dispersion of algal refractive indices has been successfully demonstrated [Bernard *et al.* 2001, Naqvi *et al.* 2004]. The Kramers-Kronig relations are

therefore used here to calculate spectral variations in the real refractive index arising from those in the imaginary refractive index. These follow the notation of Bricaud & Morel [1986], where the spectral variations $\Delta n(\lambda)$ vary around the central part of the real refractive index 1+ε, as given by:

$$n(\lambda)=1+\varepsilon+\Delta n(\lambda) \tag{4.14}$$

4.2.4 The Anomalous Diffraction Approximation

Somewhat different to the anomalous dispersion effects described above is the anomalous diffraction approximation (ADA), first described by Van de Hulst [1957]. The ADA offers approximations to the absorption and attenuation optical efficiency factors using relatively simple algebraic formulae, based on the assumptions that the particle is large relative to wavelength ($\alpha>>1$) and the refractive index is small ($m-1<<1$). These important conditions allow the assumption that a ray of light traversing a particle suffers no deflection, and that the attenuation within the particle is thus related simply to pathlength. The ADA has been used extensively in algal optics [Bricaud & Morel 1986, Bricaud *et al.* 1988, Ahn *et al.* 1992], partially due to its computational economy, but more importantly because it allows the effects of the real and imaginary refractive indices on absorption and scattering to be decoupled. This allows the calculation of the imaginary refractive index for algal assemblages, assuming homogeneous geometry and given algal absorption and size distribution data [Bricaud & Morel 1986, Stramski *et al.* 1988]. The ADA expression for the absorption efficiency factor is given by:

$$Q_a=1+\frac{2e^{-\rho'}}{\rho'}+2\frac{e^{-\rho'}-1}{\rho'^2}, \qquad \rho'=a_{cm}d=4\alpha n' \tag{4.15}$$

where ρ' is the absorption optical thickness. Equations 4.13 and 4.15 are thus used iteratively in this study to determine homogeneous refractive index data in conjunction with measured algal absorption and particle size distribution data. Whilst it is possible to derive an ADA approximation for two-layered spheres [Quirantes & Bernard 2004], such

a formulation is not used here – all two-layered calculations use the exact Aden-Kerker formulae.

4.2.5 The Package Effect

The package effect parameter $Q_a^*(\lambda)$ describes the consequence of placing the absorbing cellular material in particulate as opposed to solution form, and is the ratio of the particulate Chl *a*- specific absorption $a^*(\lambda)$ to the Chl *a*-specific absorption of the same material placed perfectly in solution $a_{sol}^*(\lambda)$. It is given by [Morel & Bricaud 1981]:

$$Q_a^* = \frac{a^*}{a_{sol}^*} \qquad (4.16) \qquad Q_a^* = \frac{3\ Q_a}{2\ a_{cm} d} \qquad (4.17)$$

An additional relationship can be described which introduces the intracellular Chl *a* concentration c_i (kg m^{-3}):

$$a_{sol}^* = \frac{a_{cm}}{c_i} \qquad (4.18)$$

It should be noted that equation 4.17 is an exact derivation, and is not limited (from a strict theoretical perspective) by the same assumptions as the ADA with regard to size and refractive index. This will obviously not hold true if the Q_a term in Equation 4.17 is calculated with the ADA as opposed to an exact solution [Latimer 1984, Geider & Osborne 1987]. Cellular packaging has important physiological consequences, as it will impact upon the ability of a cell to make incident energy available for photosynthesis [Raven 1984, Finkel & Irwin 2000], and the ability of a cell to dissipate energy through fluorescence [Babin *et al.* 1996]. The effect of varying cellular geometry on the package effect is considered here, and an expression for the package effect of a two-layered sphere, based on Gladstone-Dale volume equivalence [Aas 1996], is derived as:

$$Q_a^* = \frac{3}{2\left(a_{cm}^{core} q^3 + a_{cm}^{shell}[1-q^3]\right)d} \quad (4.19)$$

where Q_a is the absorption efficiency factor of the two layered sphere (dimensionless), a_{cm}^{core} is the absorption of cellular material for the particle core (m^{-1}), a_{cm}^{shell} is the absorption of cellular material for the particle shell (m^{-1}), and q is the ratio of the core : shell radii (dimensionless) [A. Quirantes, pers. comm.] The above expression is obviously dependent upon the validity of the volume equivalence term for the effective optical thickness, and it can be tested against a direct calculation of the package effect, as follows. If the imaginary refractive indices of a hypothetical two-layered particle population are known, the a_{cm} values for both layers can be calculated from equation 4.4. The hypothetical total absorption in solution can be calculated as:

$$a_{sol} = \frac{\pi}{6}\int F(d)d^3 d(d)\left[a_{cm}^{core} q^3 + a_{cm}^{shell}\left(1-q^3\right)\right] \quad (4.20)$$

Assuming the particulate absorption is known from model output, the package effect parameter can then be calculated with equation 4.16.

All optical modelling in this study for both heterogeneous and homogeneous particles, apart from package effect calculations as discussed above, were made with the two-layered code of Toon & Ackerman [1981] with size bins of 1 μm and an angular resolution of 0.1°. The suitability of the Toon & Ackerman code for homogeneous modelling was verified by comparison with the Bohren & Huffman [1983] code – identical results were found across a wide variety of size and refractive indices. All models were run under a combined Matlab R13 (The Mathworks) and Fortran (Compaq Visual Fortran V6.5) environment.

4.3 Morphometrics and Refractive Indices of the Algal Cell

4.3.1 Chloroplast Morphometrics

The chloroplast of an autotrophic eukaryotic cell is the membrane bound organelle containing the highly absorbing pigment-protein complexes responsible for light harvesting and photosynthesis, and it will exert a profound optical effect. Algal related studies investigating the effects of cellular internal structure on scattering [Witkowski *et al.* 1993, 1998] and absorption packaging [Geider & Osborne 1987] indicate the importance of chloroplasts in modifying both the absorbing and scattering properties of algal cells.

Imposing a simple two-layered geometry upon a hypothetical algal cell thus requires some knowledge of the variability of chloroplast size, or more appropriately, the relative chloroplast volume. Phytoplankton cells exhibit wide variability with regard to chloroplast morphology: the total number of chloroplasts is highly variable, and they exhibit a wide variety of shapes, size and membrane structure. Physiology is also known to strongly influence cell structure: photoadaptation, temperature, life stage, nutrient and trace element history can all influence chloroplast volume, location, internal structure and internal pigment density [Jeffrey & Vesk 1977, Thinh 1983, Rosen & Lowe 1984]. Table 4.1 details relative chloroplast volumes Vv derived from published data for a range of cultured algal species, which show Vv values ranging from 4.4 % to 57 % (cf. 3 % to 66 % from Geider & Osborne [1987]). There appears no significant relationship between cell size, as given by the equivalent volume spherical diameter, and chloroplast volume – this may be a function of the small data set in Table 4.1 (published morphometric chloroplast data is scarce) which incorporates a wide range of growth conditions and species.

Nevertheless, within the context of this study, it is reasonable to assume a size-independent relative chloroplast volume of 20 % (the median value from Table 4.1) as a first approximation for a spherical algal geometry. The use of a size invariant Vv value can be justified by evidence suggesting that the algal protein to Chl *a* ratio is relatively

invariant to changing cell size, and thus the proportion of cytoplasmic mass devoted to chloroplasts is independent of size [Hitchcock 1982, Moal *et al.* 1987, Montagnes *et al.* 1994]. To aid visualisation in comparison to a typical transmittance electron micrograph, a Vv value of 20 % would result in an inner relative radius q of 0.58 if the inner layer of a two-layered sphere is considered the chloroplast. Previous modelling studies employing heterogeneous geometries with dedicated chloroplast layers have employed relative chloroplast volumes of Vv =41 % [Zaneveld & Kitchen 1995], Vv=58 % [Latimer 1984], and Vv=27 % to 66% [Bricaud *et al.* 1992]. These are in all cases considerably higher than the preliminary Vv value assumed here, and fall amongst the higher values reported in Table 4.1. Nevertheless, a Vv value of 20 % for a dedicated chloroplast layer is considered appropriate given the available morphometric data. Additionally, the primary focus of this study is ocean colour related applications in productive upwelling waters, and thus high-light adapted algae from the upper few metres depth. The assumption of a relatively small chloroplast volume is consistent with observations of smaller chloroplast volume in high-light adapted cells, as shown in Table 4.1.

Table 4.1 Relative chloroplast volume (*Vv* in %) for a range of cultured phytoplankton species under varying growth conditions. The paucity of published data regarding chloroplast morphometry has necessitated the use of different methods to generate chloroplast volume data, as given by the *Vv* methods column. The upper box represents cultures considered low light (< 200 µE m^{-2} s^{-1}), and the lower box high light (> 200 µE m^{-2} s^{-1}). Where necessary growth illuminance quoted in lux have been converted with 1 µE m^{-2} s^{-1} = 60 lux. EVSD=equivalent volume spherical diameter, *Av*=relative area, *d*=diameter, TEM=transmittance electron micrograph.

Species	Class	EVSD µm	*Vv* %	Chloroplasts No.	Growth Light [µE m^{-2} s^{-1}]	*Vv* Method	Reference
Phaeodactylum tricornutum	Bacillariophyte	2.2	20.7	two large	5	*Av* quoted/*d* from TEM	Janssen *et al.* 2001
Phaeodactylum tricornutum	Bacillariophyte	2.2	8.9	two large	50	*Av* quoted/*d* from TEM	Janssen *et al.* 2001
Nannochloropsis	Eustigmophyte	2.7	57.0	one large	35	*Vv* quoted	Fisher *et al.* 1998
Aureococcus anophagefferens	Pelagophyte	2.8	12.5	one large	unknown	TEM spheroidal geometry	Pitcher *et al.* 1999
Pavlova pinguis	Haptophyte	3.6	14.9	one large	unknown	TEM spheroidal geometry	Green 1980
Amphidinium carterae	Dinophyte	4.3	26.4	one large	unknown	*Vv* quoted	Jenks & Gibbs 2000
Cryptomonas lis	Cryptophyte	4.9	25.8	two large	10	*Av* quoted	Thinh 1983
Chlamydomonas applanata	Chlorophyte	5.1	52.0	one large	30	*Vv* quoted	Visviki 2000
Cyclotella cryptica	Bacillariophyte	5.7	19.8	several	5	*Av* quoted/*d* from TEM	Janssen *et al.* 2001
Cyclotella cryptica	Bacillariophyte	6.4	4.4	several	50	*Av* quoted/*d* from TEM	Janssen *et al.* 2001
Symbiodinium spp	Dinophyte	8.1	17.0	many	50	*Vv* quoted	Muller-Parker *et al.* 1996
Symbiodinium spp	Dinophyte	8.1	33.0	many	5	*Vv* quoted	Muller-Parker *et al.* 1996
Cyclotella meneghiniana	Bacillariophyte	16.1	21.5	several	10	*Vv* quoted	Rosen & Lowe 1984
Cyclotella meneghiniana	Bacillariophyte	16.1	28.6	several	107	*Vv* quoted	Rosen & Lowe 1984
Glenodiniopsis steinii	Dinophyte	16.8	24.8	one large	155	*Vv* quoted	Highfill & Pfiester 1992
Nannochloropsis	Eustigmophyte	2.7	29.0	one large	650	*Vv* quoted	Fisher *et al.* 1998
Amphidinium carterae	Dinophyte	4.3	16.7	one large	unknown	*Vv* quoted	Jenks & Gibbs 2000
Cryptomonas lis	Cryptophyte	7.3	7.6	two large	260	*Av* quoted	Thinh 1983
Diatoma tenue	Bacillariophyte	7.8	16.0	several	200	*Vv* quoted	Sicko-Goad & Stoermer 1979

4.3.2 Real Part of the Algal Refractive Index

The real refractive index of a homogeneous algal cell is the primary causal variable with regard to the magnitude of algal scattering [Morel & Bricaud 1986]. Whilst the same is true as concerns a cell of heterogeneous geometry, complexities are introduced by the presence of additional refractive index boundaries corresponding to simulated internal structures [Meyer 1979, Zaneveld & Kitchen 1995]

The assumption of a two-layered geometry gives critical importance to the establishment of suitable chloroplast refractive index ranges. It should be realised that chloroplasts are far from homogeneous, and the adoption of a single refractive index value or spectra is itself a simplification. The chloroplast is enclosed in 2 to 4 outer membranes, and consists of stacked thylakoid membranes containing the pigment-protein complexes, embedded within the stroma. Thylakoid stacking and areal chlorophyll density is variable [Rosen & Lowe 1984, Berner *et al.* 1989], and the thylakoid membranes can exhibit considerable birefringence [Paillotin *et al.* 1998]. Changes in membrane stacking and transparency can affect light absorption due to an intracellular package effect [Jennings & Zucchelli 1985, Berner *et al.* 1989]. However, accounting for phenomena arising from chloroplast heterogeneity is beyond the scope of this study, and the chloroplast will necessarily be considered homogeneous here.

Table 4.2 provides considerable evidence that the real refractive index of chloroplasts, or the material contained therein, are considerably higher than values published for homogeneous cells. The chloroplast related data, from a wide range of sources, display central real refractive index $1+\varepsilon$ values of between 1.06 to 1.22 (excluding highest and lowest values as extrema), as compared to homogeneous cell values of 1.01 to 1.09 [Bricaud *et al.* 1988, Ahn *et al.* 1992]. However, taking chloroplast $1+\varepsilon$ values of 1.06 to 1.22, a cytoplasm $1+\varepsilon$ value of 1.02, and a relative chloroplast volume of 20%, the homogeneous volume equivalent $1+\varepsilon$ values under the Gladstone-Dale scheme range from 1.028 to 1.060 consistent with experimentally determined homogeneous values [*ibid.*]. Whilst simple volume equivalent or effective medium schemes are approximate from an optical perspective [Chylek & Videen 1998], this consistency indicates that the

chloroplast volume and real refractive index ranges suggested by Tables 4.1 and 4.2 are entirely appropriate from both an optical and cellular composition perspective. For preliminary analyses, a chloroplast $1+\varepsilon$ value of 1.14 will be used, as the extrema rejected mean from Table 4.2.

Few measurements of cytoplasm refractive indices have been published – Table 4.2 shows the single value of $1+\varepsilon=1.015$ [Charney & Brackett 1961]. Previous studies have adopted either this value [Bricaud *et al.* 1992] or similar values of 1.02 [Kitchen & Zaneveld 1992, Zaneveld & Kitchen 1995]. Variations in the algal real refractive index are typically considered as due to changes in the relative amounts of cellular water and solids, rather than changes in the chemical composition of solids [Aas 1996, Stramski 1999]. The low reported refractive index values for cytoplasm are thus consistent with an expected high water content [Aas 1996]. A value of $1+\varepsilon=1.02$ for cytoplasm will be adopted for this study.

Table 4.2 Published values of the real part of the refractive index for a range of cellular structures from terrestrial plants and algae, relative to water. The mean values for chloroplasts (including those for thylakoid membranes, pigment bound proteins, and light harvesting complexes) are calculated with the highest and lowest values excluded, whilst the mean value for external cellular membranes excludes values for calcite coatings (these are considered specific to the coccolithophore case). RI =refractive index, LHC=light harvesting complex.

Organism/Organelle	Central RI Value (1+ε)	Method	Reference
Spinach/chloroplast	1.065 - 1.199	Photovoltage	Paillotin *et al.* 1998
Spinach/chloroplast	1.030 - 1.060	Immersion/refractometer	Bryant *et al.* 1969
A. carterae/chloroplast	1.199	Forster transfer	Kleima *et al.* 2000
Rb. sphaeroides/LHC II	1.220	*In vitro* absorption shift	Andersson *et al.* 1991
Spinach/chloroplast	1.130	*In vitro* absorption shift	Renge *et al.* 1996
Maize/chloroplast	1.150 - 1.179	Forster transfer	Cinque *et al.* 2000
Zea Mays/chloroplast	1.124	*In vitro* absorption shift	Caffarri *et al.* 2001
Secale cereale/LHC II	1.15 - 1.39	*In vitro* absorption shift	Gruszecki *et al.* 1999
C. pyrenoidosa/chloroplast	1.060	Phase contrast	Charney & Brackett 1961
Chlorella/chloroplast	1.080	Mueller matrix	Quinby-Hunt *et al.* 1989
General /chlorophyll	1.140 - 1.150	Lorentz molecular weight	Aas 1996
General /protein	1.132 - 1.199	Literature review	Aas 1996
Modelled cell/chloroplast	1.095	assumed model value	Zaneveld & Kitchen 1995
C. pyrenoidosa/cytoplasm	1.015	Phase contrast	Charney & Brackett 1961
Modelled cell/cytoplasm	1.02	assumed model value	Kitchen & Zaneveld 1992
Modelled cell/cytoplasm	1.015	assumed model value	Bricaud *et al.* 1992
Chlorella/cell membrane	1.130	Mueller matrix	Quinby-Hunt *et al.* 1989
Modelled cell/calcite coating	1.22	assumed model value	Bricaud *et al.* 1992
Modelled cell/cell membrane	1.09	assumed model value	Zaneveld & Kitchen 1995
Algal/carbohydrate forms	1.162	Literature review	Aas 1996

Mean chloroplast value	1.136(±0.053)
Mean cytoplasm value	1.017(±0.003)
Mean membrane/coating value	1.127(±0.036)

4.3.3 Imaginary Part of the Algal Refractive Index

A useful conceptual framework in algal optics is to consider that unpackaged Chl *a*-specific absorption has theoretical maxima, based on either absorption measurements of Chl *a* in solvent, or of isolated chromoproteins [Bricaud *et al.* 1995, Johnsen *et al.* 1994a]. Based on this construct, the unpackaged Chl *a*-specific absorption can be normalised to a theoretical maximum at ~ 675 nm - the wavelength of the red Chl *a* absorption peak where Chl *a* is considered the sole absorber [*ibid.*]. Under a two-layered geometry, it is possible to combine equations 4.4, 4.18 and the Gladstone-Dale expression of volume equivalence to allow the calculation of the imaginary refractive index of the chloroplast layer at 675 nm:

$$n'_{chlor}(675) = \frac{675}{n_{media}} \frac{\pi c_i a^*_{sol}(675)}{4Vv} \qquad (4.21)$$

where n_{media}=1.334 and Vv is the relative chloroplast volume. Equation 4.21 thus describes the relationship between the intracellular Chl *a* concentration, chloroplast volume, chloroplast imaginary refractive index, and cellular absorption, based on the assumption that the cytoplasm layer has no significant absorption at 675 nm.

Equation 4.21 offers a useful starting point to examine the potential range and behaviour of the imaginary refractive index for algal chloroplasts n'_{chlor}, or more accurately the simulated chloroplast layer in a hypothetical two-layered geometry. It can be seen that n'_{chlor} is dependent upon the relative chloroplast volume and the intracellular Chl *a* concentration c_i, based on Gladstone-Dale volume equivalence. Whilst it would be more desirable to employ chloroplast (as opposed to intracellular) Chl *a* concentrations, and thus dispense with the need for a volume equivalence scheme, such chloroplast data are very rare (unknown to the author). The dependence of n'_{chlor} upon c_i is therefore considered a necessary approximation, and at least allows consideration of algal optical properties armed with a considerable body of published c_i data [e.g. Taguchi 1976, Malone 1980, Bricaud *et al.* 1988]. In addition, published relationships between c_i and $n'_k(675)$ for homogeneous cells [Stramski 1999, Equation 9] can be used for

comparative purposes. A reasonable range of algal c_i values could be considered 0.5 kg m^{-3} to 10 kg m^{-3} [Taguchi 1976, Malone 1980, Bricaud *et al.* 1988] – these would produce homogeneous $n'_h(675)$ values of ~0.0005 to 0.011, using Equation 4.18 and $a^*_{sol}(675) = 0.027$ mg^{-1} m^{-2} [Johnsen 1994a], or values of 0.0017 to 0.011 using the Stramksi formulation. These data ranges compare well with published values [Ahn *et al.* 1992, Stramski *et al.* 2001], and confirm the use of the Stramski formula as a validation check. The equivalent chloroplast $n'_{chlor}(675)$ value range using equation 4.21 with Vv=20 % is ~ 0.0027 to 0.054, as compared to a range from the Stramski formula of ~0.0037 to 0.051. Whilst the Stramski formula is designed for use with homogeneous cells as opposed to chloroplasts, the close comparison of the two $n'_{chlor}(675)$ data ranges (from Equation 4.21 and the Stramski formula) is encouraging, given their derivation from very different sources. Previous heterogeneous modelling studies have employed n'_{chlor} values of 0.024 in the 670 nm region [Zaneveld & Kitchen 1995] or 0.04 to 0.05 at 442 nm [Quinby-Hunt *et al.* 1989], which fall within the proposed range of values from Equation 4.21.

The spectral shape of the cellular imaginary refractive indices will be discussed in detail later, in relation to the application of inverse refractive index models to measured algal optical data. Briefly, the spectral imaginary refractive index of the chloroplast layer can be estimated to a first order using volume equivalence, if homogeneous and cytoplasm data are known or assumed. Few imaginary refractive index data are available for cellular cytoplasm. However, it would appear that the cytoplasm is weakly absorbing, with an exponential type spectral shape typical of non-pigmented organic compounds [Stephens 1995]. The cytoplasm imaginary refractive index is thus expected to be small but significant at blue wavelengths, decreasing to insignificant values in the red.

For preliminary single particle analyses to investigate the broad characteristics of a two-layered geometry, an n'_{chlor} value of 0.02 and an n'_{cyto} value of 0.0005 will be used, considered typical values in the Soret spectral region, e.g. 435 nm. Detailed spectral data for the imaginary refractive indices will be revisited later.

4.3.4 Cellular Morphometrics

Having established reasonable morphometric and refractive index data ranges, it is necessary to assess the assignment of the two layers available - is it more appropriate from a general perspective to model the chloroplast as the inner or outer layer? It must be appreciated that such a synthetic construct is a vast oversimplification - chloroplast phototaxis is a known phenomena [Rosen & Lowe 1984, Stephens 1995] and the variability of chloroplast morphometrics has been discussed previously. Nevertheless, a simplified cell geometry can be mathematically simulated, and to this end the implications of selecting a central or peripheral chloroplast layer can be assessed.

Figure 4.1 shows the optical efficiency factors and backscattering probability of particles using the geometrical and refractive index values discussed above, for a range of Mie size values. The α values used are compatible with a particle diameter range of 1 μm to 96 μm and a wavelength of 435 nm. The efficiency factors of interest to this discussion are the absorption efficiency factor Q_a and the package effect parameter Q_a^*. Figure 4.1E demonstrates the considerable difference in packaging between the inner and outer chloroplast models – the inner model has Q_a^* values approximately up to 40 % lower (meaning that the absorption packaging is approximately 40 % higher). In comparison, the packaging of the homogeneous and outer layer model differ by a maximum of 10 %. Figure 4.1C reveals that it is the difference in Q_a values that is the predominant cause of these packaging differences. The inner chloroplast model has considerably lower absorption efficiency factors, particularly so at higher sizes where it tends toward a lower limiting value than the theoretical maximum of one [Morel & Bricaud 1986]. The two means of calculating the package effect for a two-layered geometry (Equations 4.19 and 4.20) produced equivalent results, indicating that newly derived Equation 4.19 is an appropriate formulation.

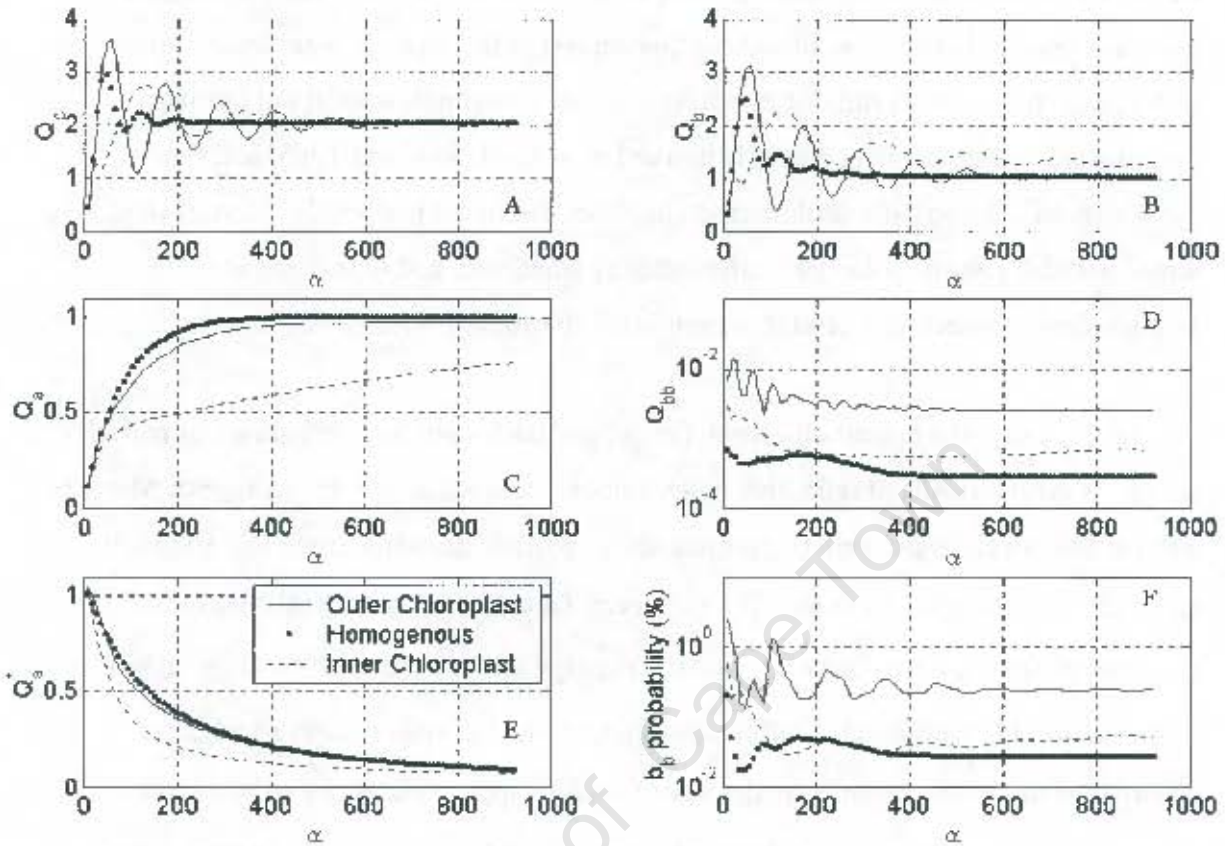

Figure 4.1 Optical efficiency factors and backscattering probability against Mie size parameter α for two-layered and homogenous spheres. Two-layered spheres in both inner (dashed line) and outer (solid line) chloroplast configurations have refractive indices of m_{chlor}=1.14 – 0.02i and m_{cyto}=1.02 – 0.0005i. Homogenous spheres (dots) have a refractive index of m_h=1.044 - 0.0044i, calculated as volume equivalent to the two-layered geometry using Gladstone-Dale equivalence. Relative chloroplast volume is set to 20%. Note the log scales for the two backscattering related graphs.

The outer chloroplast model appears to be a more appropriate choice for general application for several reasons. It can be assumed, from a general phycological cost-benefit perspective, that an algal cell will benefit from minimising absorption packaging [Raven 1984]. Direct measurements of absorption packaging indicate that packaging tends to be lower than predicted by theory, i.e. Q_a^* is closer to one [Geider & Osborne 1987, Osborne & Geider 1989]. Given both these factors, it would thus seem reasonable to adopt a model geometry that minimises packaging – the outer chloroplast model. Previous studies have also suggested that a high refractive index peripheral layer is beneficial to a cell in terms of light trapping [Latimer 1984, Geider & Osborne 1987, Zaneveld & Kitchen 1995]. In addition, the inner chloroplast model typically yields Q_a values smaller than ~0.5, except for very large cell sizes of >30 μm diameter. Reported experimental Q_a values considerably larger than 0.5 are not uncommon [Iturriaga & Sigel 1989, Ahn *et al.* 1992, Stephens 1995], and the inability of the inner chloroplast model to simulate large Q_a values at typical algal diameters of <30 μm diameter indicates that this geometry may be less suitable.

A further reason for adopting an outer chloroplast model geometry lies in the restrictions of a two-layered geometry – this precludes the specific assignation of a high refractive index external membrane or coating, structures shown to have considerable impact on backscattering [Meyer 1979, Bricaud *et al.* 1992, Zaneveld & Kitchen 1995]. Table 4.2 indicates similar real refractive index values of ~1.12-1.14 for chloroplasts and the various forms of external membrane or coating material (excluding the calcite coatings of coccolithophores which must be considered a special case). The intracellular refractive index gradient of the outer layer model will therefore be most similar to a hypothetical three layered model with an explicit peripheral membrane layer. In effect, the three layered model would simply have a thin peripheral layer outside the central chloroplast layer, of similar real refractive index and zero imaginary refractive index [Zaneveld & Kitchen 1995]. Differences in the scattering behaviour of the outer chloroplast two layer model and a hypothetical three layer model can reasonably be expected to be small, particularly in comparison to an inner chloroplast two layer model.

Examination of transmittance electron micrographs from morphometrical studies confirm that, for a wide variety of species, chloroplasts are located peripherally. These include a range of Diatom species [Hoops & Floyd 1979, Sicko-Goad & Stoermer 1979, Hitchcock 1982, Rosen & Lowe 1984, Janssen *et al.* 2001], Dinoflagellates with single [Highfill & Pfiester 1992, Jenks & Gibbs 2000] and many radial chloroplasts [Messer & Ben-Shaul 1972, Dodge & Crawford 1969, Spector & Triemer 1979], Pelagophytes [Gastrich *et al.* 1998, Pitcher *et al.* 1999], Chlorophytes [Rosen *et al.* 1986], Eustigmophytes [Fisher *et al.* 1998], and Cryptophytes [Thinh 1983]. There would thus seem evidence based on several forms of reasoning, and from a wide variety of sources, suggesting that an outer chloroplast geometry should be adopted for the remainder of this study.

4.4 Comparative Geometry and Causal Variability

Figure 4.1A and 4.1B show the typical oscillating behaviour with changing α of the attenuation and scattering efficiency factors [Van de Hulst 1957, Morel & Bricaud 1986]. Similar behaviour was noted by Aas [1984], and it can be seen that the outer layer model causes greater amplitude oscillations in both Q_c and Q_b, whilst tending to the same approximately constant values of Q_c=2 and Q_b=1 at large sizes [Morel & Bricaud 1986]. The behaviour of the Q_a values in Figure 4.1C have been discussed above – the behaviour displayed is again consistent with previous results [Morel & Bricaud 1981], in that the homogeneous and outer layer model produce similar results [Aas 1984]. The largest differences arising from heterogeneity can be seen in the enhanced backscattering efficiency Q_{bb} (Fig. 4.1D) and backscattering probability $\tilde{b}_b$ (Fig. 4.1F) values associated with the outer layer model. The Q_{bb} values of the outer layer model are between 5 and 25 times higher than the homogeneous model, converging to an approximately constant value at high sizes of $Q_{bb} \approx 0.0025 - 9$ times higher than the homogeneous model. Roughly the same comparisons hold for the backscattering probability factor values. It can be seen in both cases (Fig. 4.1D and 4.1F) that the somewhat chaotic structure in the backscattering vs size relationships [Morel & Bricaud 1986] is also appreciably different for the contrasting model geometries.

The effects of varying chloroplast size can be seen with regard to different means of comparison: heterogeneous cells of varying volume equivalence relative to homogeneous cells with a constant refractive index (Fig. 4.2), and homogeneous cells of varying volume equivalence relative to heterogeneous cells of constant m_{chlor} and m_{cyto} (Fig. 4.3). Changes in chloroplast size whilst maintaining volume equivalence have only small effects on attenuation, scattering, absorption and the package effect parameter (Figures 4.2A to 4.2C, and 4.2 E). However, more marked differences are observed if chloroplast size is adjusted without maintaining volume equivalence (Figures 4.3A to 4.3C, and 4.3 E)– not a surprising result as the bulk refractive indices of the cells will thus have changed considerably. The oscillation patterns in Q_c (Fig. 4.3A) and Q_b (Fig. 4.3B) show considerable difference in magnitude and peak position. Absorption is also affected, in

that the largest chloroplast cell displays Q_a values (Fig. 4.3C) and packaging (Fig. 4.3E) up to 50 % greater, concomitant with the increased bulk imaginary refractive index. It would thus appear that bulk refractive index changes are of much greater significance than morphological changes as concerns attenuation, total scattering and absorption parameters. These observations are consistent with the successful use of homogeneous Mie models to describe such parameters in the past [e.g. Bricaud & Morel 1986, Bricaud *et al.* 1988].

The converse appears to be true with regard to backscattering parameters from heterogeneous cells. Backscattering efficiency and probability factors of the heterogeneous volume equivalent cells (Fig. 4.2D and Fig. 4.2F) show considerable variability with changing chloroplast size and refractive index. Values of heterogeneous Q_{bb} and $\tilde{b}_b$ range from approximately 2 to 35 times higher than homogeneous values, with considerable dependence on α; somewhat chaotic at $\alpha<400$ and approximately constant thereafter. The approximately constant Q_{bb} values at high sizes ($\alpha>400$) can be used as a convenient comparison: these are 0.004 (Vv=15 %, n_{chlor}=1.18), 0.0025 (Vv=20 %, n_{chlor}=1.14), 0.0014 (Vv=30 %, n_{chlor}=1.10), and 0.00028 (homogeneous, n=1.044). In comparison, the heterogeneous cells with constant refractive indices (Figures 4.3 D and 4.3F) show markedly less relative variation in backscattering – whilst there are some differences in the oscillation patterns, the Q_{bb} values at $\alpha>400$ are approximately constant at 0.0025. It is interesting to note that the equivalent homogeneous cells with varying bulk refractive indices show significantly more variation, with the highest real refractive index cells displaying the highest backscattering values (Fig. 4.3D).These comparisons reveal not only that heterogeneous cells backscatter considerably more than their homogeneous equivalents, but behave in very different ways in response to refractive index changes. It would appear that the real refractive index of the outer chloroplast layer (or any peripheral layer) could be considered the single most important intracellular causal variable for backscattering; certainly more important than the relative size of the peripheral layer. Such conclusions are at least partially supported by previous heterogeneous modelling studies [Meyer 1979, Bricaud 1992, Zaneveld & Kitchen 1995].

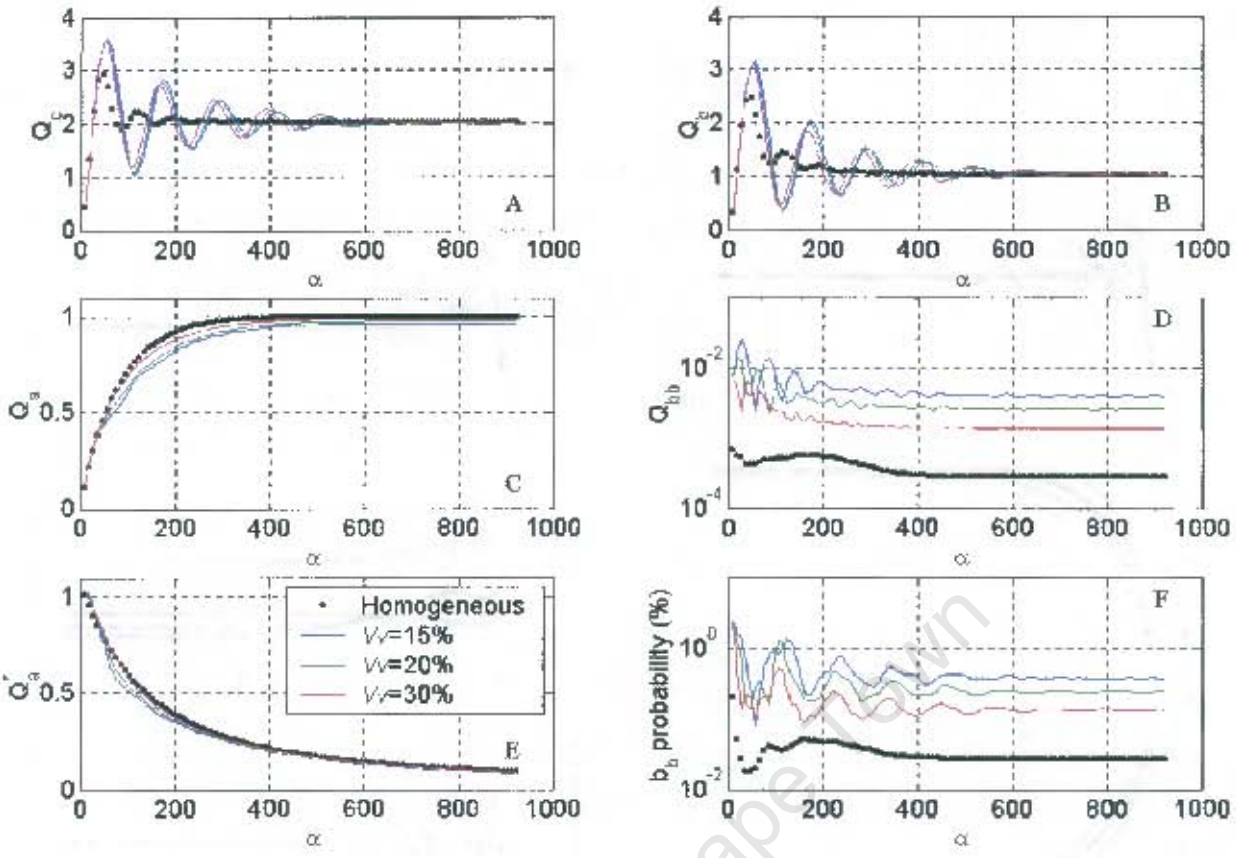

Figure 4.2 Optical efficiency factors and backscattering probability against Mie size parameter α for homogeneous spheres and heterogeneous spheres of varying relative chloroplast volume *Vv* and volume equivalent refractive indices. Relative chloroplast volumes are set to 15% (blue), 20% (green) and 30% (red). Homogenous spheres (dots) have a refractive index of m_h=1.044 - 0.0044*i*. Two-layered spheres (lines) with an outer chloroplast configuration have volume equivalent refractive indices of m_{cyto}=1.02 0.0005*i* and m_{chlor}=1.18 – 0.0265*i* (*Vv*=15 %), m_{chlor}=1.14 – 0.020*i* (*Vv*=20 %) and m_{chlor}=1.10 – 0.0135*i* (*Vv*=30 %).

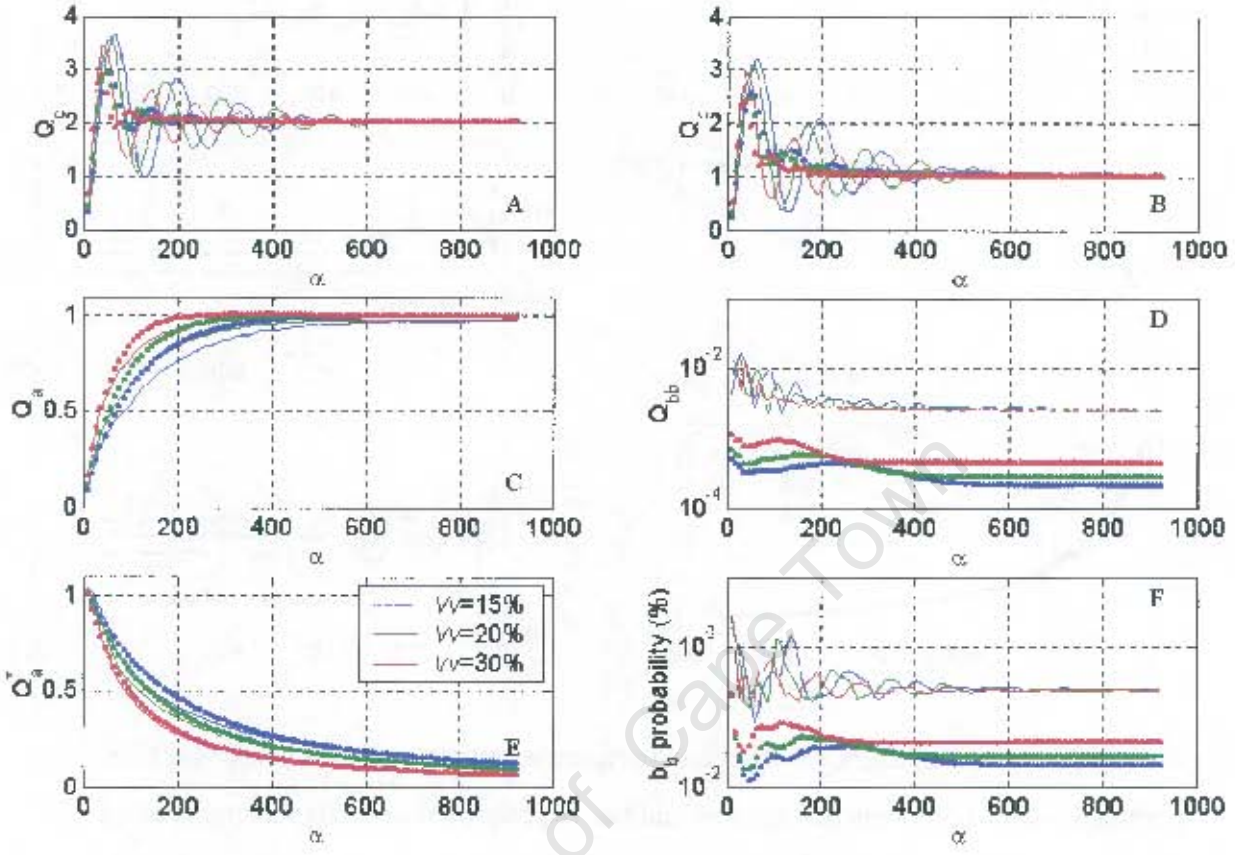

Figure 4.3 Optical efficiency factors and backscattering probability against Mie size parameter α for homogeneous spheres and heterogeneous spheres of varying relative chloroplast volume *Vv* and constant refractive index. Two-layered spheres (lines) with an outer chloroplast configuration have refractive indices of m_{chlor}=1.14 – 0.02*i* and m_{cyto}=1.02 – 0.0005*i*. Relative chloroplast volumes are set to 15% (blue), 20% (green) and 30% (red). Homogenous spheres (dots) have volume equivalent refractive indices of m_h=1.032 - 0.0024*i*, m_h=1.044 - 0.0044*i*, and m_h =1.056 - 0.0063*i* respectively. Note the log scales for the two backscattering related graphs.

The effects of variations solely in the imaginative refractive index are shown in Figure 4.4, where the value of n'_{chlor} is varied from 0.001 to 0.04. Resultant variations for Q_c (Fig. 4.4A) and Q_b (Fig. 4.4B) are consistent with the data of Morel & Bricaud [1986] – increases in the imaginary refractive index, responsible for absorption, result in damping of the typical oscillation patterns in these variables. Damping effects are observed for both homogeneous and heterogeneous geometries, although they appear more pronounced for the latter – perhaps due to the higher n'_{chlor} values relative to the homogeneous volume equivalent n'_h values. Geometry related effects on absorption (Fig. 4.4C) and the package effect parameter (Fig. 4.4E) are not pronounced for volume equivalent cells with a maximum difference of ~ 12 %. Again, the general increase in Q_a and decrease in Q_a^* with increasing n'_{chlor} are consistent with previous observations [Morel & Bricaud 1981, 1986].

Backscattering parameters for heterogeneous geometries appear to be affected in similar ways to total scattering – α related oscillations are more heavily dampened with increasing n'_{chlor} and become approximately constant at high α (Q_{bb}=0.0025 to 0.0027). Homogeneous backscattering with increasing α displays a different structure; a pronounced backscattering maxima at α=200 to 300, which disappears with increasing n'_h values – a phenomenon that has been observed previously [Morel & Bricaud 1986]. Of particular importance are the considerably elevated backscattering values at very low imaginary refractive index values; the potential effects of this will be discussed later with regard to spectral backscattering characteristics.

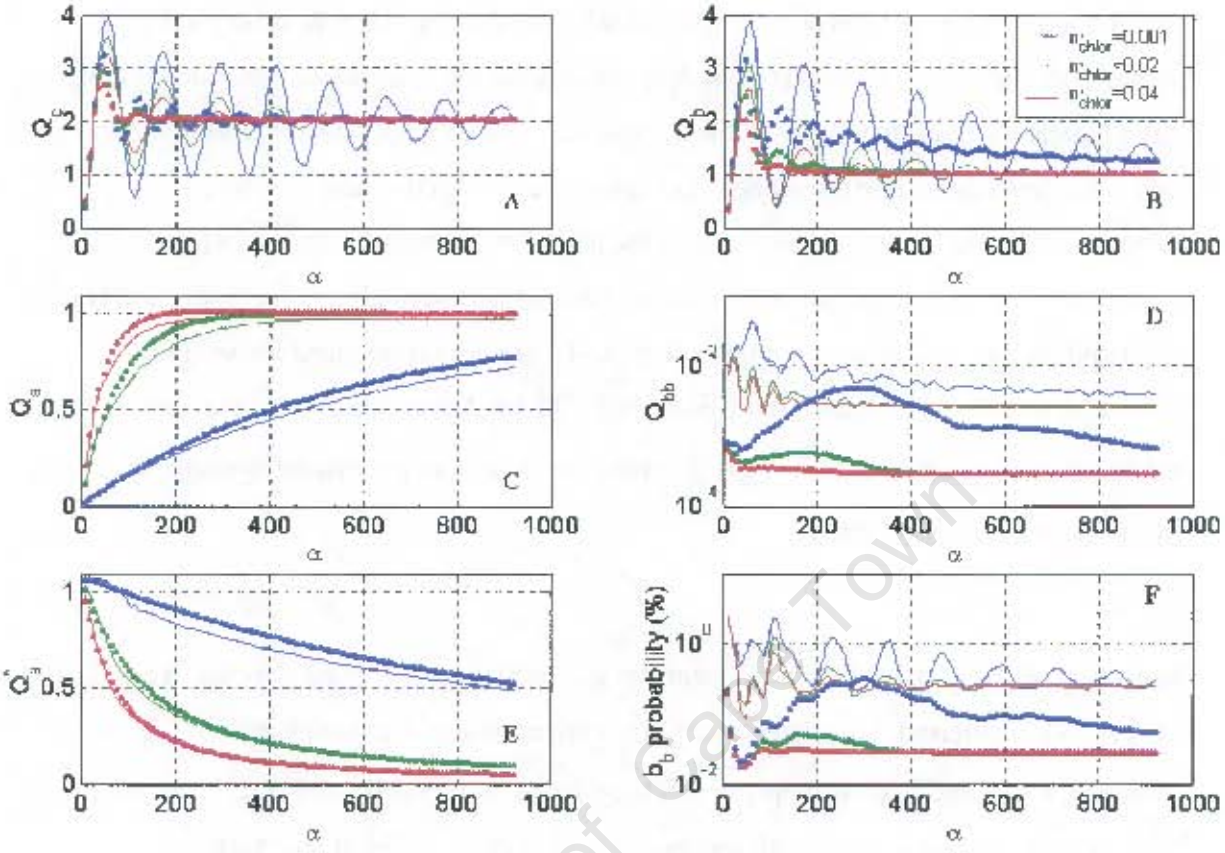

Figure 4.4 Optical efficiency factors and backscattering probability against Mie size parameter α for two-layered spheres with varying imaginary part of the chloroplast refractive index. Two-layered spheres (lines) with an outer chloroplast configuration have refractive indices of m_{cyto}=1.02 – 0.0005i , n_{chlor}=1.14, and n'_{chlor} values of 0.001 (blue), 0.02 (green) and 0.04 (red). Homogeneous spheres (dots) have volume equivalent refractive indices of m_h=1.044 - 0.0006i, m_h=1.044 - 0.0044i, and m_h=1.044 - 0.0084i respectively. Relative chloroplast volume is set to 20%. Note the log scales for the two backscattering related graphs.

The effects of variations in polydispersity can be seen in Figure 4.5, displaying data for single sizes and Standard distributions [Hansen & Travis 1974, Chapter 2] of differing effective variance (or width). The Q_c (Fig. 4.5A) and Q_b (Fig. 4.5B) data are consistent with the finding of Morel & Bricaud [1986] – increased polydispersion results in greater damping of the oscillation patterns in these variables, leaving only the first oscillation peak at $\alpha \approx 60$ still prominent. Absorption would appear to be affected primarily by the inclusion of smaller sizes as polydispersion increases, with Q_a values at $v_{eff} \sim 0.6$ up to 15 % lower than the monodispersed values (Fig. 4.5C) – package effect parameter values are consistent with this (Fig. 4.5E). Geometry related variability remains small, with maximal 10 % differences between homogeneous and heterogeneous absorption. The effects on polydispersity on backscattering are consistent with previous studies [Morel & Bricaud 1986] – the finer scale chaotic behaviour in both Q_{bb} (Fig. 4.5D) and $\bar{b}_b$ (Fig. 4.5F) are smoothed. Increased polydispersity leads to slightly higher backscattering values at large sizes due to the greater inclusion of smaller particles in the size distribution. It can also be seen that very low imaginary refractive index values lead to profound changes in selected optical properties – these will be discussed later with regard to the spectral nature of modelled inherent optical properties.

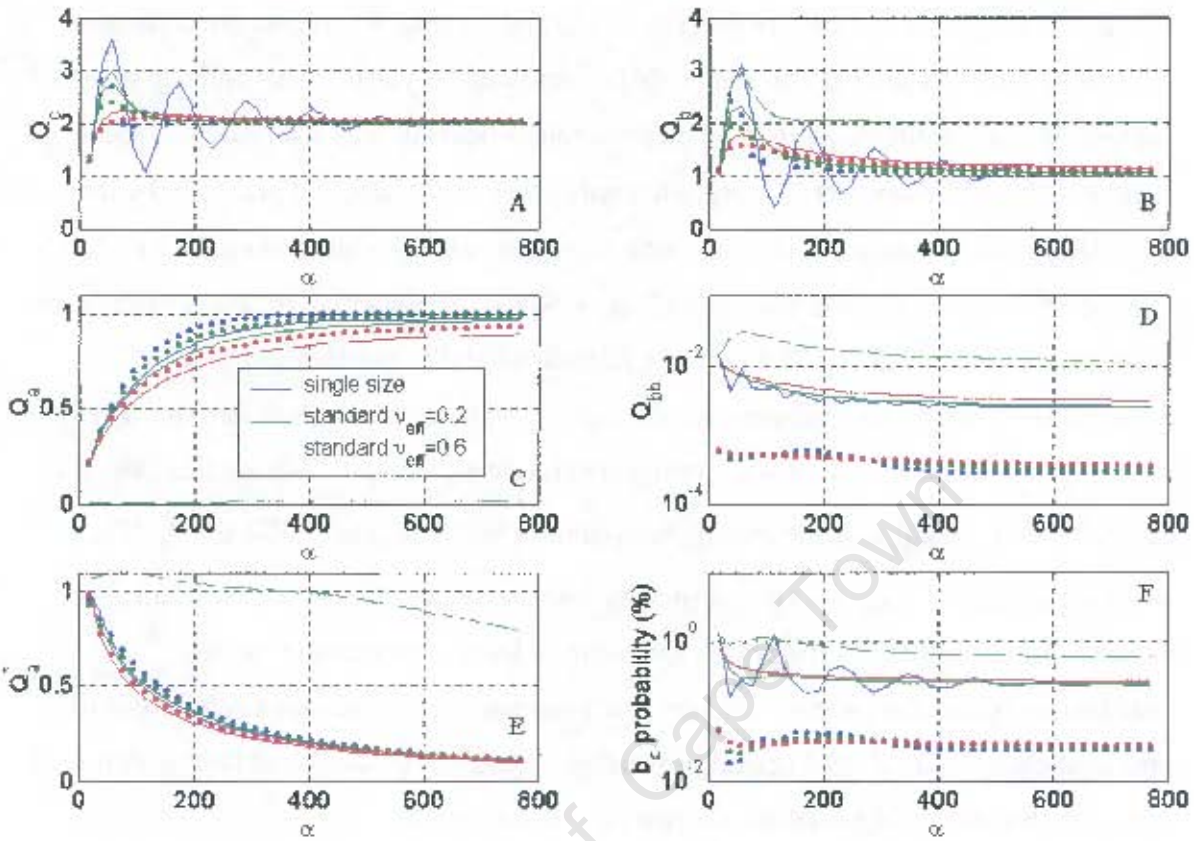

Figure 4.5 Optical efficiency factors and backscattering probability against Mie size parameter α for size distributions of two-layered spheres with varying polydispersity. Two-layered spheres (lines) with an outer chloroplast configuration have refractive indices of m_{cyto}=1.02 – 0.0005i , and m_{chlor}=1.14 - 0.02i. Homogenous spheres (dots) have volume equivalent refractive indices of m_h=1.044 - 0.0044i. Relative chloroplast volume is set to 20%. Data are shown for a single size (blue), a narrow Standard size distribution with v_{eff}=0.2, and a wide Standard size distribution with v_{eff}=0.6. Note the log scales for the two backscattering related graphs, and the α scale of 1 to 800. The green dashed lined represents a Standard size distribution of two-layered spheres with v_{eff}=0.2, m_{cyto}=1.02 – $10^{-5}i$, and m_{chlor}=1.14 – $10^{-5}i$, and demonstrates the effects of low imaginary refractive index in both chloroplast and cytoplasm.

4.5 Comparative Geometry and Spectral Inherent Optical Properties

4.5.1 Determination of Refractive Indices for Algal Populations

Modelling the full spectral inherent optical properties of an algal population requires the derivation of the refractive index spectra; either $m_h(\lambda)$ for homogeneous cells, or $m_{chlor}(\lambda)$ and $m_{cyto}(\lambda)$ for two-layered cells. Measurements of phytoplankton absorption and size distributions allow the calculation of experimental absorption efficiency factors using Equation 4.13 [Bricaud & Morel 1986, Stramski *et al.* 1988]. From these data the imaginary refractive index, and the spectral shape of the real refractive index, can be determined (as discussed previously) for both homogeneous cells and the layers of heterogeneous cells. The real refractive index spectra $n(\lambda)$, of either the homogeneous cell or its constituent layers, can then be calculated using Equation 4.14, through the selection of appropriate $1-\varepsilon$ values.

It is possible to make direct determinations of $1-\varepsilon$ values for homogeneous cells through the ADA – this would require additional use of attenuation or scattering data, not available to this study [Bricaud & Morel 1986, Stramksi *et al.* 1988]. Even if such data were available, it would be extremely difficult to determine real and imaginary refractive index spectra for both chloroplast and cytoplasm from optical and size measurements. The ADA, allowing the decoupling of the real and imaginary refractive index, is typically used for such purposes as an iterative inverse efficiency factor model for homogeneous cells [*ibid.*]. Whilst an ADA formulation is available for a two-layered geometry [Quirantes & Bernard 2004], it is unlikely to satisfy the original ADA assumption that the real refractive index is small (m-1<<1) [Van de Hulst 1957], given the high chloroplast refractive indices suggested by Table 4.2. Two-layered application of the iterative modelling approach to refractive index determination of Stramski [1988] would thus require invocation of the full Aden-Kerker formulae, dealing with the four unknowns of real and imaginary refractive index for both layers. Such a model was constructed and applied to sample data from Bricaud *et al.* [1988]. The results (not presented here) indicate that multiple solutions abound even with very close matches for absorption and attenuation data, i.e. *a priori* assumptions concerning the spectral refractive indices of

layers must be made to return feasible model solutions. The dependence of the study upon $1+\varepsilon$ values gleaned from the literature, most specifically for simulated chloroplasts, is thus not inappropriate.

Preliminary two-layered modelling efforts also indicated the need for assumed refractive index values of the cytoplasm. Based on the intracellular optical efficiency measurements of Stephens [1995], the typical exponential spectral shape of organic detrital particles [Ituriaga & Siegel 1989], and trial modelling runs, the imaginary refractive index for cytoplasm was chosen to be:

$$n'_{cyto}(\lambda) = n'_{cyto}(400)\exp[-0.01(\lambda - 400)] \qquad (4.22)$$

where $n'_{cyto}(400)=0.0005$. Real refractive index spectra for the cytoplasm $n_{cyto}(\lambda)$ were then generated with a Hilbert transform under Matlab R13 (The MathWorks), and Equation 4.14 with $1+\varepsilon=1.02$.

Given such considerations, refractive index spectra for sample natural algal populations have therefore been determined in three different ways. To generate initial values for homogeneous cells, $n'_h(\lambda)$ spectra were calculated using the ADA (Equation 4.15) [Stramski *et al.* 1988]. Using the $n'_{cyto}(\lambda)$ values of Equation 4.22, volume equivalent $n'_{chlor}(\lambda)$ values were determined using the Gladstone-Dale formulation given by:

$$n'_{chlor}(\lambda) = (n'_h(\lambda) - n'_{cyto}(\lambda)Vv)/(1-Vv) \qquad (4.23)$$

where Vv is the chloroplast volume. Real refractive index spectra for the chloroplast $n_{chlor}(\lambda)$ were then similarly generated with a Hilbert transform, and Equation 4.14 with assumed $1+\varepsilon$ values as discussed below.

In addition to the volume equivalent generation of $n'_{chlor}(\lambda)$, a further method based on direct application of the Aden-Kerker formulae was employed, designed to provide

greater accuracy of refractive index determination. Using the volume equivalent m_{chlor} and m_{cyto} values just described as initial input, a non-linear solution of Equation 4.11 was implemented, employing a simplex routine [Nelder & Mead 1965] and the Toon & Ackerman [1981] code. Solving for experimental Q_a values with measured size distributions, the model was allowed several passes through the entire wavelength range to yield $n'_{chlor}(\lambda)$ and $n_{chlor}(\lambda)$ values consistent with Aden-Kerker theory and the Kramers-Kronig relations, with $m_{cyto}(\lambda)$ held constant.

Sample absorption and size distribution data from natural algal assemblages in the southern Benguela are used as input to the refractive index models (Appendix II). Briefly, particulate and detrital absorption data were measured with the quantitative filter pad technique [Yentsch 1962, Roesler 1998, Kishino *et al.* 1985] using a Shimadzu UV-2501 spectrophotometer equipped with an ISR-2200 internal integrating sphere. Phytoplankton absorption $a_\phi(\lambda)$ data were then obtained by subtraction of detrital absorption $a_d(\lambda)$from total particulate absorption $a_p(\lambda)$. Particle size measurements were made using a 128 channel Coulter Multisizer II with a 140 µm aperture in manometer mode, using freshly prepared 0.2 µm filtered seawater as both blank and electrolyte. Numerical techniques [Chapter 2] were employed to fractionate measured size distributions into algal and non-algal components, and extend both lower and upper ranges of measured size distributions to match absorption measurements. Pigments were analysed using High Performance Liquid Chromatography (HPLC) using the methods of [Barlow *et al.* 1997]. Detailed methods for all measurements are presented in Chapter 2.

Four assemblages types common to upwelling systems [Hutchings *et al.* 1994] were chosen for detailed analysis. These are: an offshore assemblage dominated by small Chlorophytes and Prymnesiophytes (*flagellate*, d_{eff}=4.32 µm, Chl a=0.59 mg m^{-3}, c_i=1.5 kg m^{-3}), a diatom dominated assemblage (*diatom*, d_{eff}=8.3 µm, Chl a=6.1 mg m^{-3}, c_i=2.3 kg m^{-3}), an assemblage dominated by the dinoflagellates *Alexandrium catenella* and *Ceratium* spp. (*dinoflagellate*, d_{eff}=26 µm, Chl a=126 mg m^{-3}, c_i=4.0 kg m^{-3}), and a mixed assemblage of diatoms and the Cryptophyte endosymbiont containing ciliate *Mesodinium rubrum* (*cryptophyte*, d_{eff}=14 µm, Chl a=195 mg m^{-3}, c_i=3.1 kg m^{-3}).

Dominant accessory pigments for these samples are: chlorophyll c-chlorophyll *b*-fucoxanthin derivatives (*flagellate*), chlorophyll *c*-fucoxanthin-diadinoxanthin (*diatom*), chlorophyll *c* peridinin-diadinoxanthin (*dinoflagellate*), and chlorophyll *c* – alloxanthin (*cryptophyte*).

The measured and derived refractive index data for the four example assemblages are shown in Figure 4.6. Measured Chl *a*-specific phytoplankton absorption (Fig. 4.6A) show the effects of size related packaging, most obvious when comparing the *flagellate* and *dinoflagellate* samples, dominated by small and large cells respectively. The effects of differences in accessory pigment complements can also be seen, most prominently in the phycoerythrin affected *cryptophyte* sample [Gustafson 2000]. Chl *a*-normalised volume size distributions show the typically highly polydispersed nature of natural algal assemblages, even in high biomass bloom situations, particularly so for the *crytophyte* sample, which is composed of small celled diatoms and the large celled *Mesodinium rubrum*.

Modelled absorption efficiency factor data used for the direct two-layered refractive index determinations show a very close match (Fig. 4.6C) to experimental determined Q_a values, indicating the successful simulation of the heterogeneous model. It should be noted that the two-layered refractive index model utilising the Aden-Kerker code was unable to produce appropriately smooth n'_{chlor} values when using the default Vv value of 20 % for the large celled *dinoflagellate* and *crytophyte* samples. Appropriately shaped n'_{chlor} spectra (i.e. those without significant spikes) were only obtained when minimal Vv values of 30 % were adopted for these two samples. It would appear that this is due to the high experimental Q_a values for these samples (Fig. 4.6C), and the relatively higher Q_a values theoretically possible when higher Vv values are adopted (Figures 4.2C and 4.3C). Relatively high Q_a values are associated with high values of either of the two variables causal to absorption – cell diameter d_{eff} or intracellular Chl *a* concentration c_i [Morel & Bricaud 1981, Bricaud *et al.* 1988, Ahn *et al.* 1992]. Consistent with this, the two samples requiring larger Vv values of 30 % (*dinoflagellate* and *crytophyte*) display higher d_{eff} and c_i values than the two samples that can be modelled with Vv values of 20 %

(*flagellate* and *diatom*). Further comment on the relationship between chloroplast size and absorption in the context of general algal morphometrics and physiology is considered beyond the scope of this study. To facilitate comparison between assemblages the real refractive indices of the two samples with forced *Vv* values of 30 % were adjusted to maintain a constant homogeneous volume equivalent 1+ε of 1.044 – n_{chlor} values for the *dinoflagellate* and *crytophyte* samples thus use 1+ε=1.10 as opposed to 1+ε=1.14 for *flagellate* and *diatom* samples

A final comment of the refractive index determinations can be made with regard to the use of volume equivalent determinations. Figure 4.6E displays the n'_{chlor} values calculated both from volume equivalence with homogeneous n'_h values, and those determined directly using Aden-Kerker theory. In the majority of cases the agreement between the two methods is good, with under 10 % difference. The exceptions are at the Soret peak of the *crytophyte* and *dinoflagellate* samples, where differences of ~ 15 % and ~25 % are observed. It should be remembered that the n'_h are calculated with the ADA, known to give errors of ~ 10% in comparison to Mie theory [Latimer 1984, Geider & Osborne 1987], and some discrepancies can therefore be expected between ADA and Aden-Kerker derived values. The general agreement between volume equivalent derived imaginary refractive index values and those derived from exact theory are consistent with previous discussion indicating the effects of cell heterogeneity are relatively small on absorption. It would thus seem reasonable to employ the more easily derived volume equivalent refractive index values for general cases, perhaps excepting very highly packaged cells such as the *dinoflagellate* sample.

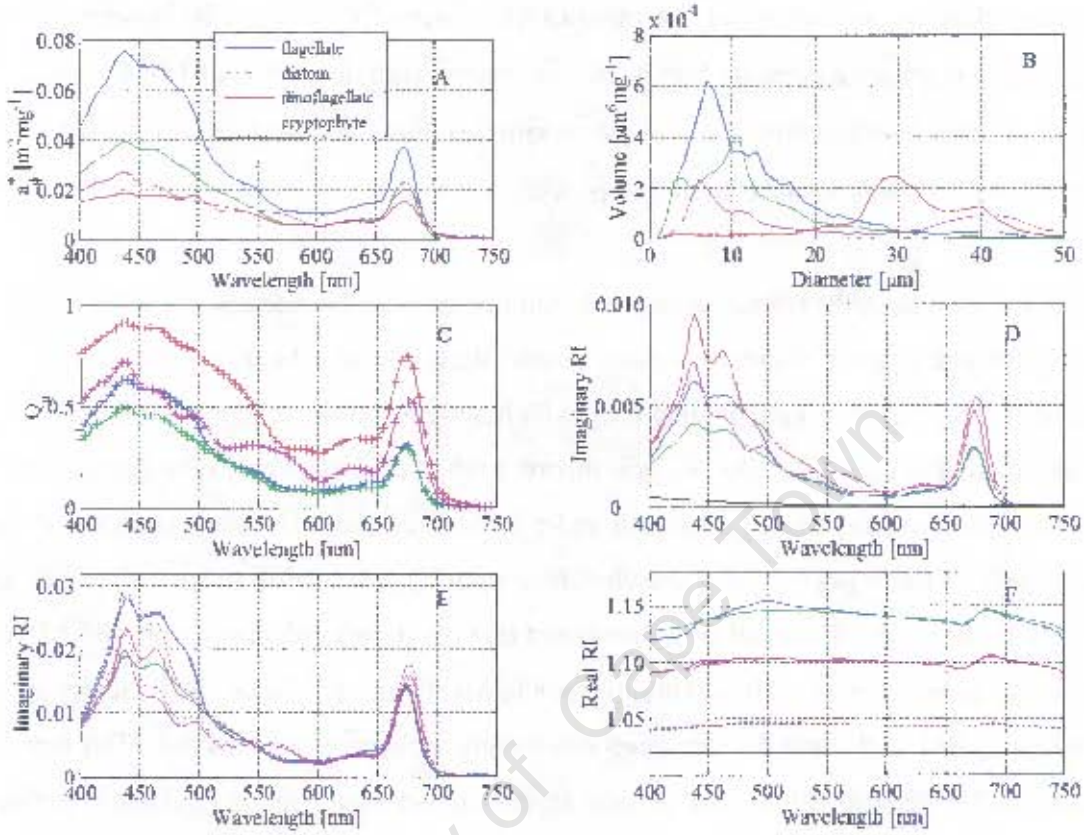

Figure 4.6. Optical and size data for four sample algal assemblages. A) Chl *a*-specific phytoplanton absorption, B) Chl *a* specific cellular volume distributions, C) experimental (line) and two layer model values (-) for absorption efficiency factors, D) imaginary refractive indices for homogeneous cells $n'_h(\lambda)$ and for cellular cytoplasm $n'_{cyto}(\lambda)$ (black line), E) imaginary refractive indices for chloroplasts $n'_{chlor}(\lambda)$, determined with the inverse Aden-Kerker model (solid line) and from homogeneous values with volume equivalence (dashed lines), F) real refractive indices for chloroplasts $n_{chlor}(\lambda)$ (solid lines), and volume equivalent homogeneous cells (dashed lines). Note that larger Vv values of 30 % were required for successful two-layered Q_a simulation for the two assemblages dominated by larger cells; the *dinoflagellate* and *cryptophyte* samples.

Based on the Aden-Kerker derived refractive index spectra and measured algal size distributions for the four sample assemblages, the same code was used to determine a range of simulated efficiency factors and inherent optical properties for two-layered and volume equivalent homogeneous geometries.

4.5.2 Modelled Optical Efficiency Factors

Mean optical efficiency factors are detailed in Figure 4.7. Consistent with Figure 4.2, it appears that geometry related differences in attenuation, total scattering and absorption are relatively small. Absorption appears to be least affected by geometry changes – heterogeneous cells produce slightly lower absorption values with a maximum 10 % difference and little change in spectral shape (Fig. 4.7C). Attenuation differences are slightly more pronounced (Fig.4.7A), with changes in spectral shape with geometry most noticeable for large cell assemblages – the two-layered geometry Q_c values appear to display greater spectral variability than their homogeneous counterparts. Maximum differences for Q_c values occur at red wavelengths and are ~ 15 % - in all cases apart from the far red values for the *dinoflagellate* sample, the two-layered values are higher. Of the three non-angular efficiency factors, geometry related differences in scattering are most pronounced (Figures 4.7B and 4.7E) – two-layered Q_b values are ~ 15 % higher in most cases, with the most pronounced spectral differences observed for the *dinoflagellate* sample. In all cases the magnitude and spectral shape of the Q_c, Q_b, and Q_a spectra displayed in Figure 4.7 are consistent with analogous published experimental data for algal cultures [Bricaud *et al.* 1988, Ahn *et al.* 1992].

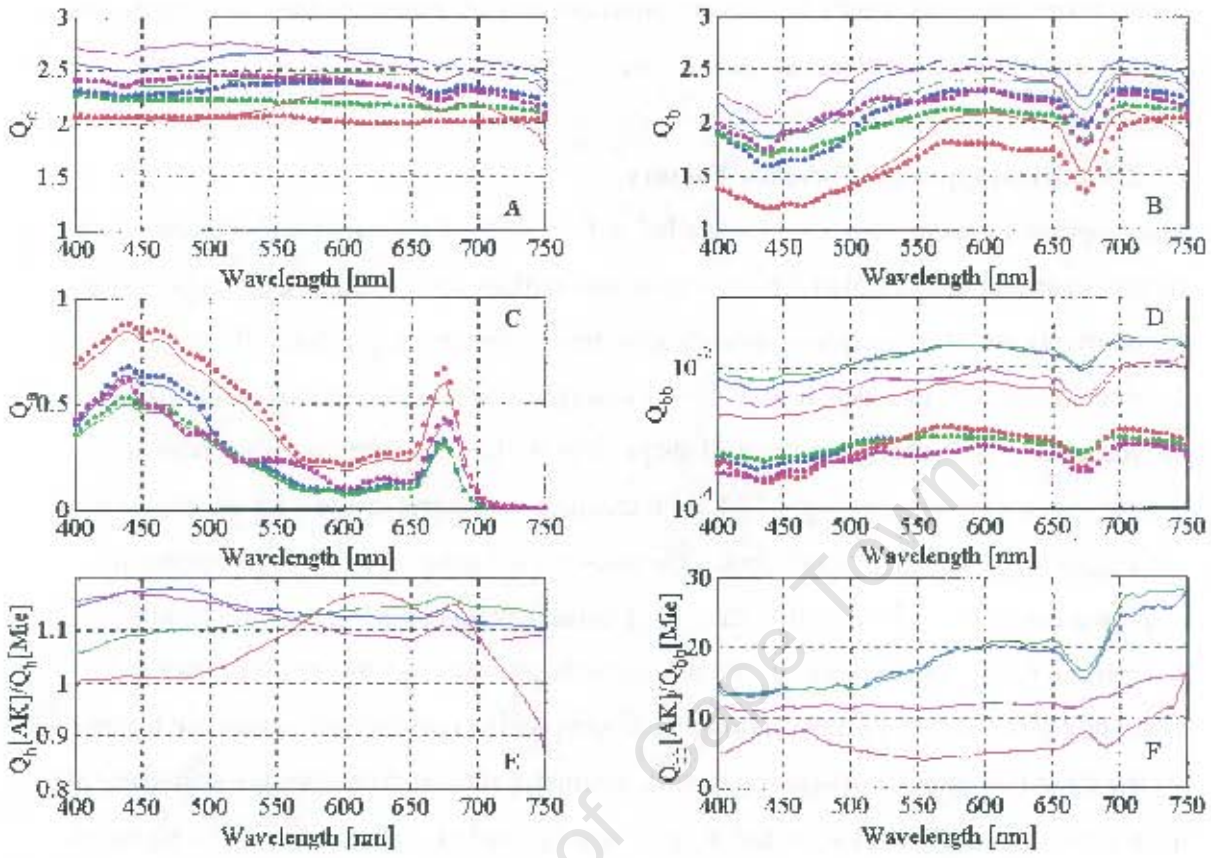

Figure 4.7 Optical efficiency factors for the four sample algal assemblages. Legend colours are as for the previous figure, for data from the two-layered geometry (lines) and homogeneous geometry (dots). A) attenuation efficiency factors Q_c, B) scattering efficiency factors Q_b, C) absorption efficiency factors Q_a, D) backscattering efficiency factors Q_{bb}, E) ratio of Q_b for two-layered and homogeneous gemoetries, F) ratio of Q_{bb} for two-layered and homogeneous gemoetries. Homogeneous refractive indices are calculated from volume equivalence to the two-layered data to facilitate comparison.

The geometry related effects for attenuation, scattering and absorption are very small in comparison to those observed for backscattering. Two-layered backscattering values range from ~500 % to ~2500 % higher than equivalent homogeneous values, with considerable differences in spectral shape (Figures 4.7D and 4.7F). Two-layered Q_{bb} values range from ~0.002 to ~ 0.026, in comparison to homogeneous Q_{bb} values of ~0.0002 to 0.0014. The two-layered Q_{bb} values compare well with measured Q_{bb} values for a range of algal cultures of ~0.003 to ~0.039 [Vaillancourt *et al.* 2004], indicating that the large increases in backscattering associated with heterogeneity are appropriate. The backscattering spectra display considerable variability with wavelength, with consistent depressions located at very slightly shorter wavelengths than the Soret and red Chl *a* absorption peaks - such features are consistent with the effects of anomalous dispersion [Van de Hulst 1957, Bricaud *et al.* 1983, Zaneveld & Kitchen 1995].

Further assemblage-specific anomalous dispersion effects can be seen in the depressions at ~ 495 nm and ~550 nm in the *cryptophyte* sample, which correspond with the unusually distinct absorption bands at these wavelengths for this assemblage. All algal backscattering spectra display their highest values at red wavelengths, with broad secondary maxima at ~ 600 nm – the region where algae typically display absorption minima (e.g. Fig. 4.7C). These anomalous dispersion effects are not always seen in measured Q_{bb} values for algal cultures [Vaillancourt *et al.* 2004] – the reasons for this would appear to lie in the assumptions made in backscattering derivations from specific instrument systems.

The varying magnitude of the Q_{bb} spectra (Fig. 4.7D) are consistent with both the size effects (4.5D) and the real refractive index effects (Fig. 4.2D) discussed previously – the two small celled samples with central values of n_{chlor}=1.14 (*flagellate* and *diatom*) display backscattering efficiencies 2 to 3 times higher than larger celled samples with central values of n_{chlor} =1.10 (*dinoflagellate* and *cryptophyte*). The decoupled effects of these variables on heterogeneous backscattering will be discussed in more detail below.

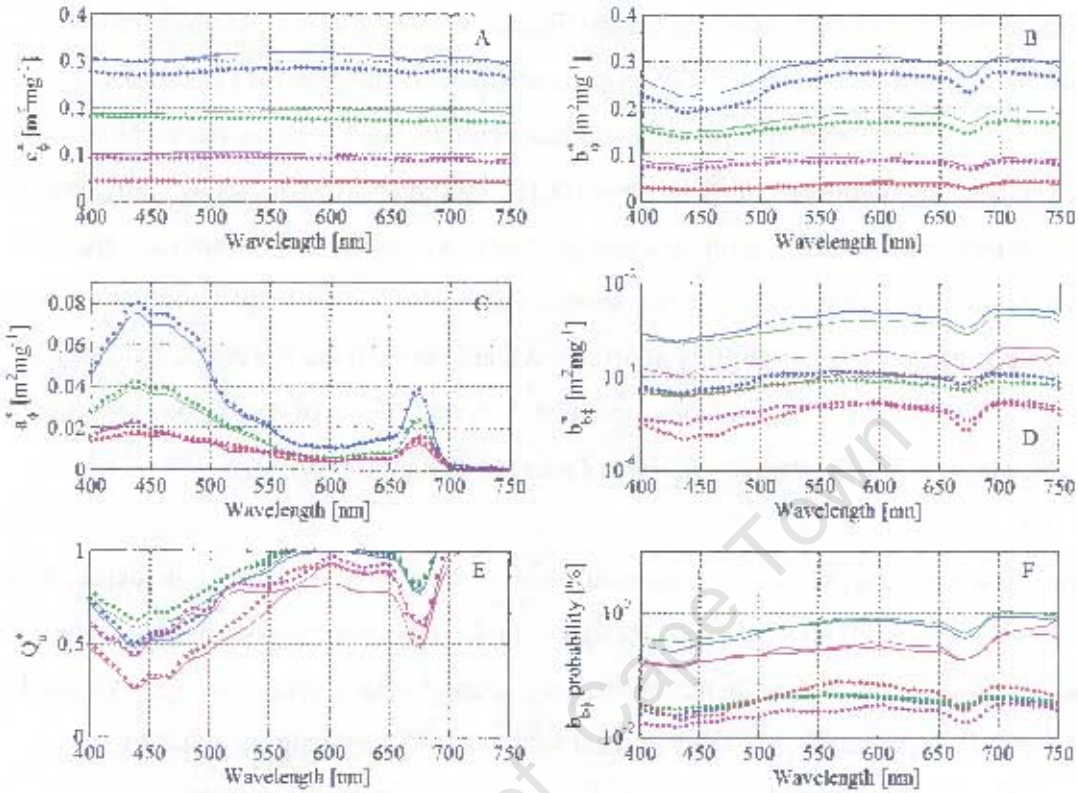

Figure 4.8 Chl *a*-specific inherent optical properties, package effect parameter and backscattering probability data for the four sample algal assemblages. Legend colours are as for the previous figure, for data from the two-layered geometry (lines) and homogeneous geometry (dots). A) Chl *a*-specific attenuation coefficient $c_\phi^*(\lambda)$, B) Chl *a*-specific scattering coefficient $b_\phi^*(\lambda)$, C) Chl *a*-specific absorption coefficient $a_\phi^*(\lambda)$, D) Chl *a*-specific backscattering coefficient $b_{b\phi}^*(\lambda)$, E) package effect parameter $Q_a^*(\lambda)$, F) Algal backscattering probability factor $\tilde{b}_{b\phi}(\lambda)$. Homogeneous refractive indices are calculated from volume equivalence to the two-layered data to facilitate comparison.

4.5.3 Modelled Inherent Optical Properties

Chl *a*-specific inherent optical properties and package effect parameter data for the four example assemblages can be seen in Figure 4.8. The magnitude and spectral shape of the attenuation (Fig. 4.8A) and scattering (Fig.4.8B) values are again consistent with previously published values for algal cultures [Bricaud *et al.* 1988, Ahn *et al.* 1992]. Geometry related differences for attenuation, scattering absorption and backscattering are equivalent to those discussed above with regard to efficiency factors. Adopting a two-layered geometry results in slightly greater packaging (Fig.4.8E) for all samples with maximum differences of ~ 10 % - the *dinoflagellate* sample is the most affected, as might be expected considering the relatively high d_{eff} and c_i values of this assemblage.

Chl *a*-specific backscattering values for the two-layered geometry range from ~2.0×10^{-3} to ~1×10^{-4} m^2 mg^{-1} at 550 nm, as compared to homogeneous values ~13×10^{-4} to ~2×10^{-5} m^2 mg^{-1} at the same wavelength. These can be be compared to measured ranges of ~1.0×10^{-3} to ~2×10^{-5} m^2 mg^{-1} at 550 nm [Ahn *et al.* 1992], the mean value of 9×10^{-4} m^2 mg^{-1} at 510 nm [Vaillancourt *et al.* 2004], and a measured valued for *Trichodesmium* spp. of 2.0×10^{-3} m^2 mg^{-1} at 550 nm [Subramaniam *et al.* 1999]. With the caveat that such coarse range comparisons are useful only to first order, and there are observed discrepancies with the data of Ahn *et al.* [1992], the comparable values of the higher two-layered values generated here and the experimental values indicates appropriate input and structure with regard to the heterogeneous model.

Modelled backscattering probability data (Fig.4.8F) show equivalent geometry related differences to those discussed with regard to Figure 4.7. Backscattering probability values range from ~0.2 % to ~1 % for the two-layered geometry, as compared to ~0.02 % to ~0.08 % for homogeneous particles. Such values can be compared to values determined experimentally of ~0.01 to ~0.4 % [Bricaud *et al.* 1983, Ahn *et al.* 1992], those determined through combined experiment and radiative transfer modelling of ~0.2 % to ~1.5 % [Stramski & Piskozub 2003], and those predicted by Mie theory of a maximum of ~0.2 % [Bricaud *et al.* 1983, Morel & Bricaud 1986, Morel 1988]. Whilst the homogeneous $\tilde{b}_b$ values generated here compare well with previous theoretical value

ranges [*ibid.*], the comparisons with published data are somewhat equivocal. Nevertheless, the $\tilde{b}_b$ data shown here indicate that adopting a viable heterogeneous geometry produces considerably higher backscattering probabilities than homogeneous equivalents, and the observed $\tilde{b}_b$ range of up to 1 % is consistent with experimental observation [Stramski & Piskozub 2003].

4.5.4 Size and Assemblage Dependent Inherent Optical Properties

The assemblage-specific refractive index spectra and morphometric data can be used, in combination with the Standard size distributions outlined in Chapter 2, to calculate the optical properties of hypothetical polydispersed algal populations. This gives the ability to assess the optical effects of variability in key intracellular parameters: the imaginary and real refractive indices, and chloroplast morphology. In addition, such an approach also allows a greater understanding of the effects of changing mean assemblage size, as given by the effective diameter. Whilst such relationships are well understood as regards algal absorption, they are poorly understood with regard to algal backscattering, particularly so from the perspective of a heterogeneous geometry. An improved understanding of how backscattering varies with both assemblage type and size is extremely important to HAB related bio-optical observations and inversion techniques.

A Chl *a*-specific size distribution for a hypothetical algal population can be calculated based on three variables: the effective diameter d_{eff}, the effective variance v_{eff} and the intracellular Chl *a* concentration c_i. A Standard size distribution $F(d)$ for a range of particle sizes given by diameter d is expressed as [Hansen & Travis 1974]:

$$F(d) = ASF\left(\frac{d}{2}\right)^{\left\{(1-3v_{eff})/v_{eff}\right\}} \exp\left[\left(\frac{d}{2}\right)\Big/\left(\frac{d_{eff}}{2}v_{eff}\right)\right] \qquad (4.25)$$

where ASF can be treated as an arbitrary scaling parameter at this stage. The total relative particle volume $\bar{V}$ of this distribution can then be calculated with:

$$\bar{V} = \frac{\pi}{6} \int F(d) d^3 d(d) \tag{4.26}$$

and the initial distribution $F(d)$ scaled to Chl a-specific $F^*(d)$ with:

$$F^*(d) = \frac{F(d)}{\bar{V} c_i} \tag{4.27}$$

The $F^*(d)$ values can then be used with the Aden–Kerker derived refractive indices discussed in Section 4.5.1, with the additional use of Equation 4.21 to ensure that the chloroplast refractive index data are consistent with the c_i value employed. With this approach IOPs have been generated for hypothetical diatom and dinoflagellate populations with d_{eff} varying from 2 µm to 64 µm. Refractive index spectra from the *diatom* and *dinoflagellate* example assemblages analysed previously have been used, in combination with the measured c_i values for these assemblages of 2.3 kg m^{-3} and 4.0 kg m^{-3} respectively. Diatom simulations employed Vv =20 % and n_{chlor}=1.14 values, whilst dinoflagellate simulations employed Vv =30 % and n_{chlor}=1.10 values, as deduced for the original example assemblages. Cytoplasm refractive index are as used previously.

It must be appreciated that the use of constant refractive index and morphological data across a wide range of algal sizes is a first approximatation. In reality, size and assemblage related variability will be considerably more complex, due to issues such as the non-scalability of certain intracellular membranes [Raven 1986], photoadaptive, taxon, and trophic state induced morphological variability (Table 4.1), and c_i and resultant real and imaginary refractive index variability [Bricaud *et al.* 1988], amongst others. The use of a single chloroplast refractive index spectra as representative of a group such as the dinoflagellates across a wide range of cell sizes is also very much a simplification, as the relative concentration and occurrence of accessory pigments will obviously vary considerably in nature. In addition the real refractive index of the chloroplast, kept at a constant central value for each assemblage across the size range, is likely to show variability [Bricaud *et al.* 1988, Ahn *et al.* 1992]. Nevertheless, as a

preliminary means of enhancing understanding of the optical variability of algal populations, the approach is of considerable use. Diatoms and dinoflagellates are chosen as examples due to the occurrence of these algal groups across a wide range of sizes [Table 4.1, Bricaud *et al.* 1988, Ahn *et al.* 1992]. It should be realized that the refractive index spectra employed for these groups are representative of the measured accessory pigment suite - the dinoflagellates are thus considered representative only of those species containing peridinin dominated pigment protein complexes.

Figure 4.9 details the Chl *a*-specific inherent optical properties of simulated diatom dominated populations of effective diameters from 2 μm to 64 μm. The changing shape of the attenuation coefficient $c_\rho^*(\lambda)$ with size (Fig. 4.9A) is of considerable interest: it has been used previously for refractive index determinations [Bricaud & Morel 1986, Twardowski *et al.* 2001], and to establish estimates of particle size distribution parameters [Boss *et al.* 2001, Roesler & Boss 2003]. Three broad types of spectral shape in $c_\rho^*(\lambda)$ can be distinguished (Fig. 4.9A): 1) decreasing $c_\rho^*(\lambda)$ with λ for small cell sizes (d_{eff}=2 and 4 μm), 2) increasing $c_\rho^*(\lambda)$ with λ for intermediate cell sizes (d_{eff}=8 and 16 μm), and 3) approximately constant $c_\rho^*(\lambda)$ for larger cell sizes (d_{eff}=32 and 64 μm) [Bricaud *et al.* 1986]. Such observations are not entirely consistent with studies employing numerical relationships between the attenuation and Junge slopes to describe the particle size distribution [Boss *et al.* 2001, Twardowski *et al.* 2001], which cannot display the second case of spectral shape above. However, such studies have been concerned with total particulate as opposed to the viable algal particulate [*ibid.*], and the inconsistency is at least in part due to this. Otherwise the changing slope and magnitude of the $c_\rho^*(\lambda)$ spectra with size are entirely consistent with both measurement and theory [Bricaud & Morel 1986, Bricaud *et al.* 1988]. Again, geometry related differences in the attenuation spectra are small (< 15 %), and adoption of a two-layered geometry does not appear to impact upon the spectral shape considerations discussed above. Similar considerations hold for the scattering $b_\rho^*(\lambda)$ spectra (Fig. 4.9B), which are also consistent in shape and magnitude with previous observations [*ibid.*].

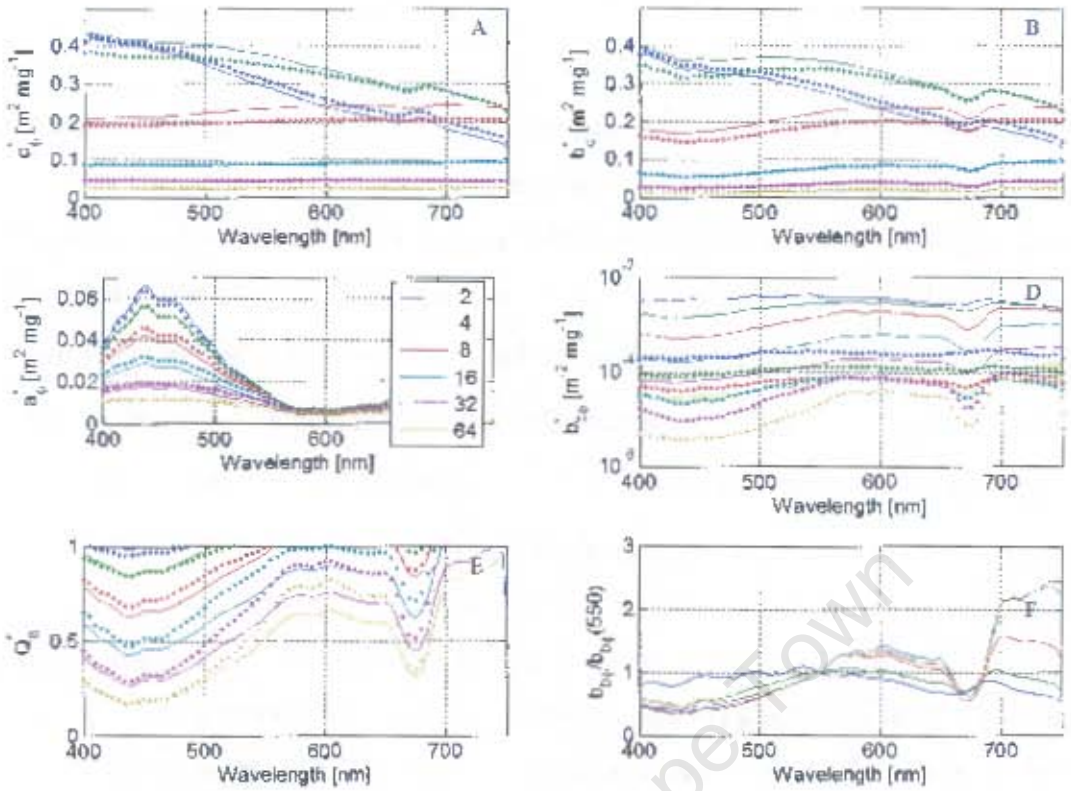

Figure 4.9 Chl *a*-specific inherent optical properties, package effect parameter and backscattering spectral shape data for Standard size distributions of varying d_{eff} and constant v_{eff}=0.2, based upon diatom refractive index data. Effective diameter values (μm) are given in the legend for data from the two-layered geometry (lines) and homogeneous geometry (dots). Figures are A) Chl *a*-specific attenuation coefficient $c_\phi^*(\lambda)$, B) Chl *a*-specific scattering coefficient $b_\phi^*(\lambda)$, C) Chl *a*-specific absorption coefficient $a_\phi^*(\lambda)$, D) Chl *a*-specific backscattering coefficient $b_{b\phi}^*(\lambda)$, E) package effect parameter $Q_a^*(\lambda)$, F) Algal backscattering coefficient normalised to 550 nm. Homogeneous refractive indices are calculated from volume equivalence to the two-layered data to facilitate comparison, with c_i =2.3 kg m^{-3} and Vv=20%.

The simulated diatom Chl *a*-specific absorption (Fig. 4.9C) and package effect parameter (Fig. 4.9E) spectra display well known characteristics with regard to changing size – higher absorption and less packaging at smaller sizes [Kirk 1975, Morel & Bricaud 1981, Ciotti *et al.* 2002]. Geometry related effects are not large and vary with size – for small cells the heterogeneous geometry produces higher $a_{\phi}^{*}(\lambda)$ and $Q_{a}^{*}(\lambda)$ values (i.e. lower packaging) with a maximum difference of ~ 10 %. For large cells the situation is reversed – the heterogeneous geometry produces lower $a_{\phi}^{*}(\lambda)$ and $Q_{a}^{*}(\lambda)$ values (i.e. higher packaging) with a maximum difference of ~ 20 %. These are consistent with the single cell analyses of Figure 4.2. The geometry related differences for small cells are also consistent with the observations of Geider & Osborne [1987], who found experimentally determined cellular packaging for a small diatom species to be lower than theoretical predictions, and ascribed the differences at least in part to cellular heterogeneity. No comparable study with regard to large cells is known to the author. Nevertheless, the predicted absorption coefficients and package effect parameters for the simulated populations are consistent with observation [*ibid.*], and reveal small but significant differences arising from cellular heterogeneity.

Geometry related differences in the Chl *a*-specific backscattering coefficient $b_{b\phi}^{*}(\lambda)$ (Fig. 4.9D) and backscattering probability $\tilde{b}_{b\phi}(\lambda)$ (not shown) are large, and similar to those discussed for Figure 4.8. Heterogeneous populations produce $b_{b\phi}^{*}(\lambda)$ and $\tilde{b}_{b\phi}(\lambda)$ values ranging from ~ 200 % to ~3500 % higher than their homogeneous equivalents, with small celled populations exhibiting the greatest differences. Backscattering values are highest for small sizes, as is expected with Chl *a*-specific $b_b(550)=3.8\times10^{-3}$ m^2 mg^{-1} for the 2 µm population and $b_b(550)=6\times10^{-5}$ m^2 mg^{-1} for the 64 µm population. Small and intermediate sized cell populations also display greater absolute spectral variability in their backscattering spectra, with spectral standard deviations ~ 5 to 10 times higher than those for larger cell populations. The normalised backscattering spectra (Fig. 4.9F) provide further evidence that the shape of the backscattering coefficient is strongly size-dependent, showing pronounced anomalous dispersion effects at all sizes other than the

smallest diameter population. In addition, the backscattering shape at larger sizes show a pronounced broad maximum at red wavelengths – the effects of this phenomenon have been observed in the pronounced red reflectance peak in high biomass bloom waters [Carder & Steward 1985, Gower *et al.* 1999, Roesler & Boss 2003]. Understanding the phenomenon is thus extremely important with regard to the application of bio-optical and ocean colour techniques to harmful algal bloom monitoring, where the effects of elevated algal backscattering at red wavelengths are likely to be most pronounced.

Figure 4.6F shows that the effect is not due to elevated real refractive index values at these wavelengths. The cause of the phenomena would appear rather to be partially due to the imaginary refractive index, or rather the lack of it – the n'_{chlor} and n'_{cyto} values at > 700 nm are extremely low ($<1\times10^{-5}$). Figure 4.4 shows that low imaginary refractive indices, either for the chloroplast or the entire cell, result in elevated backscattering values – this effect is considerably pronounced at very low values n'_{chlor} values, e.g. $<1\times10^{-5}$ (data not shown). The reason why larger cells show elevated backscattering maxima at red wavelengths in comparison to smaller cells would appear to be due to α related changes. Figure 4.5D (green dashed line) shows that when considering the α vs Q_{bb} relationship for polydispersed cells with low imaginary refractive index there are three distinct regions: a) with $\alpha < \sim 70$, Q_{bb} increases sharply with α, 2) with α between ~ 70 and ~ 400, Q_{bb} decreases sharply with α, and 3) with $\alpha > \sim 400$, Q_{bb} decreases slowly with α. Wavelength induced changes in α across these zones, where Q_{bb} changes rapidly, will thus lead to prominent spectral features in the backscattering spectra. It must also be appreciated that small cells have narrower α ranges: a 4 µm cell would have associated α values of ~42 and ~24 at 400 nm and 700 nm respectively, as compared to a 32 µm cell with analogous α values of ~335 and ~ 192. Large cells with low imaginary refractive index values are thus more prone to rapid increases in Q_{bb} with increasing wavelength (decreasing α) effectively the spectral range of the Q_{bb} spectra > 700 nm falls within the second region discussed above. This phenomenon, in combination with anomalous dispersion effects resulting from the high n'_{chlor} values at the red Chl *a* peak, appear to

produce the distinct backscattering maximum at red wavelengths for large celled assemblages.

There are implications to this phenomenon, with regard to both algal absorption and backscattering. Residual measured absorption at long wavelengths is often considered due to scattering, and can be corrected for using both estimates of scattering [Bricaud & Morel 1983] and a null point correction [Roesler 1998] – the technique adopted in this study [Chapter 2]. The absorption characteristics of algae in the near infra-red are still open to debate, not least due to the methodological difficulties of measuring low absorption values of scattering particles. Whilst some studies have concluded that algal absorption in the red is small [Babin & Stramski 2002], others have measured residual absorption at red wavelengths that cannot be accounted for by scattering processes [Bricaud *et al.* 1983, Osborne & Geider 1989]. Given the sensitivity of backscattering to even small changes in the imaginary refractive index at these wavelengths, it would appear that correct measurement of algal absorption is of great importance to establishing the nature of algal backscattering at red to infra red wavelengths.

Figure 4.10 displays the Chl *a*-specific inherent optical properties of simulated dinoflagellate populations of effective diameters from 2 μm to 64 μm. The input parameters differ to those used in Figure 4.9 in that the *dinoflagellate* refractive index spectra are used, c_i=4 kg m^{-3} and Vv=30 %. The lower magnitudes of the $c_\phi^*(\lambda)$ (Fig. 4.10A) and $b_\phi^*(\lambda)$ (Fig. 4.10B) spectra, by comparison to the diatom simulation (Fig. 4.9A), are due primarily to the effects of the higher c_i value of the dinoflagellate sample. Whilst the differences between the analogous optical efficiency spectra are relatively small, the Chl *a*-specific size distributions calculated with Equations 4.25 to 4.27 are ~ 40 % smaller in the dinoflagellate case. In the case of absorption (Fig. 4.10C), the higher Q_a values resulting from the increased c_i values and larger chloroplast volume are more than offset by the smaller size distributions to produce $a_\phi^*(\lambda)$ values ranging from ~ 8 % to ~ 40 % smaller than those of the diatom populations. Similar considerations hold for the package effect – the dinoflagellate populations display ~ 8 % greater packaging for small

cells increasing to ~ 40 % for the large celled assemblages. Simulated dinoflagellate backscattering (Fig. 4.10D) is ~2 to 4 times lower than that for corresponding diatom populations – this is primarily due to the higher central real refractive index value of the diatom population. The red backscattering maximum is noticeably more enhanced for the dinoflagellate populations (Fig. 4.10F), due to the higher relative assumed chloroplast volume of *Vv*–30 %, leading to $Q_{bb}(700)$ values ~ 50 % higher than *Vv*–20 % values. Given that the pronounced red reflectance peaks that would result from this elevated long wavelength backscattering are typically associated with very high biomass dinoflagellate blooms [Carder & Steward 1985, Gower *et al.* 1999, Roesler & Boss 2003] it is tempting to interpret these data as being typical of large celled dinoflagellates. However, this would be somewhat simplistic, particularly given that the data used here employ somewhat generalised morpological values, and that the imaginary refractive index data at red wavelengths are generated from absorption data measured in a spectral region with low signal:noise ratios and employing a null point correction. There is also considerable complexity introduced in the translation of algal spectral backscattering features into reflectance data representative of the water body as a whole. Nevertheless the enhanced red wavelength backscattering features seen here are consistent with observation and worthy of closer investigation.

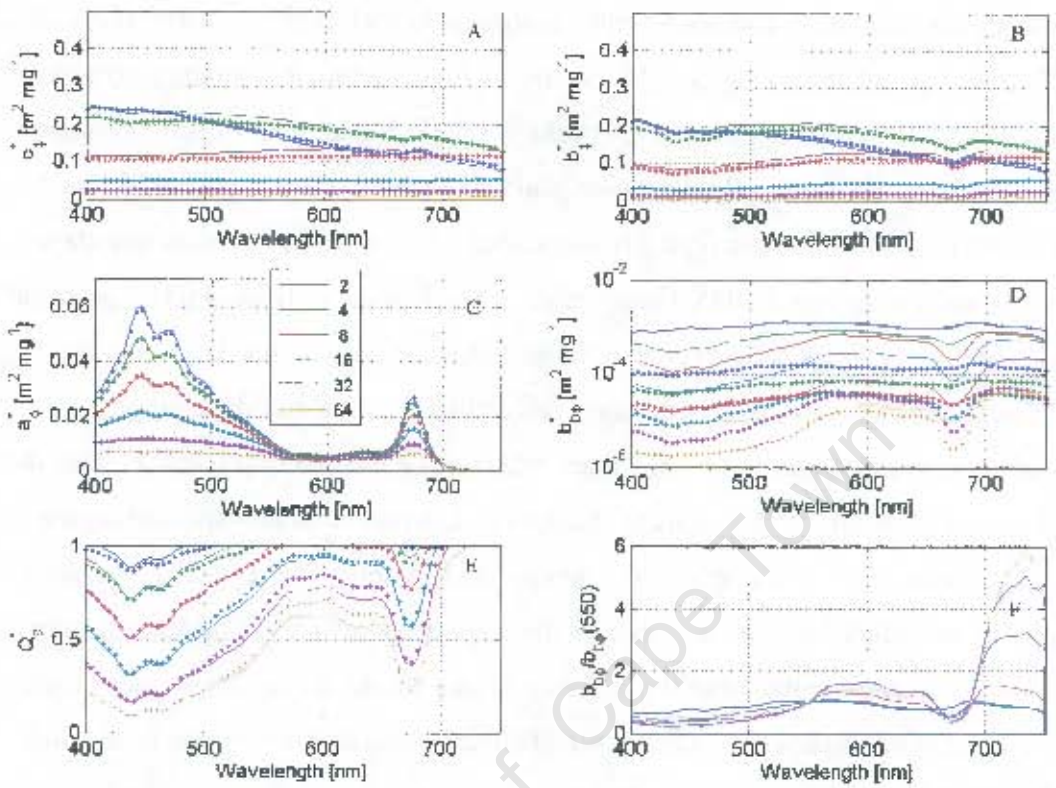

Figure 4.10 Chl *a*-specific inherent optical properties, package effect parameter and backscattering spectral shape data for Standard size distributions of varying effective diameter, based upon dinoflagellate refractive index data. Effective diameter values (μm)are given in the legend for data from the two-layered geometry (lines) and homogeneous geometry (dots). A) Chl *a*-specific attenuation coefficient $c_\phi^*(\lambda)$, B) Chl *a*-specific scattering coefficient $b_\phi^*(\lambda)$, C) Chl *a*-specific absorption coefficient $a_\phi^*(\lambda)$, D) Chl *a*-specific backscattering coefficient $b_{b\phi}^*(\lambda)$, E) package effect parameter $Q_a^*(\lambda)$, F) Algal backscattering coefficient normalised to 550 nm. Homogeneous refractive indices are calculated from volume equivalence to the two-layered data to facilitate comparison, with c_i =4 kg m^{-3} and Vv=30%.

4.6 Preliminary Validation of the Two-Layered Geometry

Absolute validation of the two-layered model would require comparison with full angular scattering measurements of cultured algal populations [Quinby Hunt *et al.* 1989] – such data are not available to this study. Currently commercially available backscattering instrumentation are in essence single- or multi-angle scattering meters, from which volume backscattering coefficients are calculated based upon assumptions rooted in Mie theory [Maffione & Dana 1997, Boss *et al.* 2001]. Validation with such instruments would require measurements of cultured algae [Vaillancourt *et al.* 2004] – again, such data are not available to this study. However even in such circumstances the use of these instruments would provide uncertain validation, as the Mie theory upon which their spectral backscattering derivations are based has been shown to be somewhat inappropriate to the simulation of algal angular scattering. An alternative to the use of dedicated backscattering instruments is offered by the use of reflectance data; or more accurately the often used reflectance approximation [Morel & Prieur 1977, Zaneveld 1995, Roesler & Perry 1995].

This approximation, commonly used for reflectance inversion algorithms [*ibid.*] expresses the light leaving the sea surface in terms of the absorption and backscattering properties of the water column. Using remote sensing reflectance R_{rs} [Zaneveld 1995]

$$R_{rs} = \frac{L_u(0^-,\lambda)}{E_d(0^+,\lambda)} = \frac{f}{Q}\frac{b_b(\lambda)}{a(\lambda)+b_b(\lambda)} \qquad (4.28)$$

where $L_u(0^-,\lambda)$ is the upwelling radiance just above the sea surface, $E_d(0^+,\lambda)$ is the downwelling irradiance just above the sea surface, f/Q is an assumed constant (≈0.085) describing the angular structure of the light field, and $a(\lambda)$ and $b_b(\lambda)$ are the total absorption and backscattering coefficients respectively. It is thus possible to relate the absorption and backscattering coefficients in the upper optical depths [Gordon & Mcluney 1975] to measurements of the upwelling radiance and downwelling irradiance. In practice, in-water reflectance measurements require that the upwelling radiance moeity is

necessarily made at some nominal depth below the surface, requiring the further use of a propagation scheme to describe the attenuation of upwelled radiance as it is propagated to the surface [Albert & Mobley 2003]. Given that the diffuse attenuation coefficient for upwelling radiance can be also expressed in terms of the absorption and backscattering coefficients [*ibid.*], Equation 4.28 can be reformulated to explicitly solve for the upwelling radiance L_u measured at depth z:

$$L_u(z,\lambda)=\frac{f}{Q}\frac{\eta^2}{\tau}\frac{b_b(\lambda)}{a(\lambda)+b_b(\lambda)}\frac{E_d(\lambda)}{\exp(-K_u(\lambda)z)} \qquad (4.29)$$

where η/τ is an assumed constant (=1.3612) describing the transmittance across the air-sea interface, K_u is the diffuse attenuation coefficient for upwelling radiance and other notation is as for Equation. 4.28. The diffuse attenuation coefficient for upwelling radiance K_u is dependent upon the total absorption and backscattering coefficients, and solar zenith angle θ_s, using the formulation of Albert & Mobley [2003]:

$$K_u=(a+b_b)\left[1+\left(\frac{b_b}{a+b_b}\right)\right]^{3.452}\left(1-\frac{0.2786}{\cos\theta_s}\right) \qquad (4.30)$$

In most waters, the total absorption and backscattering coefficients will include contributions from constituents other than water itself and the algal component: these include gelbstoff, organic detritus, small particles such as bacteria, viruses and lithogenic particles, and sediment in areas of significant terrestrial input. However, algal blooms of extraordinary biomass can provide scenarios where it is not unreasonable to assume that the sea's optical properties are dominated only by algae and water, and the effects of other constituents can be regarded as negligible. This is particularly so in scenarios where there is little riverine input, such as the southern Benguela. The use of the reflectance approximation as a validation tool does suffer from some uncertainties with regard to assumptions concerning the angular structure of the light field [Zaneveld *et al.* 1995, Morel *et al.* 2002]. However, it is of particular advantage to this study in that it offers a means of directly calculating the integrated backscattering coefficient, and in addition

allows an assessment of the effects of adopting a more complex algal geometry on ocean colour measurements.

Under this reasoning, reflectance data from two extraordinary blooms occurring in the Lamberts Bay region of the southern Benguela are used to assess the validity of the two-layered geometry with regard to algal optics. The first of these events occurred in October 2002; a bloom of the large dinoflagellate *Alexandrium catenella*, with microscope counts taken during sampling revealing a unialgal bloom with cell concentrations of 9.8 million cells l^{-1}. The second bloom, occurring in April 2004, was of the small dinoflagellate *Prorocentrum triestinum* – microscope counts again showed a unialgal bloom with cell concentrations of 120 million cells l^{-1}. Even in a productive system suffering the frequent occurrence of high biomass dinoflagellate blooms [Pitcher *et al.* 1998], these events were conspicuous both by their magnitude and monospecific nature.

4.6.1. Methods for Radiance Comparisons

Principal measurements consist of in-water hyperspectral radiometric measurements, and algal microscopic counts and size calculations used to derive algal size distributions. Radiometric measurements were made with two in-water hyperspectral instrument systems. Measurements of the *A. catenalla* bloom utilised a Satlantic Hyperspectral Tethered Surface Radiometer Buoy (H-TSRB) – a tethered surface buoy measuring upwelling radiance at a nominal depth of 0.66 m, and above surface downwelling irradiance. The *P. triestinum* bloom was measured using a TRIOS ACC sensor, measuring downwelling above surface irradiance, and a TRIOS ARC radiance sensor measuring upwelling radiance at a nominal depth of 0.4 m. The TRIOS sensors were mounted on a prototype coastal bio-optical monitoring buoy, using a modified Ocean-i power and data control system (Saturn Solutions, UK). The two systems can be considered approximately analogous with regard to measurement geometry and radiometric sensitivity, and both have a spectral resolution of ~ 3 nm. Radiometric measurements were made for a duration of two to five minutes, with sampling rates (dictated by radiance integration times) of ~ 0.5 Hz. Median values from the whole

sampling period were used to derive single spectra for both sensors, resampled to a wavelength resolution of 5 nm. Microscope counts were made on samples preserved with buffered formalin and counted using the Utermohl [1958] technique. Mean equivalent volume spherical cell diameters were calculated based on ~ 40 microscope measurements of cell dimensions, utilizing a spheroidal geometry to calculate cell volume

Modelled upwelling radiance spectra are calculated using several steps: Standard size distributions, as discussed in Chapter 2, were generated using the microscope cell concentration and d_{eff} data, using an effective variance of v_{eff}=0.006 – the narrowest possible numerically stable distribution using the Hansen & Travis [1974] formulation. The integrated total number of particles for each distribution were forced to match reported cell concentration values of 9.8×10^{9} cells m^{-3} for the *A. catenella* bloom and 1.2×10^{11} cells m^{-3} for the *P. triestinum* bloom. Equation 4.12 was then used to calculate algal absorption and backscattering properties using the microscope-derived size distribution and optical efficiency factors modeled from the *dinoflagellate* refractive index data (Figures 4.6E and 4.6F). Optical data for two-layered cells with chloroplast volumes of Vv=20 % and Vv=30% were generated, in addition to data for a volume equivalent homogeneous geometry.

Equation 4.29 was then used to calculate simulated upwelling radiance spectra, using measured downwelling irradiance spectra, the modelled algal absorption and backscattering coefficients, and the absorption and backscattering of water. For the absorption of pure water the data of Pope & Fry [1997] were used for 400 nm to 725 nm, with scaled data from Buiteveld *et al.* [1994] used for 730 nm to 750 nm. The equations of Morel [1974] were used to generate pure seawater backscattering coefficients.

4.6.2. Results of Radiance Comparisons

Microscope-derived size distributions can be seen in Figures 4.11E and 4.12E, based on calculated effective diameter values of d_{eff}=30 µm for *A. catenella* and d_{eff}=13 µm for *P. triestinum*. The Standard distribution for the *A. catenella* sample (using the smallest possible numerically stable v_{eff} value) appears rather wide for a unialgal event, and simulations were checked using normal and log-normal distributions allowing considerably narrower distributions - reflectance perturbations with narrower size distributions were relatively minor (<10 %).

The measured upwelling radiance spectra (Figures 4.11A and 4.12A) can be considered typical of very high biomass waters, and are characterized by low light levels in the blue and a red peak located at > 700 nm. This peak must be distinguished from the sun induced natural fluorescence peak [Babin *et al.* 1996], typically located at ~ 683 nm. As concerns the *A. catenella* simulations in Figure 4.11, the simulated radiance data show a reasonable match to measured data, with considerable geometry-related variability. Given the very low radiance values below ~ 550 nm and between ~ 660 nm and ~ 680 nm, comparisons will be restricted to values at the two main radiance peaks, located at ~ 580 nm and ~ 710 nm. The two-layered Vv=20% data would appear the best matched geometry, with a relative underestimate of ~ 10 % at 580 nm and a relative overestimate of ~ 80 % at 710 nm. In comparison the two-layered Vv=30% data appear to backscatter too strongly in the red (Fig. 4.11C), overestimating reflectance at 710 nm by > 100 %. This is consistent with previous discussions of morphologically induced variability in the red backscattering phenomena, and indicates the importance of the assumed morphology in such an approach. The homogeneous geometry underestimates radiance by ~ 80 % at both radiance peaks. Comparison of the absorption (Fig. 4.11B) and backscattering (Fig. 4.11C) data show that geometry-related absorption variability is small (< 15 %) in comparison to backscattering variability, where the homogeneous geometry produces b_b values ~ 20 % to 60% lower than those of the heterogeneous b_b values.

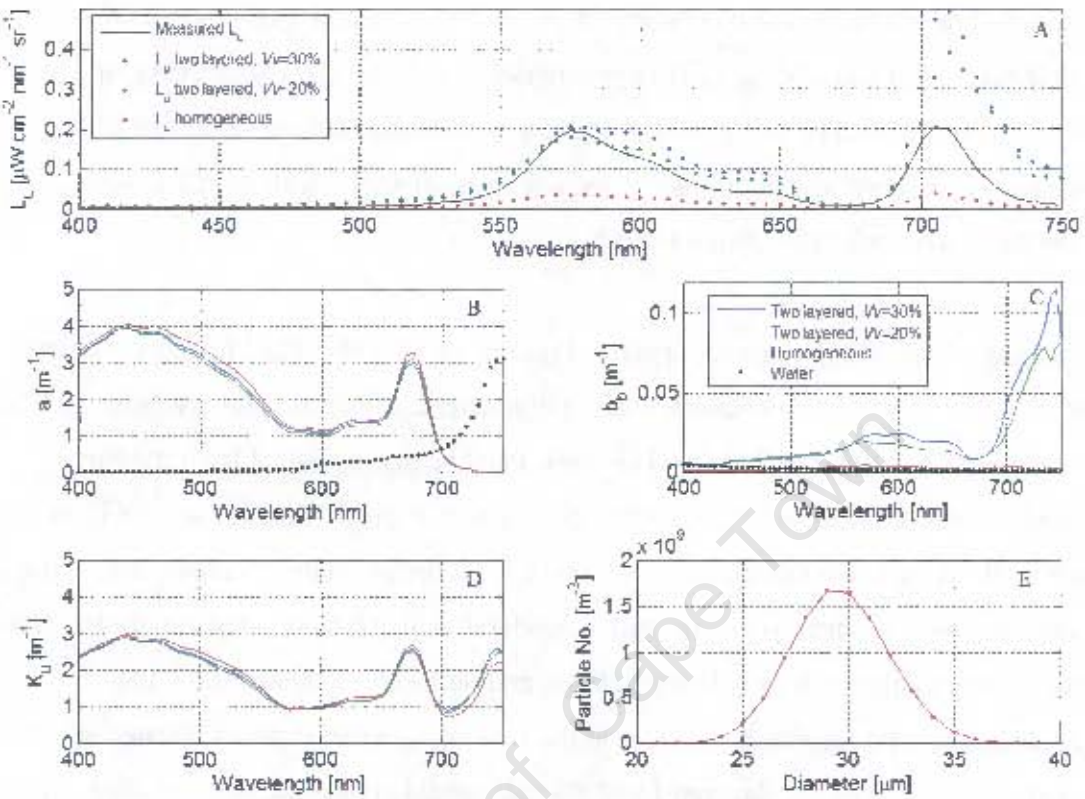

Figure 4.11 Comparison of measured and simulated upwelling radiance L_u for an *Alexandrium catenella* bloom with cell concentrations of 9.8×10^6 cells l^{-1}. A) Measured and simulated upwelling radiance L_u for various geometries, B) Simulated algal absorption coefficients and the absorption coefficient of pure water, C) Simulated algal backscattering coefficients and the backscattering coefficient of pure seawater, *D*) Diffuse attenuation coefficient for upwelling radiance K_u, used to propagate measured L_u to the air-sea interface, and E) Microscope derived algal size distribution.

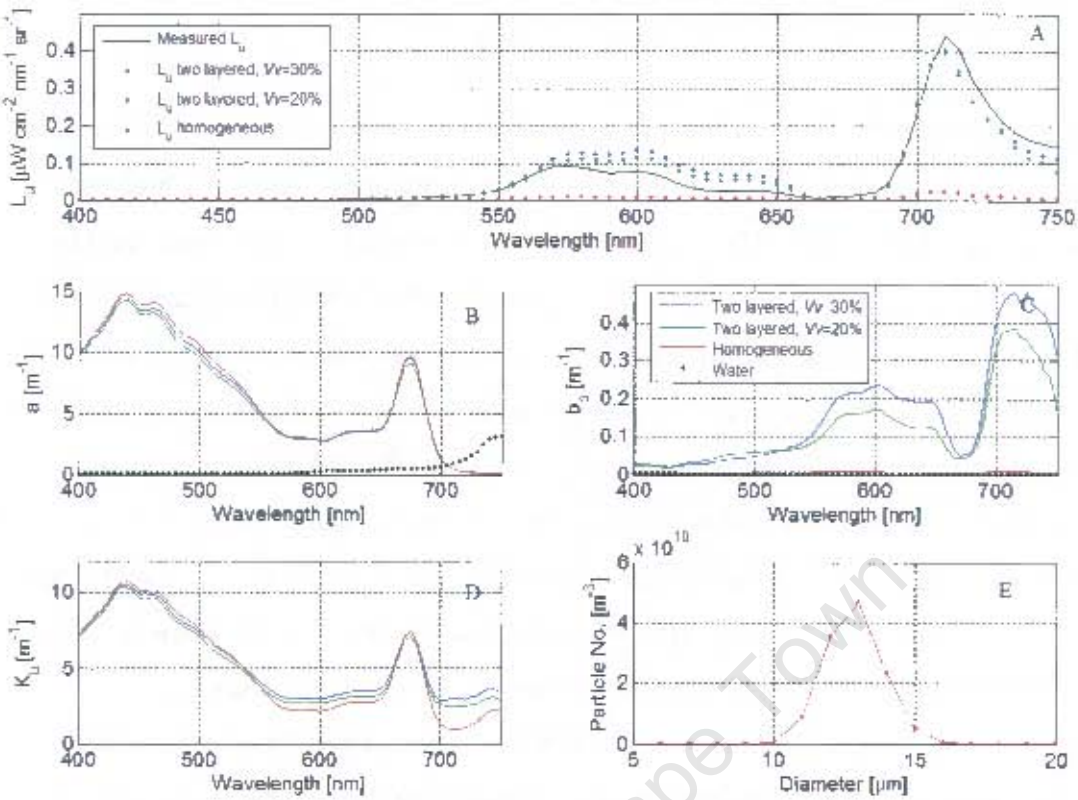

Figure 4.12 Comparison of measured and simulated upwelling radiance L_u for a *Prorocentrum triestinum* bloom with cell concentrations of 1.2×10^8 cells/litre. A) Measured and simulated upwelling radiance L_u for various geometries, B) Simulated algal absorption coefficients and the absorption coefficient of pure water, C) Simulated algal backscattering coefficients and the backscattering coefficient of pure seawater, D) Diffuse attenuation coefficient for upwelling radiance K_u, used to propagate measured L_u to the air-sea interface, and E) Microscope derived algal size distribution

In comparison to the *A. catenella* bloom, the *P. triestinum* event showed much higher cell concentrations of a smaller organism (d_{eff}=13 µm), leading to a relatively high red wavelength radiance peak. The geometry-related differences are even more marked than for the previous assemblage, with the homogeneous cells underestimating measured radiance by up to 100 %. The comparison between the two heterogeneous geometries is not as marked as for the previous assemblage (~ 5 % to 30 % differences at 580 nm and 710 nm), although it would appear once again that the *Vp*=20 % geometry is more appropriate, as it provides a slightly closer match to the measured radiance in the 580 nm to 650 nm range. Again geometry-related differences in absorption (Fig. 4.12B) are small (< 10 %), whilst backscattering differences are considerable, with the homogeneous geometry yielding backscattering values up to 95 % lower than those of the heterogeneous geometry. The close match of the measured and simulated radiance using the heterogeneous geometries, and the poor match using the homogeneous geometry, would suggest that the two-layered geometry as it is configured here is appropriate for algal bio-optical applications.

Whilst the reflectance approach does allow the ability to confirm that the magnitude of backscattering is within appropriate ranges, the very low radiance at blue wavelengths does not allow an assessment of the simulated backscattering spectral shape throughout the visible spectrum. Nevertheless, the reasonable simulated radiance comparisons from ~ 550 nm to 750 nm, with backscattering spectra that display considerable anomalous dispersion effects (Fig. 4.12C) at these wavelengths, indicates that the highly structured backscattering spectra that are predicted by theory are not unreasonable. The data used in the simulation are derived from a combination of theoretical considerations, literature derived values, and absorption and size measurements from a dinoflagellate assemblage measured several years before the bloom events shown above. The close comparison between measured and simulated radiance data, based solely on the derived optical efficiency factors and microscope-derived size parameters, confirms the validity of the approach and the general application of heterogeneous geometry algal optics to in-water bio-optical application.

4.7 Conclusions

The study has outlined a general structure for the simulation of algal optical properties using two-layered geometry models. An initial analysis of the effects of manipulating causal variables on algal IOPs has been conducted. The adopted structure uses an inner layer representing the cytoplasm, which typically occupies most of the cell volume, and an outer layer representing the chloroplast (or chloroplasts). The model geometry has been shown to be appropriate using several arguments: it is appropriately packaged from a physiological perspective, it is able to simulate observed absorption efficiency factors, it has intracellular real refractive index gradients more closely approximating those geometries explicitly considering an optically "hard" peripheral cellular membrane, and there is a considerable body of morphological observations supporting the assumption of peripheral chloroplast location. Appropriate relative volume and refractive index ranges have been established for algal chloroplasts and cytoplasm; from a volume equivalent perspective these values are consistent with previous observation, both from a cellular composition and an optical perspective. Based on these data and field measurements of algal absorption and size distributions, chloroplast refractive index spectra have been derived for several algal assemblages typical of the Benguela system. These data have been used to assess the changing nature of algal optical efficiency factors and inherent optical properties with regard to cellular heterogeneity, and changes in assemblage size and composition.

It appears that the adoption of two-layered geometry has a relatively minor impact upon optical properties that are not dependent upon angular scattering processes – attenuation, total scattering and absorption properties, including the package effect parameter. These findings are supported by previous modeling studies [Aas 1984, Zaneveld & Kitchen 1995], and are generally consistent with the widespread and successful use of the anomalous diffraction approximation and Mie modeling to describe non-angular optical properties. However, angular scattering properties, of which the integrated backscattering is focused on here, are considerably affected by the adoption of a heterogeneous geometry. Algal backscattering coefficients associated with a heterogeneous geometry

are between 5 and 25 times higher than their homogeneous volume equivalent counterparts; considerable differences in the spectral shape of the backscattering spectra are also induced by geometry change. The nature of these geometry-related differences vary considerably with size and intracellular refractive index.

Assessment of the size and assemblage-specific inherent optical properties show that non-angular coefficients behave consistently with previous observation and theory – examples include the changing slope of the attenuation coefficient with size, and package effect related variability in the absorption coefficient. In an analogous manner, variability in the algal backscattering coefficient can be characterized: spectral variability can be large and is size dependent, populations dominated by small cells backscatter considerably more than those dominated by large cells, and the real refractive index of the chloroplast (or equivalent peripheral layer) is the dominant influence on backscattering. It must be realised that this study makes somewhat simplistic assumptions with regard to algal morphology and intracellular refractive index values, and must be regarded as a preliminary attempt to create a general heterogeneous geometry for the simulation of spectral algal optical properties. Further data are needed, particularly with regard to the intracellular refractive index and intracellular morphology of algal groups from a systematic perspective. Nevertheless, the reflectance based validation indicates the validity of the adopted backscattering geometry and refractive index structure, and indicates that it is possible to establish a quantitative formulation between single particle optics and ocean colour. Such an approach offers the ability to express the algal contribution to *in situ* or remotely measured ocean colour data purely in terms of a population of particles, or more importantly for HAB applications, population size and accessory pigment related refractive index variability. An immediate application is HAB oriented inverse reflectance models; the combined use of particle size distributions with the heterogeneous geometry can establish size and assemblage-specific, coupled and easily manipulated algal absorption and backscattering coefficients.

Chapter 5

A Hyperspectral Reflectance Inversion Model Utilising Size Distributions of Two-Layered Spheres for the Description of Algal Populations.

5.1 Introduction

The light leaving the surface of the sea contains a wealth of information concerning the constituents of surface waters; most significant ecologically of which is the population of phytoplankton within the upper optical depths. Ocean colour is thus a valuable source of information to marine scientists, allowing a greater understanding of phytoplankton dynamics and the ensuing effects on biogeochemical cycles in the world ocean. The ability to measure ocean colour on a variety of spatial and temporal scales, using both satellites and in-water platforms, emphasises the utility of these data for algal detection, quantification and dynamic analyses. As ocean colour sensor systems, both *in situ* and satellite borne, become more refined and readily accessible, further application of ocean colour data can be expected. An emergent ocean colour application that will be focussed on here is the detection and monitoring of harmful algal blooms (HABs) in coastal waters.

The effective use of passive ocean colour measurements for HAB detection is reliant upon the use of inverse reflectance algorithms capable not only of quantifying algal biomass at high algal concentrations, but also allowing some form of distinction between phytoplankton assemblages dominated by different taxonomic groups. A range of such algorithms have been developed to obtain information on algal populations based principally on radiative transfer theory; techniques that potentially have broad ranging application to the bio-optical monitoring of coastal waters for harmful algal blooms [e.g. Roesler & Perry 1995, Garver & Siegel 1997, Roesler & Boss 2003]. These analytical or semi-analytical reflectance algorithms typically make use of the reflectance approximation [Morel & Prieur 1977, Zaneveld 1995], allowing the inversion of ocean colour data by parameterising reflectance in the form $R \propto b_b / (a + b_b)$, where b_b is the total backscattering coefficient and a is the total absorption coefficient. Such algorithms typically use a spectral mixture approach, employing scaleable canonical basis vectors or analogous formulations, to simulate and quantify the absorption and backscattering coefficients of the principal ocean constituents [Roesler & Perry 1995, Garver & Siegel 1997, Roesler & Boss 2003]. These include the water itself, the algae and their associated

retinue of detrital breakdown products, dissolved organic material otherwise variously known as gelbstoff, yellow substance, gilvin or chromophoric dissolved organic matter (CDOM), suspended sediment in areas of high terrigeneous input, and various other small particles such as bacteria and lithogenic particles [*ibid.*]. The approach is thus reliant upon an effective parameterisation of constituent specific absorption and backscattering coefficients - most importantly those of the algal population.

Of particular importance is the understanding and parameterisation of the spectral contribution of algal cells to the bulk backscattering coefficient - the integrated angular scattering that is responsible for returning light to the surface of the sea. Whilst algal absorption is relatively well understood with regard to both chemotaxonomic variability and other causal processes [Morel & Bricaud 1981, Bricaud *et al.* 1988, Johnsen *et al.* 1997], algal backscattering is poorly understood: it is a difficult parameter both to measure [Ahn *et al.* 1992, Vaillancourt *et al.* 2004], and to simulate using homogeneous geometry scattering models [Quinby-Hunt *et al.* 1989, Volten *et al.* 1998]. Uncertainties concerning algal backscattering variability has lead to the adoption of simplified spectrally invariant basis vectors, decoupled from algal absorption, to parameterize backscattering in inverse reflectance models [Roesler & Perry 1995, Garver & Siegel 1997]. An exception to this is the scheme adopted by Roesler & Boss [2003], who used a backscattering term coupled to the beam attenuation and absorption coefficients, based on the results of Mie modelling of homogeneous particles conforming to a Junge size distribution [Ulloa *et al.* 1994, Boss *et al.* 2001b]. Such a formulation allows some spectral shape to the simulated algal backscattering coefficient (as predicted by anomalous dispersion), and is coupled to the changing size distribution of the particulate component (as given by the slope of a Junge distribution) through the beam attenuation coefficient and backscattering probability. However, this "c-model" formulation, whilst offering a more representative backscattering parameterisation, is still somewhat restrictive for several reasons. Firstly, it employs a constant (i.e. spectrally invariant) backscattering probability factor – evidence suggests that this is unlikely to be the case for natural waters [Morel *et al.* 2002]. Secondly, the attenuation slope parameterisation [Equation 6, Roesler & Boss 2003] upon which the backscattering term is based, is

derived using assumptions that may not be appropriate for biologically dominated waters the use of Junge particle size distributions, and the use of either non-absorbing particles or particles with spectrally invariant imaginary refractive indices [Boss *et al.* 2001b].

Chapter 4 has demonstrated that it is possible to closely simulate the reflectance spectra of biologically dominated waters by representing the optical properties of an algal population using Standard size distributions of two-layered spheres with appropriate refractive index characteristics. The adoption of such a formulation for a more general inverse reflectance algorithm potentially offers several advantages over previous algorithm structures. The approach allows a more holistic description of algal inherent optical properties; one in which the algal absorption and backscattering coefficients are coupled at a fundamental level. In addition, whilst the two-layered geometry is relatively untested as concerns algal simulation across a broad range of scenarios, it would appear to provide more realistic simulations of algal backscattering properties than previous reflectance algorithm parameterisations, offering variable spectral shape and backscattering probability. Importantly, this variability is manipulated strictly in terms of fundamental causal variables such as algal size, intracellular Chl *a* concentration and spectral refractive index. Parameterisation of the algal component in this way thus not only offers the possibility of inverting reflectance in terms of algal absorption and backscattering, but also directly and quantifiably in terms of causal parameters, such as assemblage size. The use of spectral mixing models, based on accessory pigment related spectral refractive index variability, may also allow the derivation of quantitative chemotaxonomic data [e.g. Chapter 3]. Additionally, expressing the algal absorption and backscattering from explicit particle optic calculations gives the ability to derive other inherent optical properties potentially desirable for ecophysiological modelling, such as attenuation, scattering and volume scattering coefficients, and the package effect.
This study will thus seek to implement an inverse reflectance algorithm based on a non-linear solution of the reflectance approximation in terms of the total absorption and backscattering coefficients of the upper optical depths. The optical properties of natural algal populations will be represented with Standard size distributions of two-layered particles. In addition to the calculation of Chl *a* concentrations and an assemblage size

descriptor (as given by the effective diameter of the size distribution), the algorithm will also investigate the potential of deriving accessory pigment concentrations through the use of spectral mixing models. Whilst the algorithm as presented here is designed for use with *in situ* hyperspectral reflectance data, the structure of the algorithm allows potential modification for use with multi-spectral space based ocean colour data. The algorithm is tested here with in-water hyperspectral radiometric data sampled across a wide range of water types in the southern Benguela, using concurrently measured independent absorption, particle size distribution and HPLC pigment data to assess algorithm performance. Assessment is made with regard to the accuracy and precision of model determinations, and the potential utility of returned algal descriptors for application in harmful algal bloom monitoring.

5.2 Field Methods

Bio-optical measurements were made on near-surface samples from diverse water types, ranging from the near oligotrophic to high biomass algal blooms dominated by a variety of algal species. Sampling was conducted from 2002 to 2004 in the southern Benguela from a variety of platforms (see Table 5.1), and forty-three samples in total were analysed for this study. Principal measurements consisted of hyperspectral radiometry, phytoplankton, detrital and gelbstoff absorption, particle size distributions, and intra-cellular pigments. Identification of dominant algal species and groups were made using a combination of microscope analysis of fresh and preserved samples and chemotaxonomic information from HPLC pigment analyses.

Table 5.1 Description of sampling locations and dates, with general assemblage descriptions and biomass ranges (see Appendix II).

Date	Cruise identifier & location	Dominant Algal Groups	Chl *a* (mg m^{-3})
Ocober 2002	BenCal southern Benguela	Mixed	0.24 to 23
Ocober 2002	LB02 Shore based Lamberts Bay	*Alexandrium catenella*	309
January 2003	SBOC03 Shore based Saldanha Bay	*Aureococcus anophagefferens*	12 to 14
March 2003	LB03 Shore based Lamberts Bay	Mixed	1 to 17
March 2004	LB04 Shore based Lamberts Bay	Mixed, *Mesodinium rubrum*, *Pseudo-Nitzschia* spp.	3 to 70

5.2.1 Radiometric Measurements

In-water hyperspectral radiometric measurements were made with a Hyperspectral Tethered Surface Radiometer Buoy (HyperTSRB S/N 018), manufactured by Satlantic, Inc. (Halifax, Canada), and is designed to obtain upwelling near surface spectral radiance Lu(z) and above surface downwelling irradiance Ed (0+), away from vessel perturbations in the submarine light field. Upwelling radiance is measured at a nominal depth of z = 0.66 m. The instrument consists of two 256 channel spectrographs linked by fiber optic

bundles to an upward looking cosine corrected irradiance sensor, and a downward looking 8.5° field of view radiance sensor. Adaptive gain allows a variable integration time to be chosen independently for each sensor head based on the current light field. Actual acquisition rates are therefore variable and dependent upon instrument response to the light field, and typically range from 0.7 Hz to 1.6 Hz. The 256 channel spectrographs provide a spectral range of 400 nm to 800nm, at a spectral resolution of 3.3 nm and accuracy of 0.3 nm. Radiometric measurements were typically made for a duration of 2 to 5 minutes, with median values from the whole sampling period used to derive single spectra for both sensors, re-sampled to a wavelength resolution of 5 nm. Further processing of radiometric data, namely propagation of radiance data through the water column and air-sea interface, were carried out as an integral part of the reflectance algorithm, as presented below.

5.2.2 Particulate Absorption

Particulate absorption data were measured with the quantitative filter pad technique [Yentsch 1962, Roesler 1998] using a Shimadzu UV-2501 spectrophotometer equipped with a ISR-2200 internal integrating sphere. Discrete seawater samples were filtered under less than 10 mm mercury pressure using Whatman GF/F filter pads, which were placed at the entrance port of the sphere, and scanned from 350 nm to 750 nm using an air reference and baseline. In cases where filters could not be read immediately they were stored frozen in liquid nitrogen. Blank filter pads were prepared by filtering several hundred ml of Milli-Q water through fresh GF/F filters, which were then read in the same manner as the samples. Filtration volumes were adjusted to maintain a large amount of material on the filter while avoiding excessive clogging, and varied between 2 l and 0.1 l. Absorption coefficients were calculated using the pathlength amplification factor of Roesler [1998] assuming a null point correction at 750 nm. Detrital measurements were made using methanol extraction on the filter, followed by re-reading in the spectrophotometer [Kishino *et al.* 1985]. Phytoplankton absorption $a_\phi(\lambda)$ data were then obtained by subtraction of detrital absorption $a_d(\lambda)$ from total particulate absorption $a_p(\lambda)$.

A different method was adopted on the BenCal cruise, necessitated by the collaborative involvement of several research groups. Particulate absorption measurements were made using a LI-COR LI-1800 UW modular spectroradiometer equipped with an 1800-12 external integrating sphere [see Barlow *et al.* 2003]. Whilst similar measurement protocols were followed in the main, a different pathlength amplification factor was employed [Mitchell and Kiefer 1988], and detrital absorption was estimated through the numerical techniques of Bricaud and Stramski [1990].

5.2.3 Gelbstoff Absorption

Samples were prepared by filtering discrete water samples through GF/F filter papers under less than 10 mm mercury pressure, using stainless steel filter frits. Absorbance measurements were made using a Shimadzu UV-2501 spectrophotometer equipped with 10 cm pathlength matched quartz cuvettes. BDH Lichrosolv HPLC grade water was used as a pure water reference. Absorption coefficients were calculated as by Mueller & Austin [1995], with a null absorption point set to 750 nm.

5.2.4 Particle Size Distributions (PSD)

Particle size measurements were made using a 128 channel Coulter Multisizer II with either a 50 µm or 140 µm aperture in manometer mode, using freshly prepared 0.2 µm filtered seawater as both blank and electrolyte. Polydispersed algal particle size distributions are described by the effective diameter d_{eff} [Hansen & Travis 1974, Ahn *et al.* 1992] as given by:

$$d_{eff} = \frac{\int_{1}^{100} \frac{\pi}{4} d^3 F(d) d(d)}{\int_{1}^{100} \frac{\pi}{4} d^2 F(d) d(d)} \qquad (5.1)$$

where d is the particle diameter, and $F(d)d(d)$ is the number of particles per unit volume in the size range $d \pm \frac{1}{2} d(d)$.

5.2.5 Pigments

Pigments were analysed using High Performance Liquid Chromatography (HPLC). Seawater was filtered through 25 mm GF/F filters and filters stored frozen in liquid nitrogen until analysis. Filtration volumes were adjusted to maintain approximately constant amounts of material on the filter and ranged from 0.1 l to 2 l. Pigments were extracted in acetone, containing *trans*-β-apo-8'-carotenal internal standard, with the aid of ultrasonication and clarified by centrifugation. Analysis of pigments followed the reverse phase HPLC procedure outlined by Barlow *et al.* [1997] using a 3 µm Hypersil MOS2 C8 column (100 x 4.6 mm), a Varian ProStar pump, a Thermo Separations AS3000 autosampler, a Thermo Separations UV6000 diode array absorbance detector, and ChromQuest chromatography software. Pigments were detected at 440 and 665 nm, identified by retention time and on-line diode array spectra, and quantified relative to the internal standard. Chlorophyll *a* standard and *trans*-β-apo-8'-carotenal were obtained from Sigma-Aldrich Ltd. Other pigment standards were purchased from the DHI Institute for Water and Environment, Denmark. Slight variations in the method were employed for pigment analyses from the BenCal cruise [see Barlow *et al.* 2003].

5.3 Optical theory & Model Development

The reflectance approximation, commonly used for reflectance inversion algorithms [Roesler & Perry 1995, Garver & Siegel 1997, Roesler & Boss 2003] expresses the light leaving the sea surface in terms of the absorption and backscattering properties of the water column. Using remote sensing reflectance R_{rs} [Zaneveld 1995]

$$R_{rs} = \frac{L_u(0^+,\lambda)}{E_d(0^-,\lambda)} = \frac{f}{Q}\frac{b_b(\lambda)}{a(\lambda)+b_b(\lambda)} \qquad (5.2)$$

where $L_u(0^+,\lambda)$ is the upwelling radiance just above the sea surface, $E_d(0^+,\lambda)$ is the downwelling irradiance just above the sea surface, f/Q is a shape factor describing the angular structure of the light field [Zaneveld 1995, Morel *et al.* 2002], $a(\lambda)$ is the total absorption coefficient, and $b_b(\lambda)$ is the total backscattering coefficient. It is thus possible to relate the absorption and backscattering coefficients in the upper optical depths [Gordon & Mcluney 1975] to measurements of the upwelling radiance and downwelling irradiance.

The total absorption and backscattering coefficients are the summed total respective coefficients of the principal optical constituents of the water column; considered to be phytoplankton, coloured dissolved compounds (here referred to as gelbstoff), particulate biological breakdown products otherwise known as detritus, other small particles generally considered to have a ubiquitous presence in the sea, such as lithogenic material or bacteria, and the seawater itself.

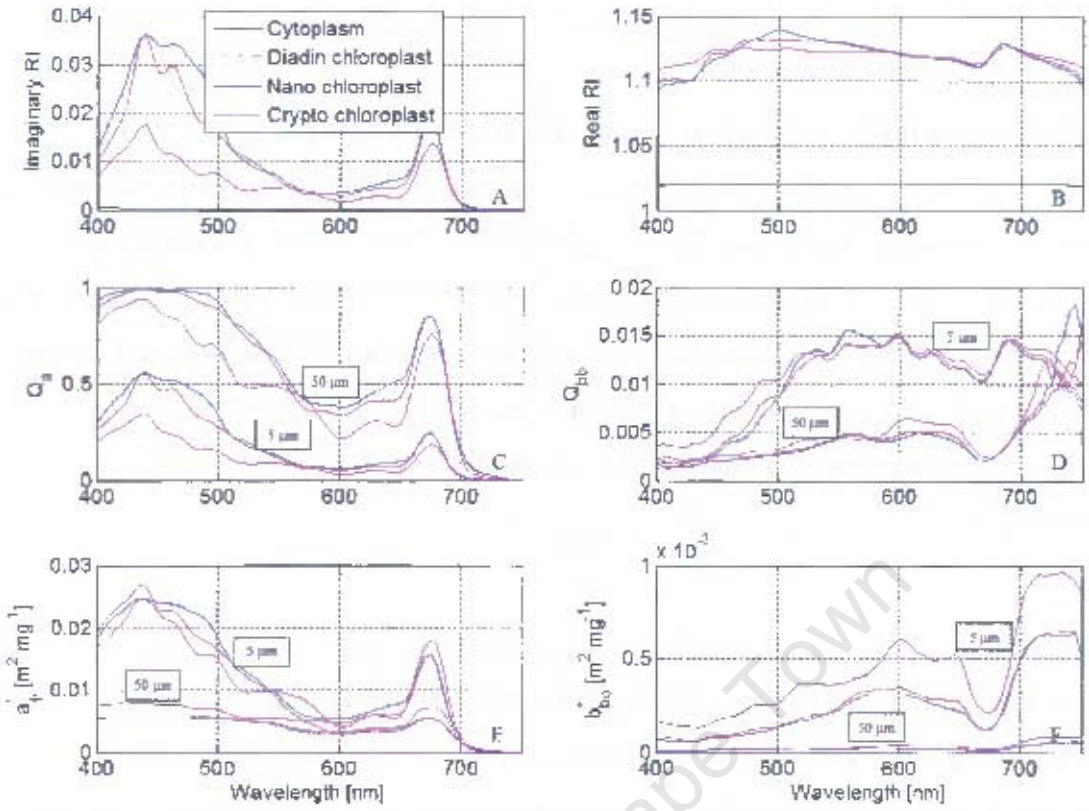

Figure 5.1 Input data and examples of absorption and backscattering data for the three algal groups used as basis vectors. A) Cytoplasm and chloroplast imaginary refractive index data, B) Cytoplasm and chloroplast real refractive index data, C) Example absorption efficiency factor spectra at 5 µm and 50 µm for the three algal groups, D) Example backscattering efficiency factor spectra at 5 µm and 50 µm, E) Example Chl *a*-specific algal absorption spectra for typical size distributions at effective diameters of 5 µm and 50 µm, F) Example Chl *a*-specific algal backscattering spectra for typical size distributions at effective diameters of 5 µm and 50 µm.

5.3.1 Phytoplankton Absorption and Backscattering Coefficients

Earlier sections of this study have demonstrated the feasibility of representing the optical properties of complex phytoplankton size distributions with simple Standard distributions [Hansen & Travis 1974], providing the effective diameter and total particle surface area are equivalent. In addition, particle optic models using a two-layered spherical geometry have been shown to provide reasonable approximations to the absorbing and backscattering properties of phytoplankton populations, based on reflectance comparisons.

The algorithm uses absorption and backscattering data for three algal groups – Chl *b* containing nanoflagellates and Chlorophytes, fucoxanthin/peridinin containing diatoms and dinoflagellates, and alloxanthin/phycoerythrin containing Cryptophytes (or organisms associated with Cryptophyte endosymbionts such as *Mesodinium rubrum)*. The three groups are chosen as representative of the major algal classes in upwelling systems [Hutchings *et al.* 1994], and will be referred to as the *nano, diadin* and *crypo* groups, repectively. In addition the three groups potentially allow the calculation of the two accessory pigment groups (Chl *b* and Allo) shown to be quantifiable from absorption spectral mixture models [Chapter 3]. Refractive index data representative of these three algal groups (Figure 5.1) are derived from field measurements of absorption and particle size distributions, based on a two-layered geometry with a peripheral chloroplast layer set to 20 % of total cell volume [Chapters 2 - 4]. Absorption (Q_a) and backscattering (Q_{bb}) efficiency factors for size ranges of the three algal groups from 1 μm to 100 μm diameter are then generated using these refractive index data. These pre-computed efficiency factors are used by the algorithm to calculate the phytoplankton absorption coefficient and backscattering coefficients using an admixture of the three algal groups as given by:

$$a_\phi = \mathrm{Chl}\, a\,(\pi/4)\int \sum_{n=3} (P_n Q_{an}) F^*(d) d^2\, d(d) \qquad (5.3)$$

and

$$b_{b\phi} = \mathrm{Chl}\, a\,(\pi/4)\int \sum_{n=3} (P_n Q_{bbn}) F^*(d) d^2\, d(d) \qquad (5.4)$$

where $F^*(d)$ is the Chl a specific size distribution (see Equation 5.9) and the solvable unknowns P_n represent the normalised scaling parameter ($0 \leq P_n \leq 1$) for a single vector in the admixture such that:

$$\sum_{n=1 \text{ to } 3} P_n = 1 \tag{5.5}$$

Sample absorption and backscattering efficiency factors and volume coefficients can be seen in Figure 5.1. Relative accessory pigment concentrations, to be used as chemotaxonomic markers, are calculated through a mean pigment suite admixture $\overline{ps}$, where:

$$\overline{ps} = P_1\overline{ps}_1 + P_2\overline{ps}_2 + P_3\overline{ps}_3 \tag{5.6}$$

and ps_n represents a vector of measured accessory pigment concentrations associated with each algal group. The particle size distribution in Equation 5.3 is given by a Standard size distribution [Hansen & Travis 1974, Chapter 2]:

$$F(d) = ASF\left(\frac{d}{2}\right)^{\left[(1-3v_{eff})/v_{eff}\right]} \exp\left[\left(\frac{d}{2}\right)\Big/\left(\frac{d_{eff}}{2}v_{eff}\right)\right] \tag{5.7}$$

where the effective diameter d_{eff} is a solvable unknown, ASF is an arbitrary scaling parameter, and a constant effective variance of v_{eff}=0.6 is used [Chapter 2]. The total relative particle volume volume $\bar{V}$ of this distribution can then be calculated with:

$$\bar{V} = \frac{\pi}{6}\int F(d)d^3 d(d) \tag{5.8}$$

and the initial distribution $F(d)$ is scaled to a Chl a specific size distribution $F^*(d)$ for use in Equations 5.3 and 5.4 with:

$$F^*(d) = \frac{F(d)}{\overline{V}\, c_i} \qquad (5.9)$$

The phytoplankton absorption and backscattering efficiency factors are thus explicitly dependent upon the spectral refractive index data, two-layered geometry parameters, and the c_i values employed for each algal group. These c_i values were set to 3.5 kg m^{-3} (*diadin* and *nano* groups) and 2.5 kg m^{-3} (*crypto*), considered representative values for each group based upon analysis of previous field measurements [Chapter 3]. Phytoplankton absorption and backscattering coefficients are in turn further explicitly dependent on the Chl *a* concentration, effective diameter, and the fractional component of the three algal groups as given by the P_n parameters – these five parameters being explicitly solved for by the reflectance algorithm.

5.3.2 Absorption and Backscattering Coefficients of Other Constituents

Gelbstoff and detritus absorption spectra typically display similar exponential spectral shapes [Bricaud *et al.* 1981, Roesler *et al.* 1989] and their combined absorption is represented by an exponential shape function [e.g. Roesler & Perry 1995]:

$$a_{gd}(\lambda) = a_{gd}(400)\exp[-S(\lambda - 400)] \qquad (5.10)$$

where $a_{gd}(400)$ is explicitly solved for. The exponential slope factor S is taken as a constant of 0.012, determined as a typical combined value for the southern Benguela [Bernard 1996, unpublished data].

Backscattering by small particles b_{bs}, e.g. detrital, bacterial or lithogenic particles, is represented by a power law following a $\lambda^{-1.2}$ relationship [Roesler & Perry 1995], employing an explicitly solved scaling parameter. The absorption of seawater is given by the data of Pope & Fry [1997], whilst the backscattering of seawater is given by the data of Morel [1974].

5.3.3 Bidirectional Reflectance Considerations

The bidirectional character of the upwelling light field in the sea is well known, and is described in the reflectance approximation (Equation 5.2) by the combined parameter f/Q [Zaneveld 1995, Morel *et al.* 2002]. It is known that this parameter is dependent upon the inherent optical properties of surface waters, most importantly the phase function and backscattering efficiency [Morel & Maritorena 2001], and other factors influencing the angular structure of the radiative field, such as solar zenith angle and surface roughness [Morel *et al.* 2002, Albert & Mobley 2003]. There is thus a need for analytical reflectance models to account for variability in the f/Q parameter, as acknowledged in previous model formulations [Roesler & Boss 2003]. The most sophisticated formulation available to estimate systematic variability in the f/Q parameter is that of Morel *et al.* [2002], obtained through radiative transfer simulations employing phase functions allowing a variable backscattering efficiency. The spectral formulation is explicitly dependent upon both the Chl a concentration and the solar zenith angle, and the look-up tables provided by Morel *et al.* [2002] are used here for f/Q estimation. Somewhat coarse adaptations are necessarily made for the change of application: the original data (available at seven wavelengths) are linearly interpolated to a 5 nm resolution for hyperspectral use, and the data for Chl a = 10 mg m^{-3} are used where model estimated Chl a values are larger than this. Solar zenith angles are calculated from position, date and time using the algorithm of Reda and Andreas (2003).

5.3.4 Propagation of Upwelling Radiance

In practice, in-water reflectance measurements require that the upwelling radiance metity is necessarily made at some nominal depth below the surface, requiring the further use of a propagation scheme to describe the attenuation of upwelled radiance as it is propagated to the surface. The diffuse attenuation coefficient for upwelling radiance K_u is dependent upon the total absorption and backscattering coefficients, and solar zenith angle θ_s, using the formulation of Albert & Mobley [2003]:

$$K_u = (a + b_b)\left[1 + \left(\frac{b_b}{a + b_b}\right)\right]^{3.452}\left(1 - \frac{0.2786}{\cos\theta_s}\right) \qquad (5.11)$$

5.3.5 Final Model Formulation

Given that the diffuse attenuation coefficient for upwelling radiance can be also expressed in terms of the solvable absorption and backscattering coefficients, Equation 5.2 can be reformulated to explicitly solve for the upwelling radiance L_u measured at depth z whilst maintaining the integrity of the reflectance approximation:

$$L_u(z,\lambda)=\frac{f}{Q}\frac{\eta^2}{\tau}\frac{b_b(\lambda)}{a(\lambda)+b_b(\lambda)}\frac{E_d(\lambda)}{\exp(-K_u(\lambda)z)} \qquad (5.12)$$

where η/τ is an assumed constant (=1.3612) describing the upwelling radiance transmittance across the air-sea interface, and other notation is as previously described.

The model can be summarised as follows. Inputs are: measured hyperspectral upwelling subsurface radiance ($L_u(z,\lambda)$, μw cm^{-2} nm^{-1} sr^{-1}) and above surface downwelling irradiance ($E_d(0+,\lambda)$, μw cm^{-2} nm^{-1}). The model uses seven solvable unknowns: Chl *a* concentration (mg m^{-3}), algal effective diameter (d_{eff}, μm), the relative concentration of the three algal groups ($0< P_n < 1$, n=1 to 3), combined gelbstoff and detrital absorption (e.g. $a_{gd}(400)$, m^{-1}), and small particle backscattering (e.g. $b_{bs}(550)$, m^{-1}). Algal optical properties for the three groups are calculated assuming constant group-specific and size-independent chloroplast and cytoplasm refractive indices, chloroplast volumes of 20 %, and c_i values. Gelbstoff/detrital absorption and small particle backscattering employ constant spectral shapes and variable magnitude.

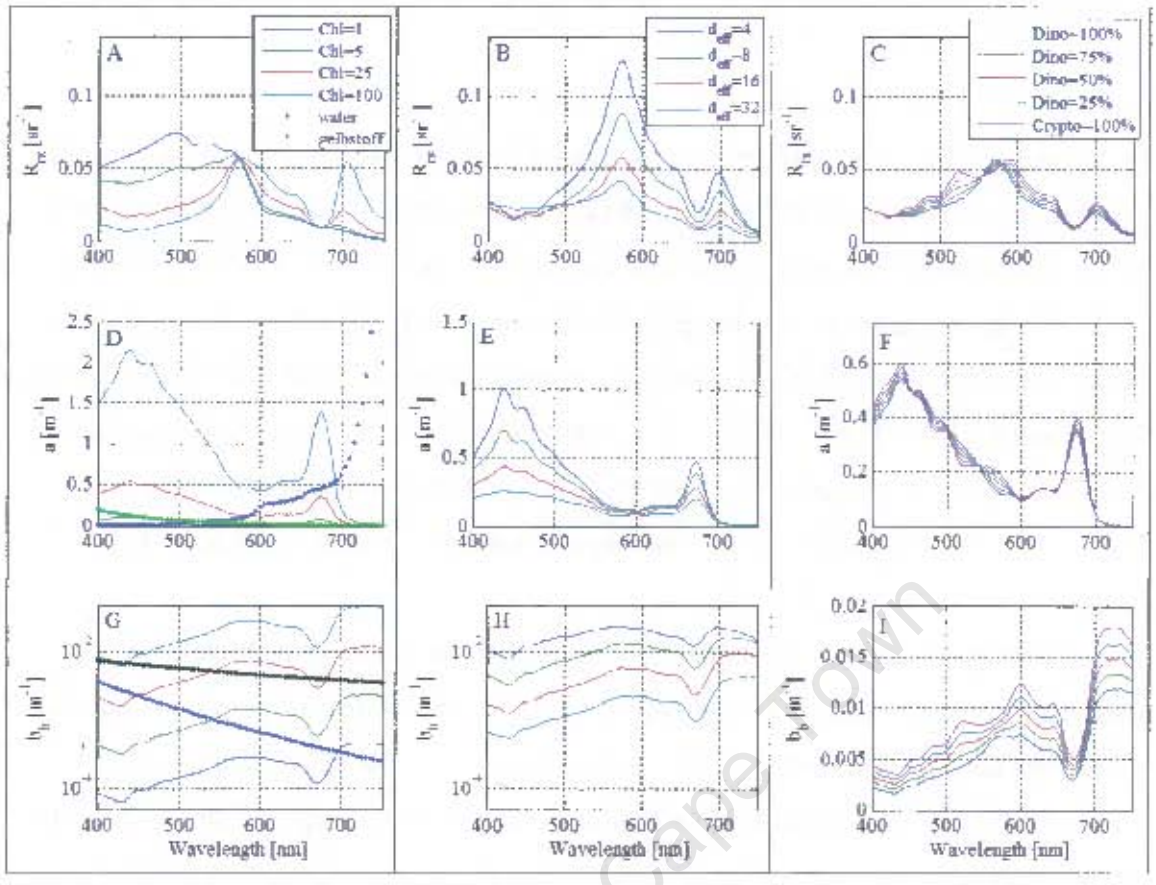

Figure 5.2 Simulated reflectance, absorption and backscattering using the reflectance model in a forward mode. The effects of increasing Chl *a* concentration are shown for A) reflectance, D) absorption, and G) backscattering, using a hypothetical *diadin* population with d_{eff}=16 μm. The effects of changing algal assemblage size are shown for B) reflectance, E) absorption, and H) backscattering, using a hypothetical *diadin* population with Chl *a* =25 mg m^{-3}. The effects of changing accessory pigmentation are shown for C) reflectance, F) absorption, and I) backscattering, using a variable admixture of the *diadin* and *crypto* basis vectors, at Chl *a*=25 mg m^{-3} and d_{eff}=16 μm. For all simulations constant values of a_g(400)=0.2 m^{-1} and b_{bs}(550)=0.005 m^{-1} were used, in conjunction with the a_g and b_{bs} spectral shapes discussed above.

The model employs a Simplex solution method [Nelder & Mead 1965], using constant initial values, and is coded in Matlab R14 (The Mathworks). As the model specifically does not account for sun induced natural fluorescence [Babin *et al.* 1996, Maritorena *et al.* 2000], the convergence weighting for the Nelder-Mead solution is set to negligible values between 665 and 715 nm the spectral region likely to be affected by natural algal fluorescence [*ibid.*]. The model thus does not seek to match spectral reflectance values at these fluorescence wavelengths, and in effect offers a means of discriminating fluorescence effects, as have earlier models of a similar nature [Roesler & Perry 1995].

The sensitivity of the model to changes in algal biomass, effective diameter and assemblage type is demonstrated in Figure 5.2, using the model in a forward simulation mode. The lack of simulated algal fluorescence is apparent in the reflectance spectra (Figures 5.2A to 5.2C), with close to minimal values at ~ 683 nm, typically given as the fluorescence peak wavelength [Babin *et al.* 1996, Maritorena *et al.* 2000]. Increases in algal biomass (Figures 5.2A, D, G) demonstrate the change from low biomass waters with high reflectance at blue wavelengths (due to the dominant optical effects of the water), to high biomass waters with high red reflectance (due to the dominant optical effects of the algae).

Figures 5.2B, E and H show the profound effects that changes in algal size can have on reflectance values in high biomass waters (Chl a=25 mg m^{-3}), at least considering the theoretical paradigm of this study. Reflectance values from waters dominated by small cells display very different spectral shapes to waters dominated by large cells: the effects of enhanced algal backscattering and Soret peak absorption by small cells lead to greatly enhanced reflectance values at longer wavelengths. In contrast large cells, with algal backscattering values typically an order of magnitude lower and greatly flattened Soret peak absorption values, result in much lower, flatter reflectance spectra.

Reflectance variability associated with changes in accessory pigmentation (Figures 5.2C, F and I), whilst distinct, appear relatively small in contrast to size induced changes. As the algal light harvesting pigment system changes from carotenoid- to phycobiliprotein-

dominated (*diadin* to *crypto*), the primary reflectance peak is shifted to a longer wavelength (~570 nm to ~590 nm) and a peak appears at ~ 525 nm.The effects of changes in c_i can also be discerned (*diadin* c_i=3.5 kg m^{-3} vs. *crypto* c_i=2.5 kg m^{-3}), with the *crypto* assemblage demonstrating higher absorption at the Soret and red peaks, and higher backscattering values. Whilst the size and accessory pigment related changes shown in Figure 5.2 represent somewhat extreme cases of comparison, they demonstrate that the primary solution variables of the reflectance model with regard to algae (biomass, size and accessory pigment complement) can be considered causal to reflectance variability in algal dominated waters.

5.4 Results

5.4.1 Reflectance Simulation

The model was able to closely simulate either measured upwelling radiance or remote-sensing reflectance R_{rs} through a wide range of water types, with Chl *a* values ranging from 0.24 mg m^{-3} to 309 mg m^{-3}. Further discussion of algorithm performance will be concerned solely with R_{rs} data – whilst the algorithm is mathematically manipulated to solve for upwelling radiance, it is the reflectance approximation and R_{rs} data that are the core of the model. Examples of the ability of the model to closely simulate reflectance data from a diverse range of water types (with associated predictions for absorption and backscattering) are shown in Figure 5.3.

A closer examination of model simulated spectral reflectance can be seen in Figure 5.4D, showing the r^2, standard error of prediction (SEP), and linear least-squares slope values of predicted vs. measured reflectance. A noticeable feature is the poor simulation in the natural fluorescence spectral range, centred at ~ 683 nm and extending from 660 nm to 700 nm – this is entirely expected as the model has no ability to simulate this fluorescence (also see Figure 5.3A to C). This narrow band of relatively low r^2, high SEP and lowered slope values, coincident with sun induced fluorescence emission spectra [Babin *et al.* 1996], are an indication that the spectral weighting procedures used by the model to avoid fluorescence aliasing are appropriate.

The model appears to perform relatively poorly at long wavelengths i.e. > 720 nm, probably due to two factors (Fig. 5.4A). Firstly, reflectance values at these red wavelengths are typically low e.g. $< 5 \times 10^{-4}$ sr^{-1}, leading to lower signal:noise ratios and enhanced errors in prediction. Secondly, phytoplankton absorption and backscattering are somewhat poorly characterised at these wavelengths, primarily due to uncertainties regarding the typically low values of cellular material absorption. As discussed in Chapter 4 with regard to these wavelengths: algal backscattering is highly dependent upon the absorbing properties of the cellular assemblage, low algal absorption leads to

As regards the prediction of relative accessory pigment concentrations (Fig. 5.4F), the model was only able to predict the Allo/Chl *a* ratio with success (r^2=0.64, SEP= 42 %, n=36), with an offset resulting from the non-zero Allo concentrations of the pigment basis vectors used in the model (y=0.52x + 0.04). The elevated Allo ratios in the data set employed here are associated with the ciliate *Mesodinium rubrum*, and whilst it is unlikely that the direct effects of Allo are causal to detection (see discussion in Chapter 2), there is no doubt that the model is effectively distinguishing waters with elevated concentrations of this organism.

The limited ability of the model as concerns the prediction of Chl *b* and other accessory pigments (data not shown) is consistent with the findings of Chapter 2, and a result of causality; only significant spectral changes to absorption and backscattering, associated with large changes in assemblage structure, are likely to be detected. The models lack of ability to detect changes in the relative Chl *b* concentration (*cf.* Chapter 2) is also possibly a function of the test data set used: Chl *b* containing organisms only form at most a minor assemblage component (maximum Chl *b*: Chl *a* ratio=0.14). In addition, it is only relatively low biomass waters that show even these moderately elevated Chl *b* concentrations (Chl *a*<3.6 mg m^{-3}), and the model is unlikely to be able to distinguish subtle spectral changes in algal optical properties when the algal contribution to the total reflectance signal is relatively small.

clarity. The ability of the model to closely simulate reflectance, whilst accurately predicting algal absorption and intracellular descriptors, can be used to argue that the backscattering values predicted by the model (and the scattering model used to provide these) are approximately correct. Further discussion of the modelled backscattering predictions, in comparison to previously published backscattering parameterisations, are presented below.

5.4.3 Prediction of Algal Descriptors

Detailed quantitative analyses of model performance, using bootstrapping analyses (1000 replicates) to generate all statistical data, are shown in Figure 5.4. Prediction of Chl *a* concentrations (Fig. 5.4D)was extremely good (r^2=0.98, standard error of prediction (SEP)=29 %, n=42), through a dynamic range of over three decades and with little bias (y=0.91x).

The model also showed the ability to detect the effective diameter (Fig. 5.4E) of the algal assemblage d_{eff} (r^2=0.67, SEP= 47 %, n=42), although with a systematic bias towards over-prediction (y=1.39x). The over-prediction of algal size is likely to result at least in part from the assumptions necessarily employed by the algal IOP parameterisations in the model; specifically the assumption of constant c_i values for the three algal groups represented. Whilst it is known that this assumption is a considerable simplification (Fig. 3.1), it is necessary in the context of the model: the effects of variations in c_i and effective diameter upon absorption are somewhat similar, and the model effectively ascribes this variability to effective diameter in order to allow size related predictions (cf. Chapter 2). This allows a reasonable prediction of the changes in an algal size parameter from reflectance data, with the important caveat that assemblage c_i values must remain reasonably constant, e.g. the unlikely switch to a heterotroph dominated community [Pitcher *et al.* 1998] with considerably lower c_i values could introduce significant errors in size prediction. It is considered inappropriate to use the reflectance model to gain absolute algal size data: the effective diameter product should rather be used to assess whether the relative size of the algal community has changed, e.g. the shift to domination by large celled dinoflagellate species through a data time series.

5.4.2 Prediction of Inherent Optical Properties

Performance of the model with regard to spectral algal absorption is shown in Figure 5.4B, with synopses in Table 5.2 and examples in Figure 5.3. Algal absorption coefficients were in general well predicted by the model, with spectral r^2 values of 0.84 to 0.94 and SEP values of 34 % to 55 %, between 400 and 700 nm. The rather flat spectral r^2 and SEP values indicate that there is little spectral bias in the $a_\phi(\lambda)$ predictions. The good comparison between the mean absolute deviations of measured and predicted algal absorption suggest that predicted algal absorption coefficients fall within a suitable range. Algal absorption is also an important intermediate variable with regard to Chl *a*, assemblage size, and accessory pigment prediction, and the generally good predictions of both algal absorption and these parameters (see below) indicate that the two-layered equivalent size distribution absorption parameterisation employed by the model is appropriate.

The ability of the model to predict variations in the combined gelbstoff and detrital absorption coefficient is limited, with maximal r^2 values of 0.1 and minimal SEP values of 48 % (Fig. 5.4C). However, the contribution of gelbstoff and detritus to the total absorption coefficient is relatively small, with the mean absolute deviation of measured $a_{gd}(440)$ values approximately four times smaller than that of $a_\phi(440)$. This relatively small non-algal absorption component is typical of the southern Benguela system, which is productive, dynamic and has little terrigenous input [Bernard 1996, unpublished data]. The inability of the reflectance model to predict variations in what is effectively a relatively small modifier of the submarine light field is therefore not wholly negative, as can be seen by the good comparison of the mean absolute deviations of measured and predicted a_{gd} values (Table 5.2).

The lack of independently measured backscattering data did not allow a direct analysis of the model's ability to predict the backscattering coefficient. Whilst independent data from the Hydroscat-6 (Hobilabs, Tucson, Arizona) were available for samples from the BenCal cruise [Barlow *et al.* 2003], there are considerable uncertainties associated with these data - in the author's opinion introduction of such data would lend more obfuscation than

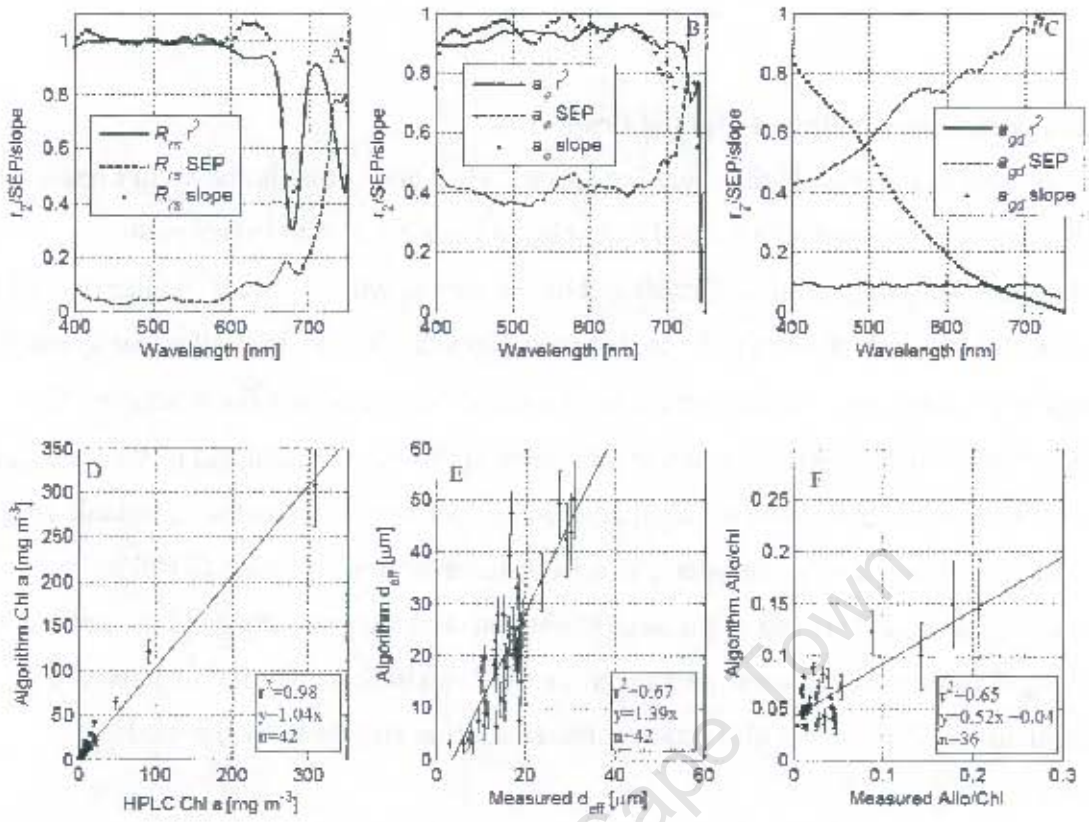

Figure 5.4 Algorithm performance, given by r^2, standard error of prediction (SEP), and linear slope values, with regard to: A) spectral remote sensing reflectance $R_{rs}(\lambda)$, B) spectral phytoplankton absorption $a_\phi(\lambda)$, C) spectral combined gelbstoff/detrital absorption $a_{gd}(\lambda)$, D) Chl *a* concentration, E) effective diameter d_{eff}, and F) the Allo/Chl *a* ratio.

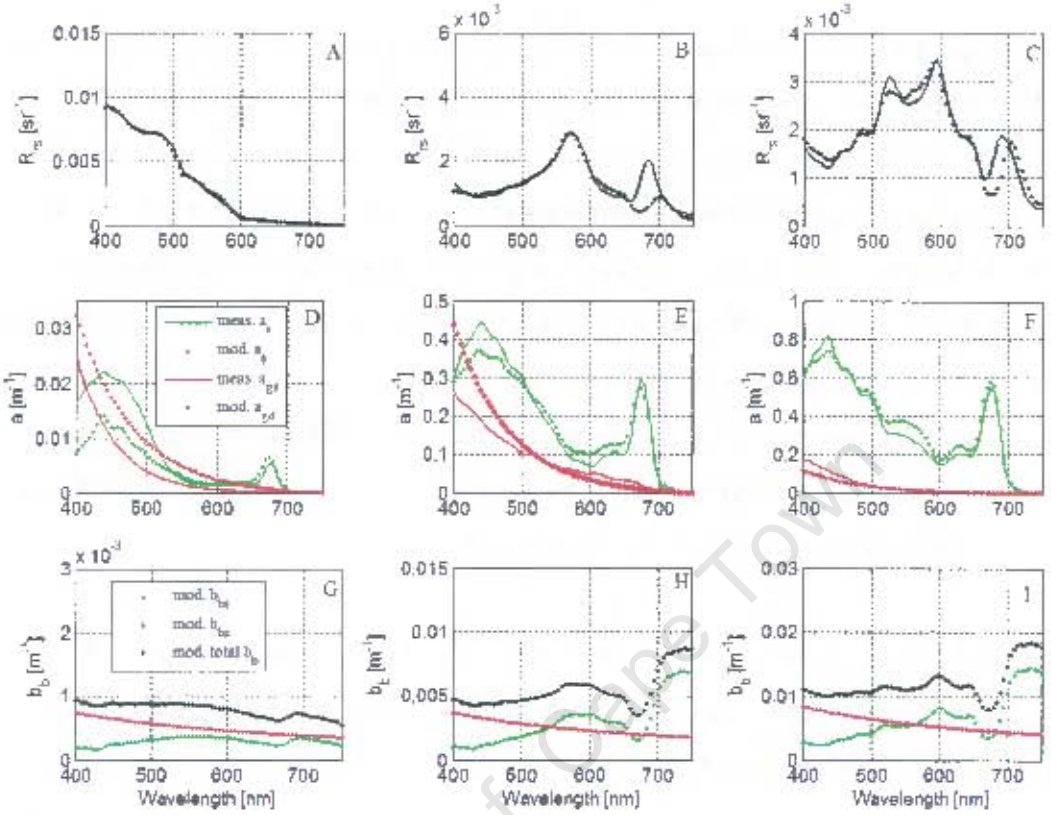

Figure 5.3 Example reflectance model matches and IOP results for a range of water types. A) reflectance, D) absorption, and G) backscattering for low biomass flagellate dominated waters (measured Chl *a*=0.24 mg m^{-3}); B) reflectance, E) absorption, and H) backscattering for intermediate biomass diatom dominated waters (measured Chl *a*=20.9 mg m^{-3}); and C) reflectance, F) absorption, and I)backscattering for high biomass *Mesodinium rubrum* dominated waters (measured Chl *a*=49.3 mg m^{-3}). Note the distinct natural fluorescence peaks unmatched by the model in B and C, the generally good match between measured and modelled absorption values, and the variability in the spectral shape of the total particulate backscattering coefficients. In all cases lines represent measured data whilst dots represent modelled data.

low precision of absorption measurements and subsequent IOP parameterisation, and ultimately low confidence in the model backscattering values in this spectral region.

Finally, Figure 5.4A shows that the slope values of the predicted vs. measured reflectance are elevated by ~ 10 % in a band centered at ~630 nm. This feature indicates that reflectance simulation is less good in this spectral region; an area influenced by the minor absorption peaks of the chlorophyll pigments [Stuart *et al.* 1998]. It is likely that this region of elevated uncertainty is due to the algal IOP parameterisations employed by the model. Whether this is manifest through absorption, backscattering or some combination of these is unclear. Chapter 3 indicates that the absorption size/pigment related decoupling, made possible in theory through simulation of the package effect, is somewhat incomplete at these wavelengths (Figure 3.2A) – such a phenomenon could lead to the reflectance simulation feature under discussion.

Table 5.2 Analysis of model performance: r^2, standard error of prediction (SEP, %), slope, intercept, mean absolute deviation (MAD), and number of samples for algal descriptors and absorption coefficients

Variable	r^2	SEP (%)	Slope	Intercept	MAD measured	MAD predicted	No. Samples
Chl *a*	0.98	29	1.04	0	19.5	20	42
d_{eff}	0.67	47	1.39	0	4.6	10.7	42
Allo/Chl *a*	0.65	45	0.52	0.04	0.028	0.024	36
$a_{\phi}(440)$	0.89	42	0.92	0	0.26	0.24	42
$a_{gd}(400)$	0.1	48	0.86	0	0.069	0.058	42

5.5 Discussion: a Perspective on Marine Backscattering

An improved understanding of the contribution of algal backscattering to total backscattering in surface waters is crucial to the ability to analytically express ocean colour. Whilst there are no independent measurements of backscattering with which to assess the validity of the algorithm backscattering estimates presented here, it can be argued that these estimates are reasonable, considering the good performance of the algorithm with regard to simulation of reflectance and prediction of absorption parameters. An examination of the backscattering data returned by the algorithm may therefore be useful in attempting to gain a broader understanding of what can still be regarded as a poorly understood inherent optical property [Morel & Maritorena 2001, Stramski *et al.* 2004].

Figure 5.6A shows that the magnitude of the backscattering values returned by the algorithm are in approximate agreement with the models of Morel & Maritorena [2001] and Gordon *et al.* [1988], referred to as MM01 and G88 respectively. There is, however, considerable scatter of the algorithm returned data around the MM01 and G88 parameterisations, due to both the varying presence of non-algal particles and the substantial spectral shape the algorithm assigns to the backscattering spectra (Fig. 5.7). Such scatter has been observed previously in the backscattering probability data presented by Twardowski *et al.* [2001], referred to as TW01.

It is also possible to analyse algorithm returned backscattering in terms of backscattering probability $\tilde{b}_b$, making the assumption that the non-algal $\tilde{b}_b$ data have a spectrally invariant value of 1% - the maximal value suggested by Morel & Maritorena [2001]. The algal component is based on a complete solution to the Aden-Kerker theory, and has a highly variable $\tilde{b}_b$ based on a full calculation of the volume scattering function. It would appear (Fig. 5.6B) that the algorithm $\tilde{b}_b$ values are only in agreement with MM01, G88 and TW01 at low Chl *a* values and at blue wavelengths, i.e. 435 nm.

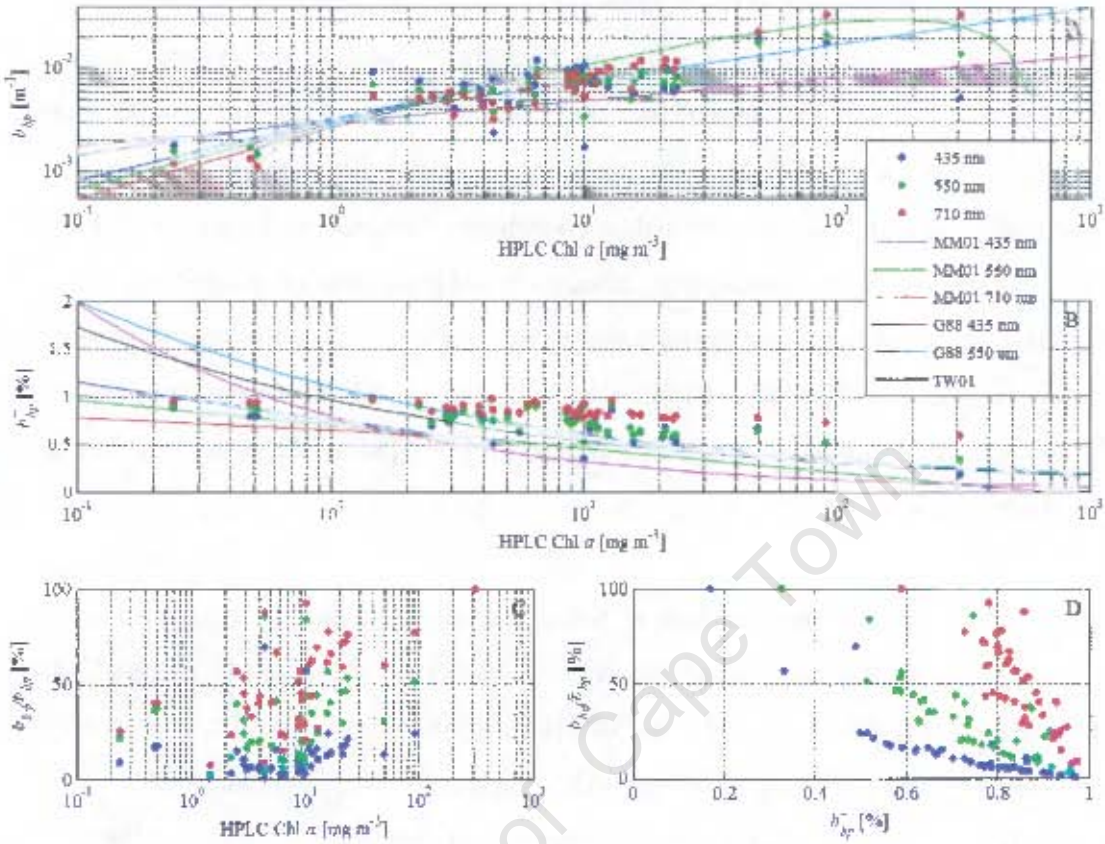

Figure 5.6 Analysis of backscattering parameters returned by the reflectance algorithm in comparison to published backscattering models - those of Morel & Maritorena [2001, Equation 13] (MM01), Gordon *et al.* 1988 (G88), and Twardowski *et al.* 2001. A) Particulate backscattering at 435, 550 and 710 nm vs. measured Chl *a* concentrations, from the algorithm (dots), MM01 and G88 (lines), B) Particulate backscattering probability in percent at the same wavelengths vs. measured Chl *a* concentrations, from the algorithm (dots), MM01, G88 and TW01 (lines), C) Percentage of particulate backscattering ascribed by the model to the algal component at the same wavelengths vs. measured Chl *a* concentrations, and D) Particulate backscattering probability in percent vs. the percentage of particulate backscattering ascribed to the algal component. Small particle backscattering as returned by the reflectance algorithm is ascribed a spectrally flat backscattering probability of 1 %, the maximal prescribed value of this parameter used by MM01.

At higher Chl *a* values (>3 mg m^{-3}), algorithm $\tilde{b}_b$ values are 30 % to 50 % higher than those from previous studies, particularly at longer wavelengths, and do not appear to decrease so sharply with increasing Chl *a* values. This is due largely to the considerable spectral shape the algorithm imparts to both the b_b and $\tilde{b}_b$ spectra (Fig. 5.7). In almost all cases the algal backscattering $b_{b\phi}$ and backscattering probability $\tilde{b}_{b\phi}$ spectra have maxima at red wavelengths, and in a majority of cases the fractional contribution by algae to the particulate backscattering is large enough to impart similar red maxima to the particulate backscattering b_{bp} and backscattering probability $\tilde{b}_{bp}$ spectra (Figures 5.6C and D, Figures 5.7B and D). Algorithm algal backscattering probability values range from ~ 0.2 % to ~0.9 % and are considerably influenced by cell size [Chapter 4]: in all cases algal $\tilde{b}_{b\phi}$ values are under the 1 % value assumed for the non-algal particulate.

The algal contribution to particulate backscattering is of considerable interest, particularly as this contribution has in the past been considered relatively minor [Stramksi & Kiefer 1991, Morel & Ahn 1991]. Again, assuming for the sake of argument that the algorithm backscattering returns are correct to first order, it appears that the algal contribution to backscattering is very much spectrally dependent (Figures 5.6C and D). At 435 nm (excluding two outliers) the algal contribution to particulate backscattering is relatively small through a wide range of Chl *a* concentrations (0.3 to 100 mg m^{-3}) : from negligible to 25 %. At 550 nm this contribution is raised to between ~5 % to 55 %, and at 710 nm the algal contribution is between 10 % and 90 % of the particulate backscattering. These algal contributions to backscattering are significantly higher than those proposed previously (Stramski & Kiefer 1991, Morel & Ahn 1991), and the possible reasons for this are explored below.

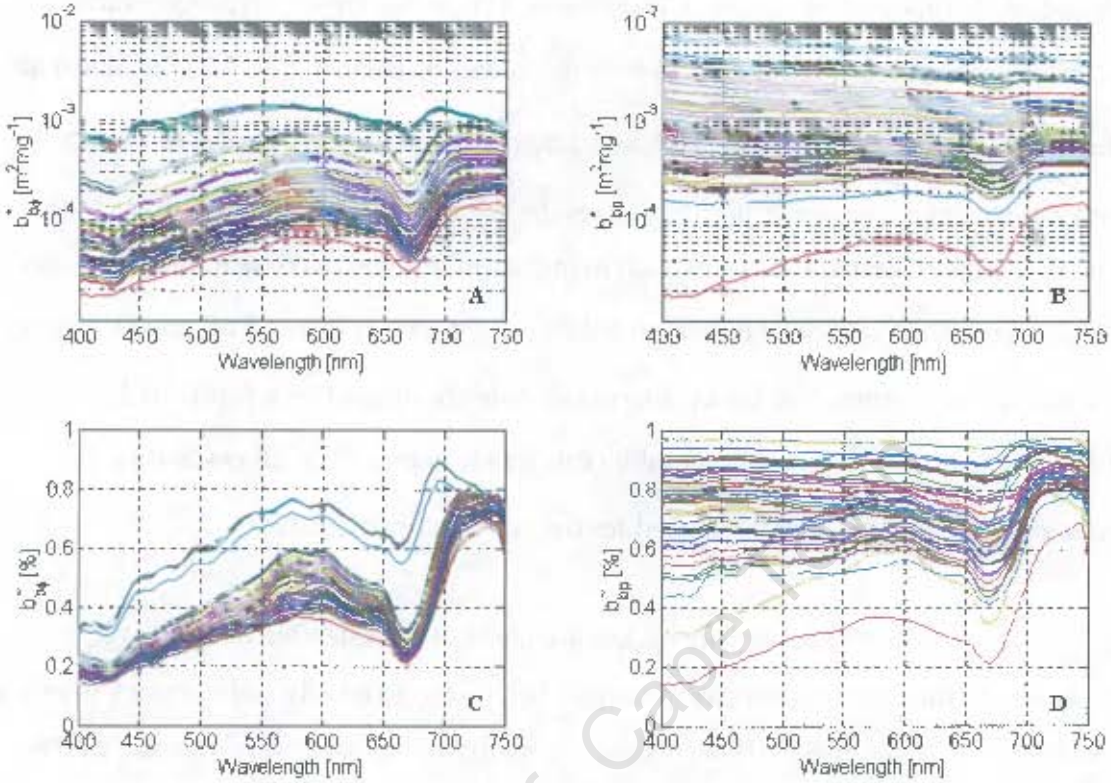

Figure 5.7. Returned algorithm backscattering data for A) Chl *a* specific algal backscattering, B) Chl *a* specific particulate backscattering, C) Algal backscattering probability in percent, and D) Particulate backscattering probability in percent. Small particle backscattering as returned by the reflectance algorithm is ascribed a spectrally flat backscattering probability of 1 %, the maximal prescribed value of this parameter used by MM01. Coloured lines are simply used to distinguish between samples.

Two conclusions can be drawn from these data. Firstly, the algorithm requires the presence of significant non-algal particulate to explain observed reflectance values, in accordance with much previous research [e.g. Morel & Ahn 1991, Morel & Maritorena 2001, Twardowski *et al.* 2001]. The simple backscattering shape assumed by the model to account for this poorly defined particle field ($b_{bs} = \lambda^{-1.2}$) does not allow further comment on the nature of these particles: they are likely to be a combination of organic detritus, bacterial cells and inorganic particulate of an aoelian nature [e.g Twardowski *et al.* 2001, Claustre & Maritorena 2003, Stramski *et al.* 2004]. Secondly, despite this need for the presence of a non-algal particle pool, the algal contribution to backscattering can be significant, particularly at red wavelengths where $b_{b\phi}$ values can be up to three times higher than at blue wavelengths.

The enhanced algal contribution to backscattering relative to previous work appears to have two main causes. The first of these is the avoidance of a Jungian type distribution, commonly assumed for oceanic waters [e.g. Stramski & Kiefer 1991, Morel & Maritorena 2001, Morel *et al.* 2002], to determine the relative proportion of both the algae and small non-algal particles. Such a distribution is not appropriate to the high biomass waters of the Benguela (cf. Chapter 2), and the formulation of the reflectance algorithm negates the need for this assumption. Algorithm results appear to show that even at relatively low biomass waters the non-algal contribution to particulate backscattering is highly variable (Fig. 5.6C), indicating the need for a greater knowledge of variability in the non-algal particle population [Twardowski *et al.* 2001, Morel *et al.* 2002, Stramski *et al.* 2004].

The second cause of the relatively elevated algal backscattering contribution results from the adoption of a two-layered geometry with complex spectral refractive index (in combination with Standard size distributions) to calculate all algal IOPs. Detailed discussion of the effects of this parameterisation are presented in Chapter 4: a general conclusion is that both Chl *a*-specific backscattering coefficients and probability values are enhanced by an order of magnitude relative to data resulting from homogeneous geometries [Stramski & Kiefer 1991, Morel & Ahn 1991, Twardowski *et al.* 2001]. An

additional effect of the spectral two-layered geometry is the considerable spectral variability in algal backscattering now observed, imparting in turn considerable spectral shape to the particulate backscattering parameters (Figures 5.6D and 5.7). This produces pronounced algal & particulate backscattering at red wavelengths: a phenomenon that would appear to be responsible for the red-brown colour of very high biomass "red tides" [Chapter 4]. Understanding this elevated red backscattering is thus extremely important to bio-optically based HAB applications, and it would appear to be due in part to the low imaginary refractive index values of phytoplankton at these wavelengths [Ahn *et al.* 1992, Chapter 4]. Further research is needed to better understand the potential impact of these low refractive index values on algal IOPS and thus ocean colour.

5.6 Conclusions

The inverse reflectance model presented here appears capable of simulating reflectance spectra from a wide variety of water types and algal biomass concentrations, allowing the model to accurately estimate absolute values of the algal absorption coefficient and Chl *a* concentrations. In addition the model appears capable of estimating relative changes in the effective diameter d_{eff} of the algal population, and the presence of phycoerythrin containing organisms through the relative alloxanthin concentration Allo. Estimates of these two algal descriptors are achieved through assumptions concerning the invariant behaviour of certain algal intracellular properties (as discussed below): it is suggested the the size and accessory pigment descriptors estimated by the model are more appropriate to assessing relative change in the algal assemblage rather than the estimation of absolute values. The model is designed for application to harmful algal bloom monitoring in the productive waters of the southern Benguela, and would appear to have considerable potential in determining core assemblage descriptors of a causal bio-optical nature from ocean colour data.

The model is based on the assumptions that 1) algal inherent optical properties may be accurately described through the use of a two-layered geometry in combination with

assumptions concerning intracellular variability and Standard size distributions, 2) the inherent optical properties of non-algal components are adequately described, and 3) the modified reflectance approximation described in Equation 5.12 may be used in a quantitative manner. The model has been developed and tested using independent data, and the model is essentially untuned in that only the choice of the refractive index basis vectors describing broad algal groups has been determined for regional application in upwelling systems. Algal intracellular variability has necessarily been constrained with chloroplast volume being assumed constant at 20 %, and algal c_i and refractive index values held invariant for each of the three algal groups represented. In addition, it is assumed that a Standard size distribution [Hansen & Travis 1974] of constant width and selectable effective diameter is able to simulate the optical properties of complex phytoplankton size distributions [Chapter 2]. These assumptions, and the use of a spectral mixing model employing an admixture of three algal groups, allow the quantifiable manipulation of near-surface algal absorption and backscattering in terms of assemblage size and accessory pigmentation. Further investigation of the validity of these assumptions is reliant upon the availability of intracellular morphological, pigment and refractive index data from an appropriately wide selection of algal assemblages. It must also be emphasized that the model structure shown here is specifically designed for application in a productive upwelling system, and application to other water types, e.g. oligotrophic systems, may require an alternative choice of basis algal groups and independent testing.

In addition to allowing a more detailed description of algal assemblage variability for ocean colour data, returned model data may allow some insight to the contribution of algae to particulate backscattering. The model indicates that the algal contribution to backscattering introduces considerable spectral shape, and is notably higher than previously thought, particularly at red wavelengths where algal backscattering is often maximal. This phenomenon highlights the importance of red wavelengths in high biomass ocean colour data, and the potential inclusion of these longer wavelength into ocean colour models may allow more accurate Chl *a* estimates at high concentrations of algal biomass. The importance of algal backscattering at red wavelengths again

emphasises the need for a greater knowledge of intra-cellular refractive index variability at the typcially weakly absorbing red wavelength regions, where even small variations in the intracellular imaginary refractive index can have a profound impact on backscatter. Backscattering data returned by the model has also highlighted the need for greater knowledge of the non-algal particulate pool which, in almost all cases other than extreme bloom events, make a significant if not major contribution to particulate backscattering [Stramksi *et al.* 2004].

Whilst the model has been designed for application to moored hyperspectral radiometric sensors, it can relatively simply be adapted for use with space-based ocean colour sensors. Requirements for this are: the provision of suitable geometrical factors to estimate coherent water leaving radiance data under different viewing configurations [Morel *et al.* 2002, Morel & Gentil 2004], and a reduction in the number of unknowns currently used by the model, most likely through reducing the number of algal groups employed in the spectral mixing model. Adaptation for space-based use would allow synoptic estimates of algal size and non-algal components, and potentially more accurate Chl *a* estimates in high biomass waters. Whilst the derivation of fluorescence parameters has not been examined here, similar previous models have demonstrated such an application [Roesler & Perry 1995], and there is considerable potential to utilise *in situ* and space-based fluorescence data for HAB detection [Gower *et al.* 1999] and as a physiological proxy [Young & Beardall 2003].

Chapter 6

Conclusions

The study has demonstrated that it is possible to quantitatively relate spectral reflectance data, through the absorption and backscattering coefficients, to the variables causal to algal inherent optical properties. This is made possible principally through the use of optical models employing a two-layered geometry, in conjunction with simply parameterised equivalent size distributions. The use of these constructs, in combination with spectral mixing models based on common algal groupings for upwelling systems, allows the derivation of algal biomass, an algal size descriptor, and coarse accessory pigment identification through a reflectance inversion algorithm. Whilst the reflectance algorithm and underlying optical models presented here are far from optimal, and specific to upwelling systems in their present forms, they represent the beginnings of a framework for fully analytical ocean colour models: utilising a unified theory to describe the entire suite of algal IOPs for a hypothetical algal population.

The adoption of a preliminary analytical framework for the interpretation and simulation of ocean colour has highlighted gaps in the current knowledge of algal cellular characteristics and related effects on algal IOPs. Such gaps must be addressed, not least with the aim of providing a truly robust reflectance inversion algorithm capable of operation in a wide variety of water types. A variable of considerable importance to algal optical properties and physiology is the Chl *a* concentration per cell volume or c_i (kg m^{-3}) [Morel & Bricaud 1981, Raven 1986]. The reflectance algorithm presented here has employed invariant c_i values for each of the three algal groups represented, as a necessary constraint for effective diameter prediction. These invariant c_i values have been employed in the absence of field data indicating a more appropriate parameterization (see discussions in Chapter 3.4). There is little doubt that a greater understanding of the c_i variability of natural algal assemblages, from allometric, broad taxonomic and physiological perspectives, is required: both to improve performance of the reflectance algorithm presented here, and to promote greater understanding of the processes underlying algal optical properties.

In a similar vein, this study has made somewhat simplistic assumptions concerning the morphometrics and intra-cellular refractive index variability of the algal cell, as a

necessary first step in adopting a two-layered geometry model for algal optical properties. Comprehensive validation of the two-layered model requires a greater understanding of cellular morphometrics from a systematic perspective. In addition, the study has shown that intracellular spectral refractive index variability has a considerable effect on backscattering, particularly so when the imaginary refractive index is very small, e.g. at red wavelengths. Greater knowledge is thus required of the refractive index of cellular organelles, in particular the chloroplasts as the major source of variability in both the real and imaginary parts of the cellular refractive index. Whilst the two-layered spherical model has been employed here *a priori*, the effects of non-sphericity may be as important as those of cellular heterogeneity. There is thus a need to examine the impacts of using models employing a heterogeneous non-spherical geometry, expanding on the preliminary studies that have been conducted in this regard for small cells [Quirantes & Bernard 2004].

Whilst the major focus of this study has been the optical properties of the micro-algal milieu, there is a well documented need to better understand backscattering from other sources in the ocean [Stramski *et al.* 2004 and references within]. The results presented here emphasise this need, indicating that non-algal particulate matter represents a major source of backscattering, even in the highly productive waters of the southern Benguela. It is likely that a considerable part of this non-algal backscattering signal is associated with small particles (< 1 μm) [*ibid.*]. As the distinction between the particulate and dissolved components of seawater becomes blurred at these sizes, so a greater knowledge of what is operationally defined as the dissolved component (gelbstoff) becomes necessary.

Analytical models of ocean colour, in addition to the inherent optical properties of the marine constituents, require geometrical shape factors expressing the bidirectional character of the upwelling light field in the sea. These shape factors – the remote sensing reflectance utilised in this study employs the f/Q factor – are dependent upon illumination conditions, sea state, and the volume scattering function associated with seawater and its constituents. The f/Q factor is thus known to be sensitive to the angular scattering

characteristics of the marine hydrosol, and whilst the f/Q data employed in this study represent the most detailed data currently available [Morel *et al.* 2002], there is little doubt that they are sub-optimal for application to very high biomass waters (for which they were not designed). Detailed analyses of this shape factor require radiative transfer modelling, and there would be considerable benefit to conducting these analyses, using radiative transfer models coupled to the two-layered spherical population models, to assess f/Q variability for HAB scenarios. The ability to characterize f/Q with regard to the effects of high biomass (> 10 mg m^{-3} Chl *a*), and the spectrally variant volume scattering function and backscattering probability data given by the two-layered model, will undoubtedly increase the effectiveness of the inverse reflectance algorithm.

The reflectance algorithm also offers the ability to distinguish the solar stimulated algal fluorescence peak, centered at ~ 683 nm, from backscattered light at these wavelengths [e.g. Roesler & Perry 1995]. Whilst such an application has not been explored here, these fluorescence data offer a potential physiological insight to the algal assemblage, available either from autonomous *in situ* instrumentation or from space. Algorithm returned algal absorption in combination with a derived fluorescence peak offer a means to derive the fluorescence quantum yield [*ibid.*], thus providing the potential to remotely examine physiological stress and photosynthetic parameters [Young & Beardall 2003, Yoshikawa & Furuya 2004].

The reflectance algorithm is already undergoing trial operational use with moored autonomous hyperspectral sensors. An essential aspect of this use is establishing the effectiveness of the algal identifiers returned by the algorithm with regard to the identity of potentially harmful algal assemblages: linking a metric based on optical causality to conventional taxonomy. A probabilistic approach is perhaps likely to be most effective in this regard, whereby concurrent environmental data are used in conjunction with the bio-optically derived data to assess probable bloom identity. The use of the reflectance algorithm with space-based ocean colour data has the potential to provide a powerful remote sensing tool - adaption of the algorithm for currently active multispectral ocean colour sensors is underway.

Appendix 1

Potential errors associated with numerical derivations of algal and detrital size distribution

In both Chapters 2 and 3, numerical methods are employed to estimate size distributions of the detrital, i.e. non-algal particulate component – these distributions are subsequently used to calculate the algal size distributions central to these chapters. It is thus necessary to understand the potential errors arising from the methods used to obtain these size distribution data, and potential subsequent impacts. Such considerations are of particular importance to the discussions presented in Chapter 3, as it is from the derived algal size distribution data that the core causal absorption variables of effective diameter, c_i and unpackaged absorption are derived.

Particle sizing techniques employing Coulter methods have a thirty year history in the determination of the size distribution of marine particulate [e.g. Sheldon *et al.* 1972, Olivieri 1985]. However, such measurements have pertained only to the total marine particulate, and few Coulter determinations have been made solely of the size distributions of phytoplankton themselves in their natural state – somewhat unsurprisingly given the methodological complexities involved. Measurement of the algal size distribution for naturally occurring samples requires some means of measuring or deriving the size distribution of other marine particulate, specifically detritus if considering the size range of 1 μm to 100 μm in a system where there is unlikely to be significant terrigenous input. These detrital data are then used in a subtractive manner to calculate the size distribution of viable algal particles only, in a manner analogous to the algal/detrital absorption separation methods of Kishino [1985].

Numerical methods have been used here to determine the size distribution of detrital matter; specifically an optical model used to determine the detrital PSD using assumed size parameters and measured detrital absorption [Chapter 2]. However, the assumptions necessary to these methods, those of a fixed detrital imaginary refractive index and size

distribution shape, will impact calculations of both algal effective diameter and c_i values, and the unpackaged spectral absorption values employed as spectral basis vectors by the inverse models. The assumption of a Jungian shape can be supported by existing measurements of non-algal particulate in natural waters: using flow cytometry [Green *et al.* 2003] or Coulter measurements from bottom-[McCave 1983, Boss *et al.* 2001] or mid-water samples [McCave 1984] dominated by non-algal particulate. Published data also support the assumption of an exponential shape for detrital absorption and thus the imaginary part of the refractive index [Roesler *et al.* 1989, Iturriaga & Siegel 1989]. However, the value of the Junge slope assumed (ξ=4) and the refractive index spectra (n'=0.001066 exp(-0.007168)) can be considered only as representative values within a range, and in the absence of detailed data allowing potential error calculations, an error assessment can only be made by examining the effects of assuming more extreme values for these two parameters.

A study was carried out on the sensitivity of calculations of d_{eff}, c_i and $a^*_{\phi\alpha}$ values to variations in the parameters used to calculate the algal portion of the size distribution from the measured size distribution and particulate absorption data. These parameters are the Junge slope parameter ξ of the detrital size distribution, and the values used to calculate the slope of the imaginary refractive index of the detrital component $n'(\lambda) = n'(400) \exp(-S)$ (see Chapter 2.2). Junge slope values were allowed to vary from $3 < \xi < 5$, and refractive index values were allowed to vary from $0.005 < n'(400) < 0.02$ and $0.005 < S < 0.013$. The Junge slope values are representative of the range of values found in natural waters [Boss *et al.* 2001], whilst the refractive index slope values represent the range of detrital absorption slope values found here, similar to previously published values [Roesler *et al.* 1989] - assuming the imaginary refractive index of the detrital component is similar in spectral behaviour to detrital absorption. The sensitivity study shows the following:

- All algal parameters displayed relative insensitivity to changes in the detrital Junge slope ξ, with average deviations in d_{eff}, c_i and $a^*_{\phi\alpha}$ of under 10 % relative to the data

used in the study (ξ=4). Maximum deviations were found with ξ=3 in $a^*_{\phi u}$ for large cells and c_i for small cells. These deviations corresponded to ~ 25 % changes in the slope value ξ.

- All algal parameters displayed relative insensitivity to changes in the magnitude of the detrital imaginary refractive index $n'(400)$, with average deviations in d_{eff}, c_i and $a^*_{\phi u}$ of under 10 % relative to the data used in the study (ξ=4). Maximum deviations were found with $n'(400)$=0.0005 in $a^*_{\phi u}$ for large cells. These deviations corresponded to ~ 60 % changes in $n'(400)$.

- The greatest sensitivity in all parameters was shown to slope S of the detrital imaginary refractive index, with average deviations of 10% in d_{eff}, 28 % in c_i, and 27 % in $a^*_{\phi u}$. Maximum deviations were again found with S=0.013 in $a^*_{\phi u}$ for large cells and c_i for small cells. These deviations corresponded to ~ 80 % changes in the slope value S.

The sensitivity study indicates that in the context of the large observed variability in the whole data set for absorption and related bio-physical descriptors, the sensitivity to changes in the assumed detrital parameters used in processing the algal size distribution data are generally small. Nevertheless, the study shows that errors from the detrital assumptions are most likely to be manifest in the c_i values of assemblages dominated by very small cells, and the unpackaged absorption values of assemblages dominated by very large cells. These phenomena may be responsible for several apparent incongruities in the data: the relatively small c_i values of the *Aureococcus*-dominated assemblages, and the relatively low values of unpackaged absorption for the assemblage employed for the *dinoflagellate* basis vector.

Appendix II

Location of Sampling Sites

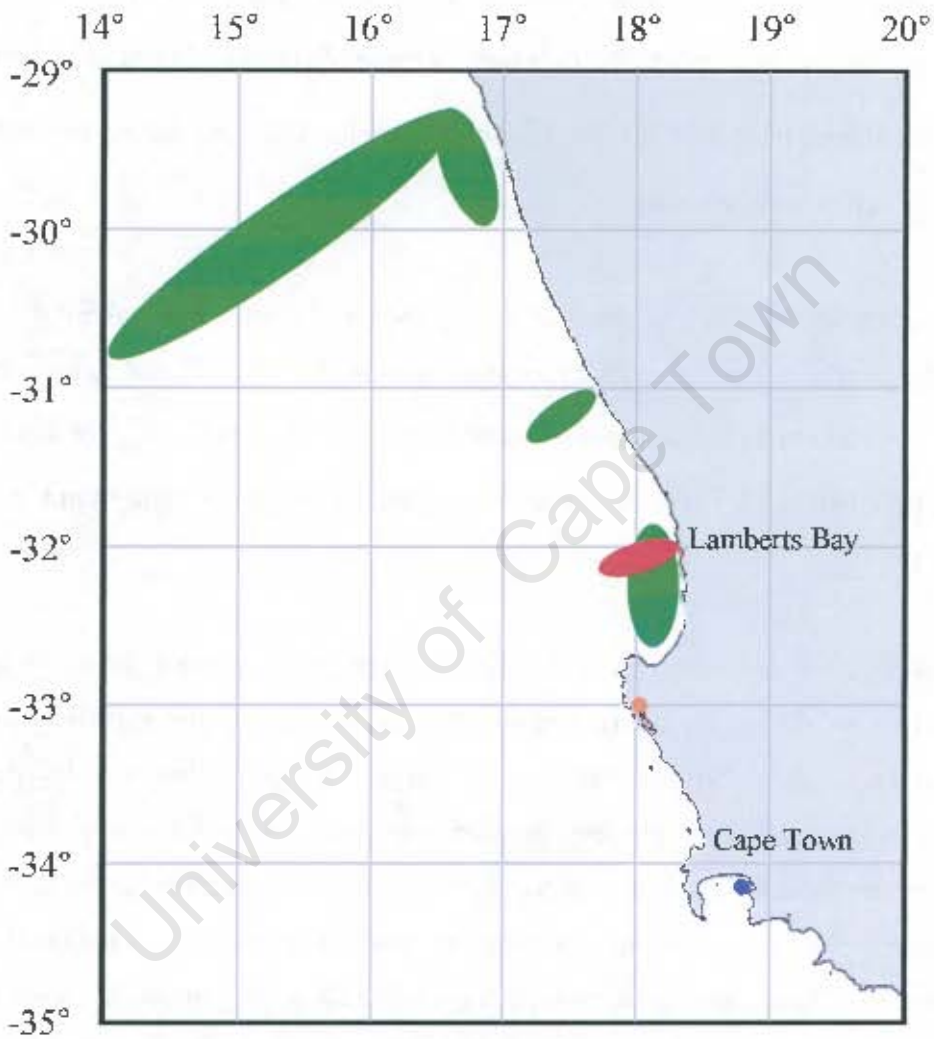

- 1999/2002 BENEFIT & BENCAL cruises
- 1999/2003 Saldanha Bay *A. anophagefferens* sampling
- 2001 False Bay *K. cristata* sampling
- 1999 – 2004 Lamberts Bay sampling

Appendix III
Notation

Symbol	Definition	Unit
a	absorption coefficient	m^{-1}
a_{cm}	absorption of cellular material	m^{-1}
a_d	detrital absorption coefficient	m^{-1}
a_g	gelsbtoff absorption coefficient	m^{-1}
a_{gd}	combined gelsbtoff and detrital absorption coefficient	m^{-1}
a_ϕ	phytoplankton absorption coefficient	m^{-1}
a_p	particulate absorption coefficient	m^{-1}
a_ϕ^*	Chl *a* specific phytoplankton absorption	m^2 mg Chl a^{-1}
$a_{\phi u}^*$	unpackaged Chl *a* specific phytoplankton absorption	m^2 mg Chl a^{-1}
ASF	Area scaling factor for size distribution manipulation	dimensionless
b	scattering coefficient	m^{-1}
b_p	particulate scattering coefficient	m^{-1}
b_ϕ	phytoplankton scattering coefficient	m^{-1}
b_ϕ^*	Chl *a* specific phytoplankton scattering coefficient	m^2 mg Chl a^{-1}
b_b	backscattering coefficient	m^{-1}
b_{bp}	Particulate backscattering coefficient	m^{-1}
b_{bs}	Small particle backscattering coefficient	m^{-1}
$b_{b\phi}$	phytoplankton backscattering coefficient	m^{-1}
$b_{b\phi}^*$	Chl *a* specific phytoplankton backscattering coefficient	m^2 mg Chl a^{-1}
$\tilde{b}_b$	backscattering probability	dimensionless
$\tilde{b}_{b\phi}$	phytoplankton backscattering probability	dimensionless
c	attenuation coefficient	m^{-1}
c_ϕ	phytoplankton absorption coefficient	m^{-1}
c_ϕ^*	Chl *a* specific phytoplankton absorption	m^2 mg Chl a^{-1}
c_i	intracellular Chl *a* concentration	kg m^{-3}
Chl *a*	total algal chlorophyll *a* concentration	mg m^{-3}
d	particle diameter	µm
d_{eff}	effective diameter of size distribution	µm
$< d^k >$	kth diametric moment	varies
E_d	downwelling irradiance	µW $cm^{-2}nm^{-1}$

Symbol	Definition	Unit
$F(d)$	number of particles per unit volume per micrometer	# $m^{-3}\mu m^{-1}$
$F^*(d)$	Chl *a* specific no. of particles per unit volume per micrometer	# $m^{-3}\mu m^{-1}mg^{-1}$
K_u	diffuse attenuation coefficient	m^{-1}
I_{-u}	upwelling radiance	$\mu W\ cm^{-2}nm^{-1}sr^{-1}$
m	complex refractive index	dimensionless
m_h	complex refractive index of a homogeneous particle	dimensionless
m_{chlor}	complex refractive indexof the chloroplast	dimensionless
m_{cyto}	complex refractive index of the cytoplasm	dimensionless
n	real part of the refractive index	dimensionless
n_h	real part of the refractive index of a homogeneous particle	dimensionless
n_{chlor}	real part of the refractive indexof the chloroplast	dimensionless
n_{cyto}	real part of the refractive index of the cytoplasm	dimensionless
n'	imaginary part of the refractive index	dimensionless
n'_h	imaginary part of the refractive index of a homogeneous particle	dimensionless
n'_{chlor}	imaginary part of the refractive indexof the chloroplast	dimensionless
n'_{cyto}	imaginary part of the refractive index of the cytoplasm	dimensionless
N/V	number of particles per unit volume	# m^{-3}
P_n	normalised scaling parameter for algal group	dimensionless
Q_{ab}	absorption efficiency factor	dimensionless
$\bar{Q}_{ab}$	mean absorption efficiency factor of a size distribution	dimensionless
Q_a^*	package effect parameter	dimensionless
Q_b	scattering efficiency factor	dimensionless
Q_{bb}	backscattering efficiency factor	dimensionless
$\bar{Q}_{bb}$	mean backscattering efficiency factor of a size distribution	dimensionless
Q_c	attenuation efficiency factor	dimensionless
r	particle radius	μm
r_{eff}	effective radius of a particle size distribution	μm
R_{rs}	remote sensing reflectance	sr^{-1}
S	gelbstoff absorption slope factor exponent	dimensionless
$<SA>$	projected surface area of a size distribution	m^2
V	particle volume	m^3
$\bar{V}$	total relative particle volume	dimensionless
α	Mie size parameter	dimensionless
β	volume scattering function	$m^{-1}sr^{-1}$
$\bar{\beta}$	scattering phase function	sr^{-1}

Symbol	Definition	Unit
Δn	spectral variability in the real part of the reafractive index	dimensionless
$1+\varepsilon$	central value of the real part of the refractive index	Dimensionless
ρ'	optical thickness	dimensionless
λ	in vacuo wavelength	nm
θ	scattering angle	degrees
τ	Fresnel reflectance	dimensionless
υ_{eff}	Effective variance of a particle size distribution	dimensionless
ξ	Junge slope exponent	dimensionless

Bibliography

Aas, E., 1984. Influence of shape and structure on light scattering by marine particles. Rep. Dept. Geophys., Univ. Oslo, 53, 112 pp.

Aas, E., 1996. Refractive index of phytoplankton derived from its metabolite composition. *J. Plankton Res.*, 18: 2223-2249.

Aden A.L., and M. Kerker. 1951. Scattering of electromagnetic waves from two concentric spheres. *J. Appl. Phys.* 22: 1242-1246

Agusti, S., C.M. Duarte, and J. Kalff. 1987. Algal Cell Size and the Maximum Density and Biomass of Phytoplankton. *Limnol. Oceanogr.* 32(4): 983-986.

Agusti, S. 1991. Allometric scaling of light absorption and scattering by phytoplankton cells. *Can. J. Fish. Aquat. Sci.* 48: 763–767.

Ahn, Y-H., A. Bricaud, and A. Morel. 1992. Light backscattering efficiency and related properties of some phytoplankters. *Deep-Sea Res.* 39A: 1835-1855.

Albert, A. and Mobley, C. D. 2003. An analytical model for subsurface irradiance and remote sensing reflectance in deep and shallow case-2 waters. *Opt. Express*, 11: 2873-2890.

Alexandrov, M.D., and A.A. Lacis. 2000. A new three-parameter cloud/aerosol particle size distribution based on the generalized inverse Gaussian density function. *Appl. Math. Comput.* 116: 153-165

Andersson, P. O., T. Gillbro, L. Ferguson, and R. J. Cogdell. 1991. Absorption spectral shift of carotenoids related to medium polarizability. *Photochem. Photobiol.* 54: 353–360.

Babin, M., Morel, A. and Gentili, B. 1996. Remote sensing of surface Sun-induced chlorophyll fluorescence: consequences of natural variations in the optical characteristics of phytoplankton and the quantum yield of chlorophyll a fluorescence. *Int. J. Rem. Sens.*, 17: 2417-2448.

Babin, M., and D. Stramski. 2002. Light absorption by aquatic particles in the near-infrared spectral region. *Limnol. Oceanogr.*, 47: 911-915.

Bader, H. 1970. The hyperbolic distribution of particle sizes. *J. Geophys. Res.* 75: 2822-2830.

Banse, K. 1976. Rates of growth, respiration and photosynthesis of unicell algae as related to cell size: a review. *J. Phycol.* 12: 135-40.

Barlow, R.G., D. G. Cummings, and S. W. Gibb. 1997. Improved resolution of mono- and divinyl chlorophylls a and b and zeaxanthin and lutein in phytoplankton extracts using reverse phase C-8 HPLC. *Mar. Ecol. Prog. Ser.* 161: 303-307.

Barlow, R., H. Sessions, N. Silulwane, H. Engel, S.B. Hooker, J. Aiken, J. Fishwick, V. Vicente, A. Morel, M. Chami, J. Ras, S. Bernard, M. Pfaff, J.W. Brown, and A. Fawcett, 2003: BENCAL Cruise Report, *NASA/TM 2003-206892, Vol. 27*, S.B. Hooker and E.R. Firestone, Eds., NASA Goddard Space Flight Center, Greenbelt, Maryland, September 2003, 64 pp.

Bernard, S. 1996. The chemical and bio-optical characterisation of gelbstoff in the southern African waters: a preliminary analysis. M.Sc. thesis: University of Cape Town, 114pp.

Bernard, S., T.A. Probyn, and Barlow R.G. 2001. Measured and modelled optical properties of particulate matter in the southern Benguela. *S. Afr. J. Sci.* 97(9-10): 410-420.

Berner, T., Z. Dubinsky, K. Wyman, and P.G. Falkowski. 1989. Photoadaptation and the package effect in *Dunaliella tertiolecta* (Chlorophyceae). *J. Phycol.* 25: 70-7.

Bidigare, R.R. 1989. Photosynthetic pigment composition of the brown tide alga: unique chlorophyll and carotenoid derivatives. *In, Novel phytoplankton blooms: causes and impacts of recurrent brown tides and other unusual blooms,* [ed.E.M.Cosper, V.M. Bricelj and E.J.Carpenter] . Berlin: Springer-Verlag. 799pp.

Bidigare, R. R., M.E. Ondrusek, J.H. Morrow, D.A. Kiefer. 1990. *In vivo* absorption properties of algal pigments. In: Spinrad, R. W. (ed.) Ocean Optics X, Proc. Soc. Photo-Opt. Instrum. Eng. 1302: 90-302.

Bohren C.F. and D.R. Huffman D.R. 1983. Absorption and scattering of light by small particles, pp. 530. John Wiley and Sons, New York.

Boss, E., W.S. Pegau, W.D. Gardner, J.R.V. Zaneveld, A.H. Barnard, M.S. Twardowski, G.C. Chang, and T.D. Dickey. 2001. Spectral particulate attenuation in the bottom boundary layer of a continental shelf. *J. Geophys. Res.* 106(C5): 9509-9516.

Boss, E., M.S. Twardowski, and S. Herring. 2001a. Shape of the particulate beam attenuation spectrum and its inversion to obtain the shape of the particulate size distribution. *Appl. Opt.* 40: 4885-4893.

Bricaud, A., A. Morel, and L. Prieur. 1981. Absorption by dissolved organic matter of the sea (yellow substance) in the UV and visible domains, *Limnol. Oceanogr.*, 26: 43-53.

Bricaud, A., A. Morel, and L. Prieur. 1983. Optical efficiency factors of some phytoplankters, *Limnol. Oceanogr.* 28: 816-832.

Bricaud A. and A. Morel. 1986. Light attenuation and scattering by phytoplanktonic cells: a theoretical modeling. *Appl. Opt.* 25: 571-580.

Bricaud A., A.L. Bedhomme, and A. Morel. 1988. Optical properties of diverse phytoplanktonic species: experimental results and theoretical interpretation. *J. Plankton Res.* 10: 851-873.

Bricaud, A., and D. Stramski. 1990. Spectral absorption coefficients of living phytoplankton and nonalgal biogenous matter: A comparison between the Peru upwelling area and the Sargasso Sea, *Limnol. Oceanogr.* 35: 562-582.

Bricaud A, J.R.V. Zaneveld, and J.C. Kitchen. 1992. Backscattering efficiency of coccolithophorids: use of a three-layered sphere model. In: Gilbert GD, editor. Ocean Optics XI. Proc SPIE, 1750: 27–33.

Bricaud A., M. Babin, A. Morel, and H. Claustre. 1995. Variability in the chlorophyll-specific absorption coefficients of natural phytoplankton: Analysis and parameterization. *J. Geophys. Res.* 100: 13 321-13 332.

Bricaud, A., Claustre, H., Ras, J. and K. Oubelkheir. 2004. Natural varaibility of phytoplankton absorption in oceanic waters : influence of the size structure of algal populations. *J. Geophys. Res.*, 109, C11010.

Bryant FD, Seiber, and BA, Latimer, 1969. Absolute optical cross sections of cells and chloroplasts, *Arch Biochem Biophys.*, 1969,135(1): 97-108.

Buiteveld H., J. M. H. Hakvoort, M. Donze, 1994. The optical properties of pure water," *SPIE Proceedings on Ocean Optics XII*, edited by J. S. Jaffe, 2258: 174–183.

Butler, W. L. and D.W. Hopkins, 1970. An analysis of fourth derivative spectra. *Photochem. Photobiol.*, 12, 451 456.

Caffarri S., R. Croce, J. Breton, and R. Bassi, 2001. The Major Antenna Complex of Photosystem II Has a Xanthophyll Binding Site Not Involved in Light Harvesting. *Journ. Biol.Chem.*, 276 (38): 35924–35933.

Campbell, J. W. 1995. The lognormal distribution as a model for bio-optical variability in the sea. *J. Geophys. Res.* 100(C7): 13237-13254.

Carder, K.L. and Steward, R.G. 1985. A remote-sensing reflectance model of a red-tide dinoflagellate off west Florida. *Limnol. Oceanogr.*, 30: 286-298.

Carder, K.L., R.G. Steward, J.H. Paul, and G.A. Vargo. 1991. Reflectance model for quantifying chlorophyll a in the presence of productivity degradation products. *J. Geophys. Res.*, 96: 20599-20611.

Chang, G. C., K. Mahoney, A. Briggs-Whitmire, D. Kohler, C. Mobley, M. Moline, M. Lewis, E. Boss, M. Kim, W. Philpot, and T. Dickey. 2004. The New Age of Hyperspectral Oceanography, *Oceanography*, 17(2): 22-29.

Charney, E. and F. S. Brackett, 1961. The spectral dependence of scattering from a spherical alga and its implications for the state of organization of the light-accepting pigments. *Arch. Biochem. Biophys.*, 92: 1-12.

Chylek P.and G. Videen, 1998. Scattering by a composite sphere and effective medium approximations. *Opt. Comm.*, 146: 15-20.

Cinque G., R. Croce, A.R. Holzwarth, and R. Bassi. 2000. Förster energy transfer in the chlorophyll a/b complex CP29. *Biophys.J*, 79: 1706-1717.

Ciotti, A.M., M. R. Lewis, and J.J. Cullen. 2002. Assessment of the relationships between dominant cell size in natural phytoplankton communities and the spectral shape of the absorption coefficient. *Limnol. Oceanogr.* 47(2): 404–417.

Cleveland J. and others. 2004. Special Issue: Coastal Ocean Optics and Dynamics, *Oceanography*, 17(2).

Collins, D.J., D.A. Kiefer, J.B. Soohoo, and I.S. McDermid. 1985. The role of reabsorption in the spectral distribution of phytoplankton fluorescence emission. *Deep-Sea Res.* 32(8A): 983-1003.

Conover, W. J. 1980. *Practical Nonparametric Statistics.* pp357. New York, Wiley.

Cullen, J. J., A. M. Ciotti, R. F. Davis, and M. R. Lewis. 1997. Optical detection and assessment of algal blooms. *Limnol. Oceanogr.* 42(5): 1223-1239.

Dodge J.D. and R.M. Crawford. 1969. Observations on the fine structure of the eyespot and associated organelles in the dinoflagellate *Glenodinium foliaceum* . *J Cell Sci*, 5: 479-493.

Duysens, L. N. M. 1956. The flattening of the absorption spectrum of suspensions as compared to that of solutions. *Biochim. Biophys. Acta*, 19: 1–12.

Eisner, L., M.S. Twardowski, T.J. Cowles, and M.J. Perry. 2003. Resolving phytoplankton photoprotective:photosynthetic carotenoid ratios on fine scales using in situ spectral absorption measurements. *Limnol. Oceanogr.* 48: 632–646.

Finkel, Z.V., and A.J. Irwin. 2000. Modelling size-dependent photosynthesis: light absorption and the allometric rule. *J. Theor. Biol.*, 204: 361-369.

Finkel, Z.V. 2001. Light absorption and size scaling of light-limited metabolism in marine diatoms. *Limnol. Oceanogr.*, 46: 86-94.

Fisher, R.A. 1921. On the 'probable error' of a coefficient of correlation deduced from a small sample. *Metron*, 1: 1–32.

Fisher T., T. Berner, D. Iluz, and Z. Dubinsky. 1998. The kinetics of the photoacclimation response of *Nannochloropsis* sp. (Eustigmatophyceae): a study of changes in ultrastructure and psu density. *J. Phycol.*, 34 (5): 818-824.

Garver, S.A., and D.A. Siegel. 1997. Inherent optical property inversion of ocean color spectra and its biogeochemical interpretation. 1: Time series from the Sargasso Sea. *J. Geophys. Res.*, 102: 18 607-18 625.

Gastrich, M.D., O.R. Anderson, S.S. Benmayor, E.M. Cosper. 1998. Ultrastructural analysis of viral invection in the brown-tide alga, *Aureococcus anophagefferens* (Pelagophyceae). *Phycologia*, 37: 300-306.

Geider, R.J., and B.A. Osborne. 1987. Light absorption by a marine diatom: Experimental observations and theoretical calculations of the package effect in a small *Thalassiosira* species. *Mar. Biol.*, 96(2): 299-308.

Gordon, H.R. and W.R. McLuney (1975). Estimation of the depth of sunlight penetration in the sea for remote sensing. *Appl. Opt.*, 14: 413-416.

Gordon H.R., O.B. Brown, R.H. Evans, J.W. Brown, R.C. Smith, K.S. Baker, and D.K. Clark, 1988. A semianalytic radiance model of ocean color, *J. Geophys. Res.*, 93: 10909-10924.

Gower, J.F.R., R. Doerffer, and G.A. Borstad, 1999, Interpretation of the 685 nm peak in water-leaving radiance spectra in terms of fluorescence, absorption and scattering, and its observation by MERIS, *Int. J. Remote Sensing*, 9: 1771-1786.

Green J.C. 1980. The fine structure of *Pavlova pinguis* Green and a preliminary survey of the order Pavlovales (Prymnesiophyceae). *Br. Phycol. J.*, 15(2): 151-191.
Green, R.E., H.M. Sosik, R.J. Olson, and M.D. DuRand. 2003. Flow cytometric determination of size and complex refractive index for marine particles: comparison with independent and bulk estimates *Appl. Opt.* 42(3): 526-541.

Grenfell, T. C. and S. G. Warren, 1999, Representation of a nonspherical ice particle by a collection of independent spheres for scattering and absorption of radiation, *J. Geophys. Res.*, 104(D24): 31,697-31,709.

Gruszecki, W.I., Grudzinski, W., Banaszek-Glos, A., Matula, M., Kernen, P., Krupa, Z., and Sielewiesiuk, J. 1999. Xanthophyll pigments in light-harvesting complex II in monomolecular layers: localisation, energy transfer and orientation. *Biochim. Biophys. Acta.* 1412: 173–183.

Gustafson D.E., D.K. Stoecker, M.D. Johnson, W.F. Van Heukelem, and K. Sneider. 2000. Cryptophyte algae are robbed of their organelles by the marine ciliate *Mesodinium rubrum*. Nature. 405(6790): 1049-1052.

Hackett J.D., L. Maranda, H.S. Yoon, and D. Bhattacharya. 2003. Phylogenetic evidence for the cryptophyte origin of the Plastid of *Dinophysis* (dinophysiales, dinophyceae). *J. Phycol.* 39: 440–448.

Hansen, J.E., and L.D. Travis. 1974. Light scattering in planetary atmospheres. *Space. Sci. Rev.*,16: 527-610.

Hewes, C. D., B. G. Mitchell, T. A. Moisan, M. Vernet, and F. M. H. Reid, 1998. The phycobilin signatures of chloroplasts from three dinoflagellate species: a microanalytical study of *Dinophysis caudata, D. fortii* and *D. acuminata* (Dinophysiales, Dinophyceae).
J. Phycol., 34: 945–51.

Highfill, J.F. and Pfiester, L.A. 1992. The sexual and asexual life cycle of *Glenodiniopsis steinii* (Dinophyceae). *Am. J. Bot.*, 1992: 899-903.

Hitchcock G.L. 1982. A comparative study of the size-dependent organic composition of marine diatoms and dinoflagellates *J. Plankton Res.*, 4: 363–377.

Hoepffner, N. and S. Sathyendranath, 1993, Determination of the major groups of phytoplankton pigments from the absorption spectra of total particulate matter. *J. Geophys Res.*, 98: 22789–22803.

Hoops, H.J. and G.L. Floyd. 1979. Ultrastructure of the centric diatom, *Cyclotella meneghiniana*: Vegetative cell and auxospore development. *Phycologia* 18: 424-435.

Hu, Y. X., and K. Stamnes. 1993. An accurate parameterization of cloud radiative properties suitable for climate modeling. *J. Climate.*, 6: 728-742.

Hutchings, L., G.C. Pitcher, T.A. Probyn, G.W. Bailey.1994. The Chemical and Biological Consequences of Coastal Upwelling. (ed. C.P. Summerhayes, K.C. Emeis, M.V. Angel, R.L. Smith, and B. Zeitzschel), *Dahlem Workshop on Upwelling in the Ocean: Modern Processes and Ancient Records*, Berlin (Germany), John Wiley and Sons, pp. 65-82.

Iturriaga, R. and D.A. Siegel. 1989. Microphotometric characterization of phytoplankton and detrital absorption properties in the Sargasso Sea. *Limnol. Oceanogr.*, 34: 1706 1726.

Janssen, M., L. Bathke, J. Marquardt, W.E. Krumbein, and E. Rhiel, 2001. Changes in the photosynthetic apparatus of diatoms in response to low and high light intensities. *Int. Microbiol.* 4: 27-33.

Jeffrey, S. W. and M. Vesk. 1977. Effect of blue-green light on photosynthetic pigments and chloroplast structure in the marine diatom *Stephanopyxis turbis*. *J. Phycology*, 13: 271-279.

Jeffrey S.W., R.F.C. Mantoura, and S.W. Wright. 1997. *Phytoplankton pigments in oceanography: guidelines to modern methods*, 661pp. Monographs on Oceanographic Methodology 10, UNESCO, Paris.

Jenks, A. and S.P. Gibbs. 2000. Immunolocalization and distribution of Form II Rubisco in the pyrenoid and chloroplast stroma of *Amphidinium carterae* and Form I Rubisco in the symbiont-derived plastids of *Peridinium foliaceum* (Dinophyceae). *J. Phycology*, 36: 127-138.

Jennings R.C. and G. Zucchelli. 1985. The influence of membrane stacking on light absorption by chloroplasts. *Photobiochem. Photobiophys.*, 9: 215-221.

Johnsen, G., N.B. Nelson, R.V.M. Jovine and B.B. Prezelin. 1994. Chromoprotein- and pigment-dependent modelling of spectral light absorption in two dinoflagellates, *Prorocentrum minimum* and *Heterocapsa pygmaea*. *Mar. Ecol. Prog. Ser.*, 114: 245-258.

Johnsen, G., O. Samset, L. Granskog, and E. Sakshaug. 1994a. *In-vivo* absorption characteristics in 10 classes of bloom-forming phytoplankton: taxonomic characteristics and responses to photoadaptation by means of discriminant and HPLC analysis. *Mar. Ecol. Prog. Ser.*, 105(1/2): 149-157.

Johnsen, G., B.B. Prezelin, and R.V.M. Jovine. 1997. Fluorescence excitation spectra and light utilization in two red tide dinoflagellates. *Limnol. Oceanogr.*, 42(5): 1166-1177.

Jonasz, M. and G. Fournier. 1996. Approximation of the size distribution of marine particles by a sum of log-normal functions. *Limnol. Oceanog.* 41: 744-754.

Junge, E.C. 1963. *Air chemistry and radioactivity*, pp.382, Academic Press, London.

Kirk, J.T.O. 1975. A theoretical analysis of the contribution of algal cells to the attenuation of light within natural waters. II. Spherical cells. *New. Phytol.*, 75: 21-36.

Kirk, J. T. O. 1980. Spectral absorption properties of natural waters: contribution of the soluble and particulate fractions to light absorption in some inland waters of south-eastern Australia. *Aust. J. Mar. Freshwater Res.*, 31: 287–296.

Kirkpatrick, G. J., D.F. Millie, M.A. Moline, and O.M. Schofield. 2000. Optical discrimination of a phytoplankton species in natural mixed populations. *Limnol. Oceanogr.*, 45: 467–471.

Kishino, M., M. Takahashi, N. Okami, and S. Ichimura. 1985. Estimation of the spectral absorption coefficients of phytoplankton in the sea. *Bull. Mar. Sci.*, 37: 634-642.

Kitchen, J.C., J.R.V. Zaneveld, and H. Pak. 1982. Effect of particle size distribution and chlorophyll content on beam attenuation spectra. *Appl. Opt.*, 21: 3913-3918.

Kitchen JC, and J.R.V. Zaneveld 1992. A three-layered sphere model of the optical properties of phytoplankton. *Limnol. Oceanogr.*, 37: 1680–90.

Kleima, F. J., E. Hofmann, B. Gobets, I. H.M. van Stokkum, R. van Grondelle, K. Diederichs, and H. van Amerongen. 2000. Forster excitation energy transfer in peridinin-chlorophyll-a-protein. *Biophys. J.* 78: 344-353.

Kyewalyanga M., S. Sathyendranath and T.Platt. 2002. Effect of *Mesodinium rubrum* (= *Myrionecta rubra*) on the action and absorption spectra of phytoplankton in a coastal marine inlet. *J. Plank.Res.*, 24 (7): 687-702.

Lacis, A., Hansen, J. E., and Sato, M. 1992. Climate forcing by strato-spheric acrosols, *Geophys. Res. Lett.*, 19: 1607–1610.

Latimer P. 1984. Light scattering by a homogeneous sphere with radial projections. *Appl. Opt.* 23(3): 442-447.

Lohrenz, S.E., A.D. Weidemann , and M. Tuel. 2003. Phytoplankton spectral absorption as influenced by community size structure and pigment composition. *J. Plankton. Res.* 25(1): 33-61.

Mallone R.A., and Dana D.R. 1997. Instruments and methods for measuring the backward-scattering coef.cient of ocean waters. *Appl. Opt.*, 36: 6057–67.

Malone,T.C. 1980. Algal size. In: Morris,I. (ed.), *The Physiological Ecology of Phytoplankton*. Blackwell, Oxford, pp. 433–463.

Maritorena, S., A. Morel, and B. Gentili. 2000. Determination of the fluorescence quantum yield by oceanic phytoplankton in their natural habitat *Appl. Opt.*, 39: 6725-6737.

McCave, I.N. 1983. Particulate size spectra, behavior, and origin of nepheloid layers over the Nova Scotian continental rise. *J. Geophys. Res.* C88: 7647-7666.

McCave, I. N. 1984. Size spectra and aggregation of suspended particles in the deep ocean. *Deep-Sea Res.* 31(4): 329-52.

McGraw, R., S. Nemesure, and S. E. Schwartz. 1998. Properties and evolution of aerosols with size distributions having identical moments. *J. Aerosol. Sci.* 29: 761-772.

Menden-Deuer, S. and E.J. Lessard. 2000. Carbon to volume relationships for dinoflagellates, diatoms, and other protist plankton. *Limnol. Oceanogr.*, 45: 569–579.

Messer, G. and Y. Ben-Shaul. 1972. Changes in chloroplast structure during culture growth of *Peridinium cinctum* fa. *westii* (Dinophyceae). *Phycologia*, 11: 291-299.

Meyer, R. A. 1979. Light scattering from biological cells: dependence of backscatter radiation on membrane thickness and refractive index. *Appl. Opt.* 18: 585–588.
Mie G. 1908. Beitra¨ ge zur Optik tru¨ ber Medien speziell kolloidaler Metallo¨ sungen. *Ann. Phys.* 4: 377–445.

Millie, D. F., G. B. Kirkpatrick, and B. T. Vinyard. 1995. Relating photosynthetic pigments and *in vivo* optical density spectra to irradiance for the Florida red-tide dinoflagellate, *Gymnodinium breve*. *Mar. Ecol. Prog. Ser.*, 120: 65-75.

Mishchenko, M.I., L.D. Travis, R.A. Kahn, and R.A. West. 1997. Modeling phase functions for dustlike tropospheric aerosols using a shape mixture of randomly oriented polydisperse spheroids. *J. Geophys. Res.*, 102: 16 831-16 847.

Mishchenko, M.I., and A.A. Lacis. 2003. Morphology-dependent resonances of nearly spherical particles in random orientation. *Appl. Opt.* 42: 5551-5556.

Moal, J., Martin-Jezequel, V., Harris, R. P., Samain, J. F. and Poulet, S. A. 1987. Interspecific and intraspecific variability of chemical composition of marine phytoplankton. *Oceanol. Acta*, 10: 339–346.

Montagnes, D.J.S., J.A. Berges, P.J. Harrison, and F.J.R. Taylor. 1994. Estimating carbon, nitrogen, protein, and chlorophyll a from cell volume in marine phytoplankton. *Limnol. Oceanogr.* 39: 1044-1060.

Morel, A. 1973. Diffusion de la lumiere par les eaux de mer: Resultats experimentaux et approche theorique, in *Optics of the Sea*, AGARD Lecture Ser., vol. 61, pp. 3.1.1–3.1.76, North Atlantic Treaty Org., Brussels.

Morel, A. 1974. Optical properties of pure water and pure seawater. p. 1-24, In: Jerlov & E. Steeman Nielsen (eds.). *Optical aspects of oceanography*. Academic Press.

Morel, A. and L. Pricur. 1977. Analysis of variations in ocean color. *Limnol. Oceanogr.*, 22: 709-722.

Morel A. and A. Bricaud. 1981. Theoretical results concerning light absorption in a discrete medium, and application to specific absorption of phytoplankton. *Deep-Sea Res.* 28: 1375-1393.

Morel A. and A. Bricaud. 1986. Inherent properties of algal cells including picoplankton: theoretical and experimental results. *Can. Bull. Fish. Aquat. Sci.*, 214: 521-559.

Morel, A. 1988. Optical modeling of the upper ocean in relation to its biogenous matter content (case 1 water), *J. Geophys. Res.*, 93: 10,749-10,768.

Morel, A., and Y.H. Ahn. 1990. Optical efficiency factors of free-living marine bacteria: Influence of bacterioplankton upon the optical properties and particulate organic carbon in oceanic waters. *J. Mar. Res.*, 48: 145-175.

Morel, A., and Y.H. Ahn. 1991. Optics of heterotrophic nanoflagellates and ciliates: A tentative assessment of their scattering role in oceanic waters compared to those of bacterial and algal cells. *J. Mar. Res.* 49: 177-202.

Morel, A., D. Antoine, and B. Gentili. 2002. Bidirectional reflectance of oceanic waters: Accounting for Raman emission and varying particle phase function, *Appl. Opt.*, 41: 6289-6306.
Morel, A. and B. Gentili. 2004. Radiation transport within oceanic (case 1) waters. *J. Geophys. Res.*, 109(C6): C06008.

Muller-Parker, G., K.W. Lee and C.B. Cook. 1996. Changes in the ultrastructure of symbiotic zooxanthellae (*Symbiodinium* sp., Dinophyceae) in fed and starved sea anemones (*Aiptasia pallida*) maintained under high and low light. *J. Phycol.*, 32: 987-994.

Naqvi K.R., M. N. Merzlyak and T. B. Melø. 2004. Absorption and scattering of light by suspensions of cells and subcellular particles: an analysis in terms of Kramers–Kronig relations. *Photochem. Photobiol. Sci.*, 3 (1): 132 – 137.

Nelder, J.A., and R. Mead. 1965. A Simplex Method for Function Minimization," *Computer J.*, 7: 308-313.

Ohi, N., Y. Ishiwata, and S. Taguchi. 2002. Diel patterns in light absorption and absorption efficiency factors of *Isochrysis galbana* (Prymnesiophyceae). *J. Phycl.* 38 (4): 730-737.

Oishi, T. 1990. Significant relationship between the backward scattering coefficient of seawater and the scatterance at 120 degrees. *Appl. Opt.*, 29: 4658–4665.

Olivieri, E.T. 1985. Feasibility of estimating phytoplankton size and biomass in fresh and preserved samples from the Benguela Current with a Coulter counter. *S. Afr. J. Sci.*, 3: 99-110.

Osborne, B. A. and J. A. Raven, 1986. Growth light level and photon absorption by cells of *Chlamydomonas rheinhardii, Dunaliella tertiolecta* (Chlorophyceae, Volvocales), *Scenedesmus obliquus* (Chlorophyceae, Chlorococcales) and *Euglena viridis* (Euglenophyceae, Euglenales). *Br. phycol. J.*, 21: 303-313.

Osborne, B. A. and R. J. Geider, 1989. Problems in the assessment of the package effect in five small phytoplankters. *Mar. Biol.*, 100: 151-159.

Paillotin G., W. Leibl, J. Gapinski, J. Breton, and A. Dobek. 1998. Light Gradients in Spherical Photosynthetic Vesicles. *Biophys J.*, 75: 124-133.

Pegau, W.S., J.S. Cleveland, W. Doss, C.D. Kennedy, R.A. Maffione, J.L. Mueller, R. Stone, C.C. Trees, A.D. Weidemann, W.H. Wells, and J.R.V. Zaneveld. 1995. A comparison of methods of the measurement of the absorption coefficient in natural waters, *J. Geophys. Res.*, 100: 13,201-13,220.

Pitcher, G.C., A.J. Boyd, D.A. Horstman, and B.A. Mitchell-Innes. 1998. Subsurface dinoflagellate populations, frontal blooms and the formation of red tide in the southern Benguela upwelling system. *Mar. Ecol. Prog. Ser.*, 172: 253-264.

Pitcher G. C., S. Bernard, and R. N. Pienaar. Brown tides on the west coast. *IOC Harmful Algae News*, January 1999.
Pitcher, G. C., and D. Calder. 2000. Harmful algal blooms of the southern Benguela current: A review and appraisal of monitoring from 1989 to 1997. *S. Afr. J. mar. Sci.* 22: 255-271.

Pope R. M., and E. S. Fry. 1997. Absorption spectrum (380-700 nm) of pure water. II. Integrating cavity measurements. *Appl. Opt.*, 36: 8710-8723.
Preisendorfer RW. 1976. *Hydrologic optics, vol. 5. Properties*. US Environmental Research Laboratories, USA.

Prezelin, B. B. and B.A. Boczar, B. A. 1986. Molecular bases of cell absorption and fluorescence in phytoplankton: potential applications to studies in optical oceanography. *Prog. Phycol., Res.*, 4: 350–464.

Quinby-Hunt, M.S., A.J. Hunt, K. Lofftus, and D. Shapiro. 1989. Polarized-light scattering studies of marine *Chlorella*. *Limnol. Oceanogr.*, 34 : 1587-1600.

Quirantes A., and S. Bernard. 2004. Light scattering by marine algae: two-layer spherical and nonspherical models. *J. Quant. Spectr. Rad. Transfer*, 89: 311-321.

Raven JA. 1984. A cost-benefit analysis of photon absorption by photosynthetic unicells. *New Phytol.*, 98: 593–625.

Raven, J. A. 1986. Physiological consequences of extremely small size for autotrophic organisms in the sea. In Platt, T & Li, W. K. W. [Eds.] Photosynthetic Picoplankton. vol. 214. *Can. Bull. Fish. Aquat. Sci.*, Ottawa, 583 pp.

Raven, J. A., and J.E. Kübler. 2002. New light on the scaling of metabolic rate with the size of algae. *J. Phycol.* 38: 1-11.

Reda, I. and Andreas, A. 2003. *Solar position algorithm for solar radiation application*. National Renewable Energy Laboratory (NREL), Technical report NREL/TP-560-34302.

Renge, I., R. van Grondelle and J. P. Dekker. 1996. Matrix and temperature effects on absorption spectra of β-carotene and pheophytin a in solution and in green plant photosystem II. *J. Photochem. Photobiol. A: Chem.*, 96: 109 121.

Risović, D. 1993. Two component model of sea particle size distribution. *Deep-Sea Res.* 40: 1459-1473.

Rodriguez, J., J. Tintore, J.T. Allen, J.M. Blanco, D. Gomis, A. Reul, J. Ruiz, V. Rodriguez, F. Echevarria, and F. Jimenez-Gomez. 2001. Mesoscale vertical motion and the size structure of phytoplankton in the ocean. *Nature*. 410(6826): 360-363.

Roesler, C.S., M.J. Perry, and K.L. Carder. 1989. Modeling in situ phytoplankton absorption from total absorption spectra in productive inland marine waters, *Limnol. Oceanogr., 34*: 1510-1523.

Roesler, C.S., and M.J. Perry. 1995. In situ phytoplankton absorption, fluorescence emission, and particulate backscattering spectra determined from reflectance. *J. Geophys. Res.*, C100: 13 279-13 294.

Roesler, C.S. 1998. Theoretical and experimental approaches to improve the accuracy of particulate absorption coefficients derived from the quantitative filter technique. *Limnol. Oceanogr.*, 43: 1649-1660.

Roesler, C.S., and E. Boss. 2003. Spectral beam attenuation coeffecient retrieved from ocean colour inversion. *Geophys. Res. Lett.* 30(9), 1468-1471.

Roesler, C.S., S.M. Etheridge, and G.C. Pitcher, 2003. Application of an Ocean Color Algal Taxa Detection Model to Red Tides in the Southern Benguela. In: Proceedings of the Tenth International Conference for Harmful Algal Blooms.

Rosen, B. H., and R.L. Lowe. 1984. Physiological and ultrastructural responses of *Cyclotella meneghiniana* (Bacillariophyta) to light intensity and nutrient limitation. *J. Phycol.*, 20: 173-183.

Rosen B.H., M.D. Berliner, and M.J. Petro. 1986. Analysis of starch content in *Chlorella pyrenoidosa* (Chlorophyta) by morphological and quantitative techniques, *Am. J. Bot.*, 73 (9): 1372-1375.

Sciandra A., L. Lazzara, H. Claustre H., and Babin M. 2000. Responses of the growth rate, pigment composition and optical properties of *Cryptomonas* sp. to light and nitrogen stresses. *Mar. Ecol. Prog. Ser.*, 201: 107-120.

Sheldon, R.W., and T.R. Parsons. 1967. A continuous size spectrum for particulate matter in the sea. *J. Fish. Res. Bd. Canada.* 24: 909-915.

Sheldon, R.W., A. Prakash, and W.H. Sutcliffe, Jr. 1972. The size distribution of particles in the ocean. *Limnol. Oceanogr.*, 17(3): 327-340.

Sicko-Goad, L., and E. F. Stoermer. 1979. A morphometric study of lead and copper effects on *Diatoma tenue* var. *elongatum* (Bacillariophyta). *J. Phycol.*, 15: 316-321.

Sosik, H. M. and B. G. Mitchell. 1991. Absorption, fluorescence and quantum yield for growth in nitrogen-limited *Dunaliella tertiolecta*. *Limnol. Oceanogr.*, 36: 910-921.

Spector, D.L., and R.E. Triemer. 1979. Ultrastructure of the dinoflagellate *Peridinium cinctum f. ovoplanum*. I. Vegetative cell structure. *Amer. J. Bot.*, 66: 845-850.

Stephens, F. C., 1995. Variability of spectral absorption efficiency within living cells of *Pyrocystis lunula* (Dinophyta). *Mar. Biol.*, 122: 325–331.

Stramski D, and J. Piskozub. 2003. Estimation of scattering error in spectrophotometric measurements of light absorption by aquatic particles from 3-D radiative transfer equations. *Appl. Opt.*, 42(18): 3634–46.

Stramski, D. 1999. Refractive index of planktonic cells as a measure of intracellular carbon and chlorophyll a content. *Deep-Sea Res.*, 46, 335-351

Stramski D., A. Morel, and A. Bricaud. 1988. Modelling the light attenuation and scattering by spherical phytoplankton cells: a retrieval of the bulk refractive index. *Appl. Opt.*, 27: 2954-3956.

Stramski, D., and D.A. Kiefer. 1991. Light scattering by micro-organisms in the open ocean. *Progr. Oceanogr.*, 28: 343-383.

Stramski, D., A. Bricaud, and A. Morel. 2001. Modeling the inherent optical properties of the ocean based on the detailed composition of planktonic community. *Appl. Opt.*, 40: 2929-2945.

Stramski, D., A. Sciandra, and H. Claustre. 2002. Effects of temperature, nitrogen, and light limitation on the optical properties of the marine diatom *Thalassiosira pseudonana*. *Limnol. Oceanogr.*, 47, 392-403.

Stramski, D., E. Boss, D. Bogucki, and K. J. Voss. 2004. The role of seawater constituents in light backscattering in the ocean. *Progr. Oceanogr.*, 61: 27-56.

Stuart, V., S. Sathyendranath, T. Platt, H. Maass, and B.D. Irwin. 1998. Pigment and species composition of natural phytoplankton populations: effect on the absorption spectra. *J. Plankton Res.* 20: 187-217.

Subramaniam, A., E.J. Carpenter, E. J. and P.G. Falkowski, 1999. Bio-optical properties of the marine diazotrophic cyanobacteria *Trichodesmium* sp. II. A reflectance model for remote sensing. *Limnol. Oceanogr.*, 44: 618-627.

Taguchi, S. 1976. Relationship between photosynthesis and cell size of marine diatoms. *J. Phycol.*, 12: 185–189.

Thinh, L.-V. 1983. Effect of irradiance on the physiology and ultrastructure of the marine cryptomonad, *Cryptomonas* strain Lis (Cryptophyceae). *Phycologia*. 22: 7-11.

Toon, O.B., and T.P. Ackerman. 1981. Algorithms for the calculation of scattering by stratified spheres. *Appl. Opt.*, 20: 3657-3660.

Twardowski, M.S., E. Boss, J.B. Macdonald, W.S. Pegau, A.H. Barnard, and J.R.V. Zaneveld. 2001. A model for estimating bulk refractive index from the optical backscattering ratio and the implications for understanding particle composition in Case I and Case II waters. *J. Geophys. Res.*, 106(C7): 14,129-14,142.

Utermohl,H 1958. Zur Vervollkommnung der quantitativen Phytoplankton. *Methodik. Mitt. Int. Ver. Theor. Angew. Limnol.*, 9: 1-38.

Vaillancourt RD, C.W. Brown, R.R.L. Guillard, and W.M. Balch. 2004. Light backscattering properties of marine phytoplankton: relationships to cell size, chemical composition and taxonomy. *J. Plankton Res.*, 26(2): 191–212.

Van de Hulst H.C. 1957. *Light Scattering by Small Particles*. pp. 470. Wiley, New York.

Visviki I. 2000. A Cytological Study of the Green Alga *Chlamydomonas applanata Pringsheim* (Chlamydomonadaceae). *Journal of the Torrey Botanical Society*, 127(1): 1-8.

Volten, H., J.F. de Haan, J.W. Hovenier, R. Schreurs, W. Vassen., A.G. Dekker, H.J. Hoogenboom, F. Charlton, and R. Wouts. 1998. Laboratory measurements of angular distributions of light scattered by phytoplankton and silt. *Limnol. Oceanogr.* 43: 1180-1197.

Williams, S. C., P. G. Verity, and T. Beatty. 1995. A new staining technique for dual identification of plankton and detritus in seawater. *J. Plankton Res.* 17: 2037-2047.

Witkowski, K., L. Wolinski, Z. Turzynski, D. Gedziorowska, and A. Zielinski. 1993. The investigation of kinetic growth of *Chlorella vulgaris* cells by the method of integral and dynamic light scattering. *Limnol. Oceanogr.*, 38(7): 1365-1372.

Witkowski, K., T. Krol, A. Zielinski, and E. Kuten. 1998. A light-scattering matrix for unicellular marine phytoplankton. *Limnol. Oceanogr.*, 43(5): 859-869.

Yentsch, C.S. 1962. Measurement of visible light absorption by particulate matter in the ocean. *Limnol. Oceanogr.*, 7: 207-217.

Young, E.B., and J. Beardall. 2003. Rapid ammonium- and nitrate-induced perturbations To chl a fluorescence in nitrogen-stressed *Dunaliella Tertiolecta* (Chlorophyta). *J. Phycol.*, 39: 332–342.

Yoshikawa T., and K. Furuya 2004. Long-term monitoring of primary production in coastal waters by an improved natural fluorescence method. *Mar. Ecol. Prog. Ser.*, 273: 17-30.

Zaneveld, J.R.V., and J.C. Kitchen. 1995. The variation in the inherent optical properties of phytoplankton near an absorption peak as determined by various models of cell structure. *J. Geophys. Res.*, 100 (C7): 13,309-13,320.

Zaneveld, J.R.V. 1995. A theoretical derivation of the dependence of the remotely sensed reflectance on the inherent optical properties. *J. Geophys Res.*, 100 (C7): 13,135-13,142.

Zapata M., S.W. Jeffrey, S.W. Wright, F. Rodriguez, J.L. Garrido, and L. Clementson. 2004. Photosynthetic pigments in 37 species (65 strains) of Haptophyta: implications for oceanography and chemotaxonomy. *Mar. Ecol. Prog. Ser.*, 270: 83–102.